

Partial Discharge Diagnosis of High-Voltage Gas- Insulated Systems

Sander Meijer

TR 3762

3252

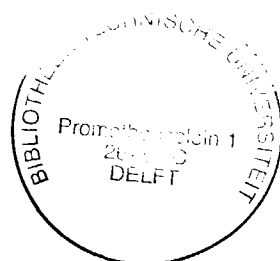
660000

700000

**PARTIAL DISCHARGE DIAGNOSIS OF
HIGH-VOLTAGE GAS-INSULATED SYSTEMS**

PARTIAL DISCHARGE DIAGNOSIS OF HIGH-VOLTAGE GAS-INSULATED SYSTEMS

Proefschrift



ter verkrijging van de graad van doctor
aan de Technische Universiteit Delft,
op gezag van de Rector Magnificus prof. ir. K.F. Wakker,
voorzitter van het College voor Promoties,
in het openbaar te verdedigen
op maandag 5 november 2001 om 10:30 uur
door Sander MEIJER
electrotechnisch ingenieur
geboren te Gouda

Dit proefschrift is goedgekeurd door de promotor:
Prof. dr. J.J. Smit

Samenstelling promotiecommissie:

Rector Magnificus, voorzitter

Prof. dr. J.J. Smit, Technische Universiteit Delft, promotor

Prof. ir. W.L. Kling, Technische Universiteit Delft

Prof. dr. ir. W.R. Rutgers, Technische Universiteit Eindhoven

Prof. dr. ir. J.H. Blom, Technische Universiteit Eindhoven

Prof. dr. ir. L.P. Ligthart, Technische Universiteit Delft

Prof. Dr.-Ing. W. Boeck, Technische Universität München

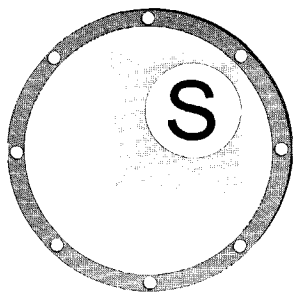
Dr. ir. E. Gulski, Technische Universiteit Delft

The investigations described in this thesis have financially and
technically been co-sponsored by
TenneT BV, Arnhem, The Netherlands
Alstom T&D, Villeurbanne Cedex, France

ISBN: 90-77017-23-2

Druk: Optima Grafische Communicatie, Rotterdam

Aan Rosita, Anoeck en Mark



SUMMARY

Partial Discharge Diagnosis of High-voltage Gas-insulated Systems

In the last thirty years, gas-insulated substations have proven to be very reliable. Moreover, many gas-insulated substations are installed at important nodes in the electricity grid. However, several failures have occurred, which involved high costs. Therefore, means to prevent failures are definitely wanted.

Moving particles, particles on insulators and protrusions on the conductors can be very dangerous to the insulation conditions of the gas-insulated substation. This means that the detection and recognition of these defects at an early stage are important for condition-based maintenance of gas-insulated substations. One of the most sensitive means to predict failures caused by such insulation defects is the detection of partial discharge activity.

In this thesis, the use of the ultra-high frequency partial discharge measuring technique for condition-based maintenance of gas-insulated systems is investigated.

In chapter 2 a brief introduction is given on gas-insulated systems, SF_6 gas and $\text{SF}_6\text{-N}_2$ gas mixtures, typical insulation defects that can occur in gas-insulated systems and electromagnetic wave propagation.

In chapter 3 the used partial-discharge measuring techniques and analysis techniques are described. Different key values are defined to compare the

energy content of partial discharge frequency spectra. In this chapter also amplitude distributions from the frequency spectra are defined, which have been analysed by statistical analysis.

Chapter 4 describes the signal propagation of UHF electrical signals through gas-insulated substations. With knowledge on pulse propagation the optimal UHF coupler locations can be determined to ensure a certain sensitivity of the UHF measuring circuit.

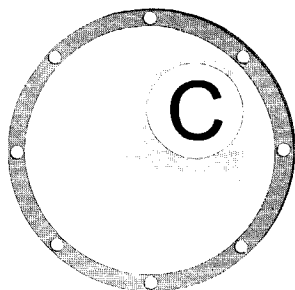
In chapter 5 different insulation defects are investigated in pure SF_6 and SF_6 - N_2 gas mixtures containing 5% or 10% SF_6 . As a result, the influence of these defects on the insulation condition of the gas could be determined and typical results have been stored in a reference database.

Chapter 6 describes a procedure for on-site UHF partial discharge measurements. The UHF measuring technique has been added to the maintenance procedure of the 380 kV gas-insulated substation in Meeden, The Netherlands.

Risk assessment of defects on the insulation condition of the GIS has been investigated in chapter 7. It is shown that combined PD pattern analysis and spectral analysis provide the required information to determine the criticality of fixed protrusions and free particles.

It has been shown that the UHF partial discharge measuring technique is a technique which is sensitive enough to monitor the insulation condition of gas-insulated systems.

Sander Meijer



CONTENTS

SUMMARY vii

CHAPTER 1 INTRODUCTION 1

 1.1 STATE OF THE ART: GIS 1

 1.2 STATE OF THE ART: PARTIAL DISCHARGE ANALYSIS 4

 1.3 AIM OF THIS THESIS 6

 1.4 STRUCTURE OF THIS THESIS 7

CHAPTER 2 PARTIAL DISCHARGE PHENOMENA IN GIS 9

 2.1 INSULATING GASES 9

 2.2 PARTIAL DISCHARGE MECHANISMS 12

 2.3 INSULATION DEFECTS IN GIS 13

 2.3.1 FIXED PROTRUSIONS 14

 2.3.2 FREE PARTICLES 15

 2.3.3 ELECTRICALLY FLOATING ELECTRODES 16

 2.3.4 PARTICLES FIXED ON INSULATOR SURFACES 16

 2.4 ELECTROMAGNETIC WAVES IN GIS 17

 2.4.1 TEM-MODES 18

 2.4.2 HIGHER-ORDER MODES 19

 2.4.3 RESONANCES 21

CHAPTER 3 ADVANCED PD ANALYSIS 25

 3.1 INTRODUCTION 25

 3.2 SIGNAL PROCESSING OF UHF SPECTRA 27

 3.2.1 MAX HOLD FREQUENCY SPECTRUM 28

 3.2.2 AVERAGED FREQUENCY SPECTRUM 28

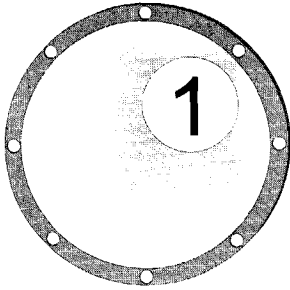
 3.2.3 SIGNAL-TO-BACKGROUND NOISE RATIO SPECTRUM ... 30

 3.3 TIME-OF-FLIGHT ANALYSIS 31

 3.4 AMPLITUDE ANALYSIS OF UHF SPECTRA 32

3.5 STATISTICAL ANALYSIS OF FREQUENCY SPECTRA	39
3.5.1 AMPLITUDE WINDOWS	40
3.5.2 FREQUENCY WINDOWS	41
3.6 ANALYSIS OF PHASE-RESOLVED PD PATTERNS	44
3.7 CONCLUSIONS	47
CHAPTER 4 SIGNAL PROPAGATION AND REDUCTION IN GIS	49
4.1 REFLECTION AND TRANSMISSION OF EM-WAVES	50
4.2 SIGNAL REDUCTION CAUSED BY A SPACER	51
4.2.1 TRANSMISSION LINE MODEL OF A SPACER	51
4.2.2 TRANSMISSION LINE MODEL OF TWO SPACERS	56
4.3 REFLECTION COEFFICIENTS OF GIS COMPONENTS	58
4.4 COMPARISON SIGNAL REDUCTION FROM ARTIFICIAL AND PARTIAL DISCHARGE PULSES	59
4.5 SIGNAL REDUCTION OF GIS	60
4.5.1 GIS SECTIONS	60
4.5.2 A REAL SUBSTATION	61
4.6 OPTIMAL SENSITIVITY OF UHF MEASURING CIRCUIT	64
4.6.1 COUPLER LOCATIONS	64
4.6.2 CIGRE SENSITIVITY CHECK	67
4.7 CONCLUSIONS	71
CHAPTER 5 EXPERIMENTAL RESULTS	73
5.1 PD DETECTION SYSTEM ACCORDING TO IEC 60270	73
5.2 PROTRUSION FIXED TO THE HIGH-VOLTAGE CONDUCTOR	75
5.2.1 PD INCEPTION AND BREAKDOWN VOLTAGE	75
5.2.2 PHASE-RESOLVED PD PATTERNS	76
5.2.3 PD MAGNITUDE	78
5.2.4 UHF FREQUENCY SPECTRA	79
5.2.5 UHF PHASE-RESOLVED PD PATTERNS	80
5.3 PROTRUSION FIXED TO THE ENCLOSURE	81
5.3.1 PD INCEPTION AND BREAKDOWN VOLTAGE	81
5.3.2 PHASE-RESOLVED PD PATTERNS	82
5.3.3 PD MAGNITUDE	83
5.3.4 UHF FREQUENCY SPECTRA	84
5.3.5 UHF PHASE-RESOLVED PD PATTERNS	84
5.4 FREE MOVING PARTICLES	85
5.4.1 INCEPTION VOLTAGE	85
5.4.2 PHASE-RESOLVED PD PATTERNS	86
5.4.3 PD MAGNITUDE	87
5.4.4 UHF FREQUENCY SPECTRA	87
5.4.4 UHF PHASE-RESOLVED PD PATTERNS	88
5.5 SUMMARY AND CONCLUSIONS	89

CHAPTER 6 APPLICATION OF ON-SITE UHF PD INSPECTIONS	91
6.1 ON-SITE GIS DIAGNOSTICS	91
6.2 CONCLUSIONS	96
CHAPTER 7 INSULATION CONDITION ASSESSMENT	97
7.1 PD IDENTIFICATION IN PURE SF ₆ AND SF ₆ -N ₂ MIXTURES	98
7.1.1 STATISTICAL ANALYSIS OF PD PATTERNS	98
7.1.2 STATISTICAL ANALYSIS OF FREQUENCY SPECTRA	100
7.1.3 CONCLUSIONS STATISTICAL PD IDENTIFICATION	102
7.2 CRITICALITY UNDER AC VOLTAGE CONDITIONS	104
7.2.1 FIXED PROTRUSIONS	105
7.2.2 FREE PARTICLES	107
7.3 SUMMARY AND CONCLUSIONS	114
CHAPTER 8 CONCLUSIONS	117
REFERENCES	121
APPENDICES	
A ELECTROMAGNETIC FIELD CALCULATION	127
B OPTIMISATION SPECTRUM ANALYSER SETTINGS	137
C PROCEDURE TO CALCULATE REFLECTION COEFFICIENTS .	141
D PROCEDURE FOR ON-SITE UHF PD MEASUREMENTS	149
LIST OF SYMBOLS	153
LIST OF ABBREVIATIONS	157
ACKNOWLEDGMENTS	159
SAMENVATTING	161
RÉSUMÉ	163



CHAPTER 1 INTRODUCTION

1.1 STATE OF THE ART: GIS

Since the early seventies, SF_6 gas-insulated substations (GISs) are in use all over the world [1]. Figure 1.1 shows an example of a 380 kV GIS, which is located in Meeden, the Netherlands. Substations form nodes in the electricity grid and are used for distribution and transport of electricity and protection [2]. Important technical reasons to prefer metal-enclosed gas-insulated systems to air-insulated systems are, e.g., reduced influence of environmental and industrial conditions, reduced substation space and increased safety [3, 4, 5].

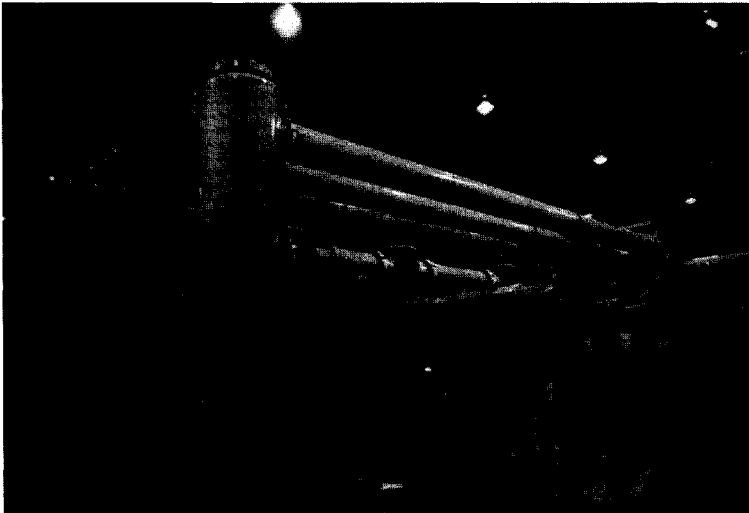


Figure 1.1: Part of the 380 kV gas-insulated substation in Meeden, the Netherlands.

Gas-insulated sub-stations, figure 1.2, are modular systems consisting of a gas-tight (for example coaxial) enclosure in which an insulating gas is confined. The high-voltage (HV) conductor is centred by spacers. Instead of pure SF_6 , gas mixtures of SF_6 and N_2 can be used to reduce costs of the equipment and SF_6 leakages [6]. A GIS has, besides these straight parts, more complex parts such as circuit breakers, disconnecting and earthing switches, T-junctions and bends. A typical 245 kV double busbar bay is shown in figure 1.3.

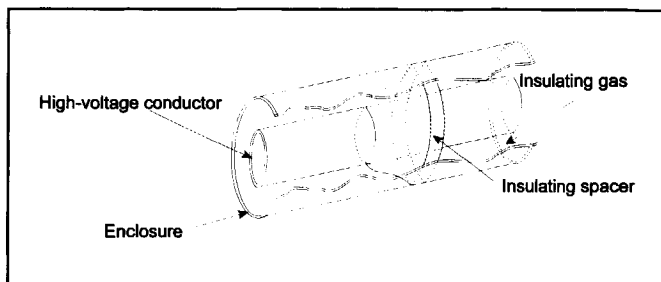


Figure 1.2: Structure of gas-insulation systems. A gas-tight enclosure confines the gas insulation. The high-voltage conductor is centred and held by insulating spacers.

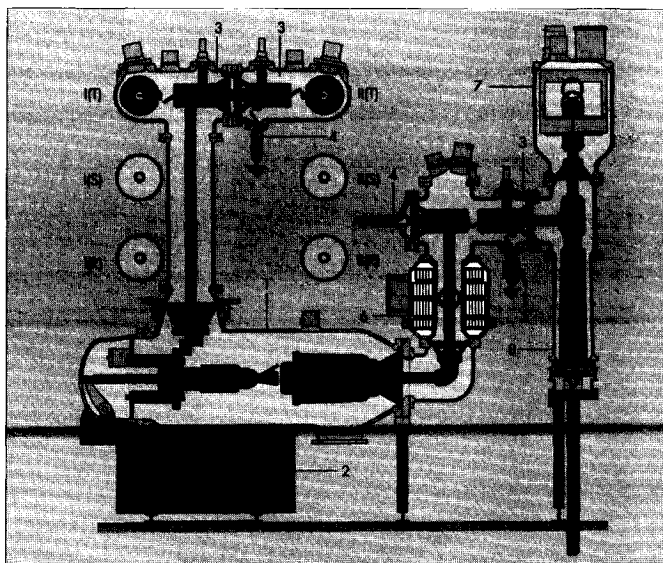


Figure 1.3: Typical 245 kV double busbar bay (I and II are the busbars):

1) circuit breaker, 2) spring mechanism, 3) disconnector, 4+5) earthing switch, 6) current transformer, 7) voltage transformer, 8) HV cable connection (courtesy of Alstom T&D, France).

Although several failures over the last 30 years have been reported in two international surveys, GISs have proven to be very reliable [3, 4, 5]. Nevertheless, due to the high costs involved with a failure, means to prevent failures are definitely wanted. In particular, the occurrence of defects like free particles, particles on insulator surfaces and protrusions fixed to the conductors can be very dangerous to the insulation conditions of the GIS [7]. Depending on the type of insulation defect, a breakdown can follow immediately, after days, months or even after years. This means that the detection and recognition of these defects at an early stage are important to avoid possible failure of GIS.

The collected failure data (871 failures) in the survey [5] refers to 2115 GIS installations, 13696 circuit breaker bays and 118483 circuit-breaker-bay-years. This results in an average of 0.75 failures per 100 circuit-breaker-bay-years for all voltage classes. Field measurements described in this thesis have been carried out at one of the 380 kV gas-insulated substations in The Netherlands (Meeden), figure 1.1. This substation has been operational since mid 1995 and belongs to the voltage class $300 \text{ kV} < U < 500 \text{ kV}$ described in the previously mentioned international surveys [3, 4, 5]. Within this voltage class, 161 failures have been reported over 6371 circuit-breaker-bay-years, resulting in an average failure frequency of 2.58/100-circuit-breaker-bay-years.

The survey [5] shows that a breakdown of the insulation system occurred in 66% of the 161 reported failures. Moreover, 58% of the failures occurred during normal operation of the GIS at nominal power frequency voltage, 25% during switching operations, 1% during lightning over-voltages and 5% during fast transients. The remaining 11% of reported failures had several different causes. In this thesis we are investigating the risk for breakdown under normal operation of the GIS at nominal power frequency. It can be concluded that in 38% of the reported failures a breakdown occurred at nominal voltage and power frequency. This means an average breakdown frequency of 0.99/100-circuit-breaker-bay-years in voltage class 4. For Meeden, where 9 circuit-breaker bays are installed, this would mean that every $11\frac{1}{4}$ years, failure of a circuit-breaker bay due to a breakdown of the insulation system can be expected.

As known, a breakdown is often preceded by partial discharge (PD) activity [8]. In service, usually low PD activity occurs, which itself is not dangerous

for the operation of a GIS. Moreover, it can be a good indication of the condition of the insulation. Therefore, one of the most sensitive means to predict an upcoming failure involving one of these defects, is the detection of partial discharge activity [7, 9]. In Meeden, no breakdowns have occurred up to now, and periodic inspections are applied to evaluate the insulation condition. Failure mechanisms which are not preceded by PD-activity, for example due to malfunctioning of circuit breakers, require other diagnostic methods, which are beyond the scope of this work.

Besides the primary equipment, secondary equipment is installed, to monitor apparatus conditions (such as voltage levels, current, gas pressure), which are beyond the scope of this thesis. The recently developed UHF couplers offer the possibility to detect partial discharge activity on-line [11]. In this way, the insulation condition of the GIS can be monitored and insulation problems accompanied by partial discharges can be effectively detected. The UHF monitor can be implemented as a part of the secondary equipment in future GIS.

1.2 STATE OF THE ART: PARTIAL DISCHARGE ANALYSIS

Prior to energizing the GIS, several tests are performed as described in [10]. During tests in the factory all different GIS parts and components are tested separately. A PD-level less than 5 pC is required to pass the test. All spacers are separately tested for internal defects. The tests after installation are not as severe as those in the factory and are mainly used to check if no defects were introduced by the installation.

During operation, the insulation condition can be checked by periodic or continuous PD measurements [11]. The following measuring systems are commonly used:

1. Electric measuring systems based on the IEC 60270 recommendations [12];
 2. Acoustic measurements using externally mounted acoustic sensors: detection of the acoustic signals emitted by a PD source [13];
 3. Electric VHF/UHF measuring systems which use narrowband or wideband filters [11, 14, 15];
 4. Other detection methods, for example based on chemical or optical properties of discharging defects [7].
-

In this thesis only electrical measuring systems (1 and 3) have been applied.

The main advantages of a standardized system are the more than 30-year experience and the availability of digital tools for PD recognition [16]. However, it has restrictions in the field application due to noise. To improve the signal-to-noise ratio, VHF/UHF detection circuits can be used to achieve a sensitive measuring system for on-line testing of GIS [15]. Depending on the specific circuitry and the type of defect even better sensitivity than with a standardized circuit can be achieved, section 5.4.

A discharging defect can be modelled as a current source, which injects a charge pulse into the GIS. Due to the short rise-time of these pulses [17], high-frequency electromagnetic waves are generated which propagate in the GIS configuration. A UHF partial discharge detection circuit uses a receiving antenna (UHF coupler) to pick up these electromagnetic waves. However, the high-frequency waves have to follow complex paths between the PD source and the UHF coupler, consisting of T-junctions, disconnectors, spacers, circuit breakers and busbars of 30 metres or more. Each component influences the propagation of these waves and each interface between two components introduces reflection and attenuation. This means that after passing several components the UHF signals can be totally damped. To ensure enough sensitivity sufficient UHF couplers have to be mounted. In practice this is done by using a rule of thumb proposed by Hampton which goes: install a coupler each 20 m of GIS [18].

Several exceptions to this rule have been reported [19-21] showing that:

- in the case of simple straight enclosures the distance between two couplers can be much longer than 20 m;
- in the case of circuit breakers or disconnectors, the distance between two couplers must be less than 20 m.

Therefore, the above rule is too simple and needs a more advanced approach.

It is known that a relationship exists between the shape of phase-resolved PD patterns and the discharge source (type of defect) [22]. Each discharging defect with its geometry, location in insulation, dielectric properties and local field is characterized by a specific PD sequence. Analysis of these sequences has shown to be a good means to distinguish

the different discharge patterns [22, 23]. However, in some cases, only analysis of PD patterns or PD pulse sequences is not sufficient for identification of different defects and, therefore, other PD related diagnostic tools have to be applied.

As stated before, to reduce the amount of used SF_6 and SF_6 leakage, gas mixtures of SF_6 and N_2 can be used instead of pure SF_6 as insulating gas in GIS, in particular in large systems such as gas-insulated lines. Many breakdown investigations in pure SF_6 and gas mixtures have been performed over the last decades [26-31], however only few investigations regarding PD phenomena have been described. To assess the risk of several defects in pure SF_6 and SF_6 - N_2 mixtures for a breakdown of the insulation system, knowledge regarding PD phenomena is necessary.

1.3 AIM OF THIS THESIS

The goal of this study is to derive the necessary systematic knowledge underlying the implementation of UHF partial discharge diagnostics for assessment of the dielectric condition of metal-enclosed gas-insulated substations under normal operational conditions at nominal power frequency voltage (corresponding to 38% of the failures).

For this purpose, the following four points of interest have to be investigated, see also figure 1.4:

1. The first is the modelling of the wave propagation through GIS in order to determine the locations of the UHF couplers to reach the required detection sensitivity.
 2. The second is the application of spectral analysis for defect recognition and amplitude-extraction.
 3. The third is to compare the influence of defects in pure SF_6 and SF_6 - N_2 gas mixtures on the insulation strength.
 4. The fourth is to correlate the PD information to the risk of insulation defects for a breakdown under normal AC operation conditions.
-

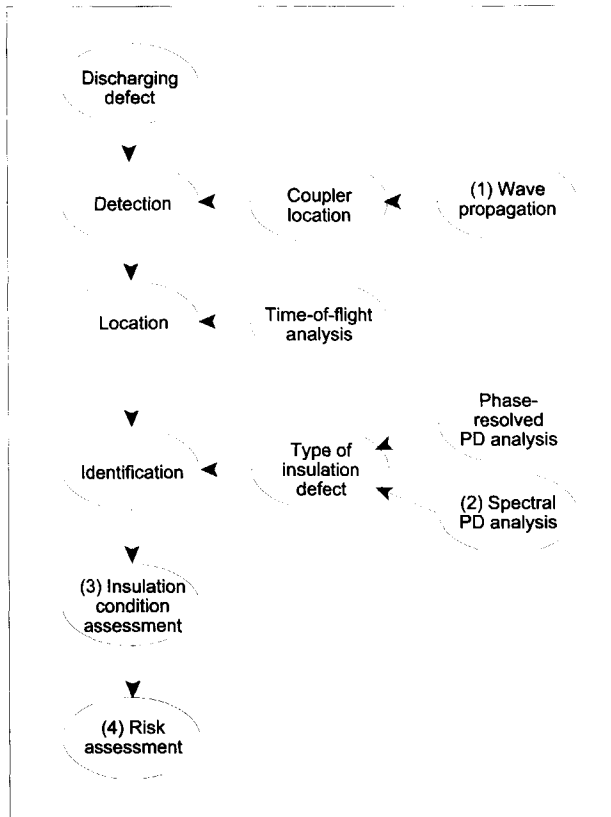


Figure 1.4: *Different aspects to assess the insulation condition of a gas-insulated substations in case of discharging defects (points of interest 1-4 indicated).*

1.4 STRUCTURE OF THIS THESIS

The following aspects are investigated in this thesis.

Chapter 2 describes partial discharge phenomena of typical defects that can result in a failure.

Chapter 3 describes the hardware and software of the UHF partial discharge detection system. We define key values which can be extracted

from the frequency spectra. Statistical analysis of frequency spectra is described for defect recognition.

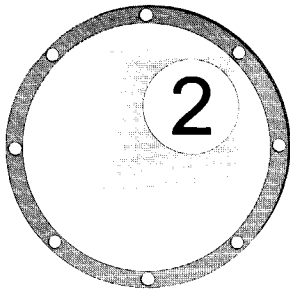
Chapter 4 describes the signal propagation of UHF electrical signals through GIS. Transmission line modelling has been used to determine the influence of different GIS components on the UHF signals. Sensitive coupler locations in GIS have been determined and tested to ensure enough detection sensitivity for defects in GIS.

In chapter 5 several defects in pure SF_6 and $\text{SF}_6\text{-N}_2$ mixtures are investigated and compared.

In chapter 6 field experiments obtained in the 380 kV GIS in Meeden are described.

In chapter 7 analysis of the insulation-condition of GIS is described. It is shown that using different evaluation techniques discrimination between different insulation defects and the generation of early warnings of several defects is possible.

Finally, conclusions are drawn in chapter 8.



CHAPTER 2 PARTIAL DISCHARGE PHENOMENA IN GIS

2.1 INSULATING GASES

Sulphur hexafluoride (SF_6) was discovered in 1900 from a reaction of fluorine and sulphur [1]. Since 1950, SF_6 is in use as insulation gas in high-voltage equipment because of its excellent insulating properties. Important properties of SF_6 are [24]:

- 1) SF_6 is electronegative and captures low energy electrons ($< 0.1 \text{ eV}$), resulting in heavy long-lived ($> 10^{-5} \text{ s}$) ions which are much slower than electrons. These ions prevent the forming of electron avalanches, leading to higher breakdown stress;
- 2) At atmospheric pressure the dielectric strength of SF_6 is roughly 2.3 times higher than that of air (8.9 kV/mm at 1 bar);
- 3) At higher pressures (until liquefaction) even higher insulation levels can be obtained;
- 4) The insulation strength recovers after breakdown;
- 5) Pure SF_6 is nontoxic, dissociation products however are toxic and corrosive;
- 6) It is nonflammable.

In the case of imperfections such as fixed protrusions, field enhancement can occur. As a result, free electrons can gain energy levels above 0.1 eV and the attachment by SF_6 molecules becomes less effective. To reduce the energy level of free electrons below 0.1 eV (i.e. slow down the speed of free electrons), SF_6 can be mixed with other gases which have properties to slow down the speed (N_2 vibration levels: 2-4 eV) [26]. Other reasons to mix SF_6 are that SF_6 is an expensive and greenhouse gas [27].

Investigations have shown that the use of a mixture of SF_6 and N_2 is a low-cost alternative to pure SF_6 in high-voltage applications. In addition, these mixtures have less environmental impact [27]. Moreover, the electrons are scattered into the low energy region where SF_6 captures the electrons still efficiently [26]. Properties of nitrogen are that it is cheap, inert, nontoxic, nonflammable, and of course environmentally acceptable [26, 27]. It has been shown that even small amounts of SF_6 in N_2 rapidly increase the dielectric strength of the mixture, which can be explained by the reduction of the effective ionisation coefficient, see figure 2.1b [64]; the increase in dielectric strength tends toward saturation when the amount of SF_6 is increased above 50%, see figure 2.1a [27, 29]. Because only a small percentage of SF_6 has such a large influence on the breakdown strength of the SF_6 - N_2 gas mixture, we investigated gas mixtures containing 5% and 10% SF_6 in this thesis.

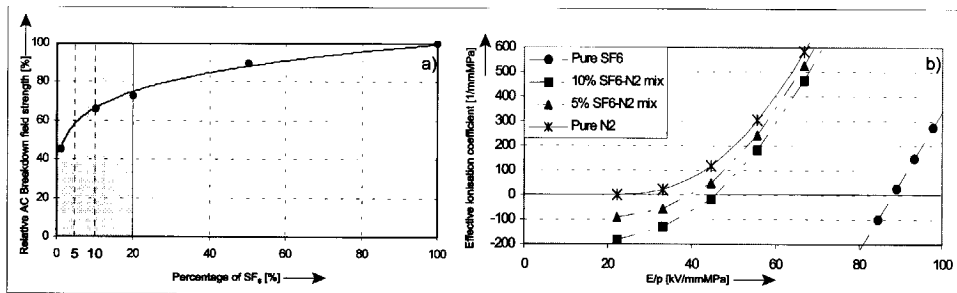


Figure 2.1: Properties of SF_6 - N_2 mixtures:

- Critical AC field strength of a SF_6 - N_2 mixture as function of the SF_6 percentage, reproduced from [29]. The typical range of SF_6 percentages of interest has been dashed.*
- Effective ionisation coefficient [64]*

The test specifications of most high-voltage AC equipment is dominated by the basic insulation level (BIL) [25]. This is the level of the full-wave lightning impulse that must be withstood in a network without any damage or flashover. Using the lightning impulse breakdown voltages measured by Guillen et.al [30] in a full scale setup without defects we reproduced figure 2.2. It shows that dielectric strengths equivalent to 4.5 bar pure SF_6 occur if the 5% gas mixture has a gas pressure of 11.5 bar and the 10% gas mixture has a gas pressure of 9.8 bar (table 2.1). In chapter 5 we compare PD phenomena in 4.5 bar pure SF_6 , 11.5 bar 5% mixture and 9.5 bar 10% mixture.

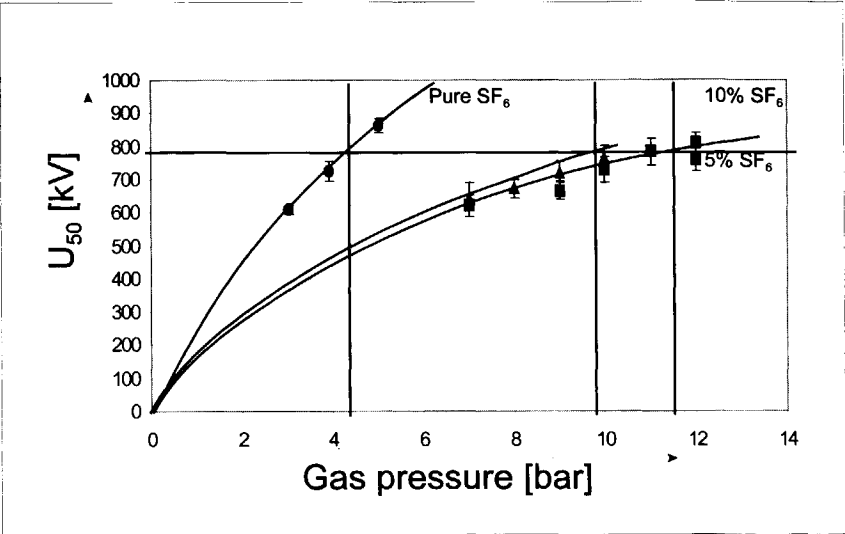


Figure 2.2: Experimental results of breakdown tests in pure SF_6 , 5% SF_6 - N_2 mixture and 10% SF_6 - N_2 mixture, reproduced from [30].

Table 2.1: Gas pressures to obtain equivalent dielectric strengths for different types of gas.

Gas type	Pressure in service
Pure SF ₆	4.5 bar
5% SF ₆ -N ₂ mixture	11.5 bar
10% SF ₆ -N ₂ mixture	9.8 bar

2.2 PARTIAL DISCHARGE MECHANISMS

To describe the PD occurrence in gases, three mechanisms have to be mentioned [24, 28].

1) Townsend Mechanism

The primary process in the gas is ionization of the gas molecules by collision between gas molecules and free electrons which have been accelerated by the field. New electron-ion pairs are formed and the number of electrons and ions grows: exponentially formation of avalanches.

Only avalanches do not result in breakdown. Feed-back processes are required which release new start-electrons. Examples of feed-back processes are:

- release of new electrons from positive ions hitting the cathode surface;
- photoelectric emission from the cathode;
- photo ionization in the gas caused by photons from excited atoms or from recombination processes.

Because of the above-mentioned processes, the criterion for breakdown according to the Townsend mechanism can be described by [24]

$$\int_0^x (\alpha - \eta) dx \geq \ln \left(1 + \frac{1}{\Gamma} \right) \quad (2.1)$$

in which α represents the ionisation coefficient of the gas, η the attachment coefficient of the gas and Γ represents the combined effects of the mentioned feedback mechanisms for creating secondary electrons.

2) Streamer Mechanism

At higher gas pressures or larger electrode-gaps (so typical GIS conditions), breakdown can be explained by the streamer theory. This theory assumes that the growth of a single electron avalanche becomes unstable due to the influence of the space charge field at the head of the avalanche. The conditions for streamer formation in SF_6 are fulfilled if the number of ions in an avalanche reaches 10^8 [24].

$$e^{\int_0^x (\alpha - \eta) dx} \geq 10^8 \quad (2.2)$$

in which α represents the ionisation coefficient of the gas and η the attachment coefficient of the gas.

3) Leader breakdown in SF₆

In case of non-uniform gas gaps in pure SF₆ at higher gas pressure (> 5 bar), breakdown occurs by the leader mechanism [28]. If the criteria for avalanche ionisation and streamer inceptions are fulfilled, a corona can propagate. The growth of this corona eventually stops when the propagation conditions are no longer fulfilled at the streamer tips. Now, two types of leader mechanisms can occur:

1. Stem mechanism: Depending on the energy in the streamer channel, expansion of the gas can take place which can result in reduction of the gas density. Ionisation can restart and a conducting channel can be created which becomes a leader section.
2. Precursor mechanism: The positive and negative ions drift apart and form space charge filaments which locally enhance the field strength. As a result, ionisation can restart and can result in a leader section.

The leader formation process repeats and results in a stepwise propagation growth of a possible breakdown path.

2.3 INSULATION DEFECTS IN GIS

Accidentally defects can be introduced into the insulation system during operation of the GIS, in particular by moving parts inside a GIS or due to vibrations [7]. Four important types of insulation defects are shown in figure 2.3:

1. Protrusions;
 2. Free moving particles;
 3. Electrically floating electrodes;
 4. Particles fixed to an insulator surface.
-

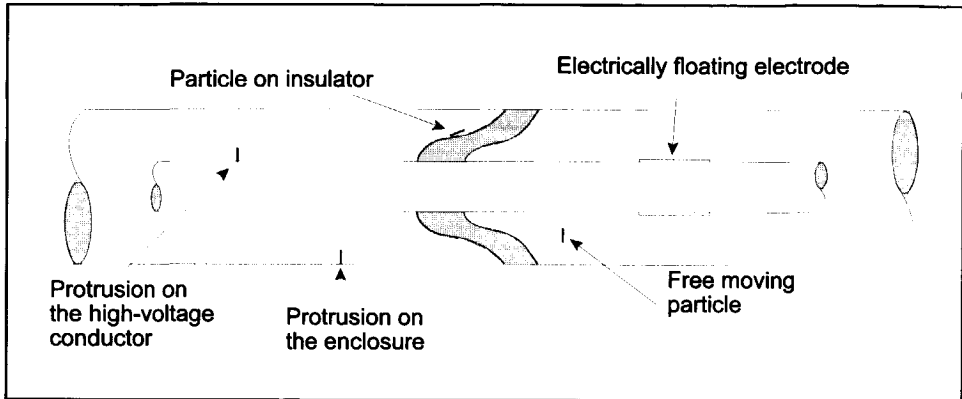


Figure 2.3: *Examples of possible insulation defects in GIS.*

2.3.1 FIXED PROTRUSIONS

Protrusions fixed to the conductor can be introduced during assembly, e.g. by scratching of parts, or during service life due to operation of contacts. Protrusions can be very dangerous because they locally enhance the electric-field strength. It is known that protrusions can get corona stabilised at AC voltage and do not cause breakdown under steady state conditions. However, due to lightning or switching impulses, a breakdown can occur [7]. In this thesis, we investigated the case of a 15 mm metallic protrusion fixed to the HV conductor, see figure 2.4. The protrusion has a tip radius of about 100 μm .



Figure 2.4: *The protrusion fixed to the high-voltage conductor.*

We also investigated a protrusion fixed to the enclosure (LV protrusion). Due to a lower electric field intensity near the enclosure, protrusions fixed to the enclosure have less influence compared to protrusions fixed to the high-voltage conductor. We investigated the case of a 30 mm metallic protrusion fixed to the enclosure; it has a tip radius of roughly 100 μm , see figure 2.5.

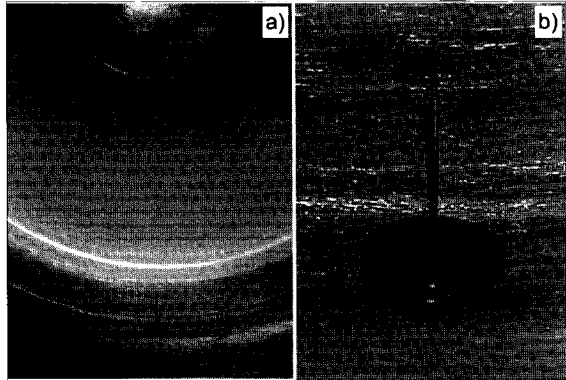


Figure 2.5: *The protrusion fixed to the enclosure:*

- a) Overview of the location in the set-up
- b) Detail of the protrusion

2.3.2 FREE PARTICLES

Another defect that can occur in GIS is the free moving particle [7]. A free conducting particle resting in contact with an electrode of an energized system is a localized perturbation of the conductor, which acquires charge and distorts the electric field. The shape, location and orientation determine the induced charge distribution [31, 32]. Depending on the accumulated charge of the particle and the applied electric field, an electrical force acts on the particle. The charged particle will lift as soon as this force exceeds the gravitational force. Especially when a particle approaches the high-voltage conductor, a breakdown can occur [7].

Another consequence of a moving particle is the possibility that it attaches itself to an electrode, which can result in corona, or that it attaches itself to a spacer, which may result in a breakdown along the gas-solid interface (see also section 2.3.4) [31]. In this thesis, we investigated the particle shown in figure

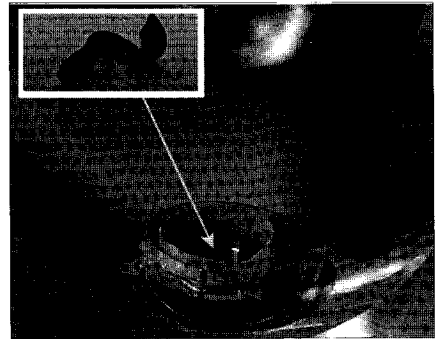


Figure 2.6: *The investigated free particle located in a conducting dish inside the setup (inset: detail of the free particle).*

2.6a. To ensure that the particle is not attracted to the spacer and to give it artificially the same freedom to move, it is placed in a conducting dish, see figure 2.6b.

2.3.3 ELECTRICALLY FLOATING ELECTRODES

A field grading shield, for example as shown in figure 2.7, can lose its contact with the conductor: an electrically floating electrode. In this case it achieves a potential which is determined by the relationship between its capacitance and the conductor vs. that to ground. If as a result of these capacitances and the applied voltage the component adopts a potential which exceeds the insulation strength of the gas, a discharge occurs [33]. Electrically floating electrodes may give relatively high electric and acoustic PD signals (more than 1000 pC) [7].



Figure 2.7: Example of a field grading shield.

In practice these kinds of defects are not immediately fatal. Of course, the material will be damaged by the many partial discharges and also dust will be produced. Eventually this can result in a breakdown.

2.3.4 PARTICLES FIXED ON INSULATOR SURFACES

A dielectric insulator surface affects the motion of free particles. It attracts free particles which can attach to the insulator surface. Enhancement of the electric field strength results and can trigger flashover along the surface [7, 31].

As an example see figure 2.8a, where a small particle is fixed to an insulator surface in a laboratory setup. Under influence of the applied electric field this resulted in flashover as shown in figure 2.8b. In this case no PD activity has been detected prior to the breakdown. Because of the absence of an early warning by partial discharges in some cases, this type

of defect can be very dangerous and proper cleaning of the surfaces and proper testing are very important to avoid that particles remain fixed to insulator surfaces.

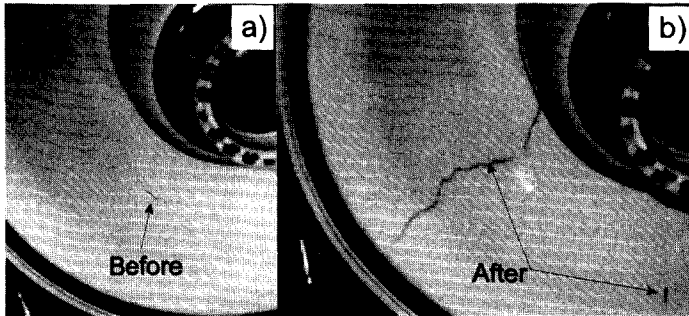


Figure 2.8: a) Particle fixed to an insulator surface and b) the tracking on the insulator surface after flashover.

2.4 ELECTROMAGNETIC WAVES IN GIS

PD pulses in GIS can have rise times down to 50 ps, which means that electromagnetic waves (em-waves) at frequencies up to 20 GHz are emitted [17]. The excited electromagnetic waves propagate in the gas-insulation system along its coaxial structure. At low (power) frequency conditions, where the wavelength is long compared to the diameter of the structure, the wave-propagation is a Transverse Electromagnetic (TEM wave): both the electric and the magnetic fields are entirely transverse to the direction of transmission. No component of either the electric or magnetic field lies in the direction of transmission. The TEM-waves can only propagate if both inner and outer conductor are present. As a result, these waves can not pass switching compartments with opened contacts.

At higher frequencies (thus shorter wavelengths) more complex field configurations become possible: TE- and TM modes. These modes are not entirely transverse: the electric field or the magnetic field have a component in the direction of transmission, called TM wave respectively TE wave. Thus a transverse electric wave has a transverse electric field component and the magnetic field has both longitudinal and transverse field components. In contrast to the TEM-waves, TE and TM waves can

also propagate without the presence of the inner conductor. This means that these em-waves can pass switching compartments with opened contacts.

2.4.1 TEM-MODES

The electromagnetic waves can be described by the wave equations for the electric and magnetic field, derived from the Maxwell equations (A.1) [34-38]. For TEM propagation of signals in the z-direction, the field components have $E_z=0$ and $H_z=0$ (see Appendix A). For propagation in the z-direction in general the solution can be written as:

$$\begin{cases} \hat{V}(z, j\omega) = \hat{V}^+ e^{-\gamma z} + \hat{V}^- e^{\gamma z} \\ \hat{I}(z, j\omega) = \hat{I}^+ e^{-\gamma z} + \hat{I}^- e^{\gamma z} \end{cases} \quad (2.3)$$

with

$$\begin{cases} \hat{V}^+ = Z_0 \hat{I}^+ \\ \hat{V}^- = -Z_0 \hat{I}^- \\ \gamma = \sqrt{j\omega\mu(\sigma + j\omega\epsilon)} \\ Z_0 = \sqrt{\frac{j\omega\mu}{\sigma + j\omega\epsilon}} \frac{\ln\left(\frac{r_o}{r_i}\right)}{2\pi} \end{cases} \quad (2.4)$$

where γ is the propagation constant, μ is the permeability of the gas, ϵ is the permittivity of the gas, r_i is the radius of the high-voltage conductor, r_o the radius of the enclosure and Z_0 the characteristic impedance of the GIS. As a result the propagating TEM-modes are fully described.

2.4.2 HIGHER-ORDER MODES

The electromagnetic waves not only propagate in the TEM-mode, but also as TE- and TM-modes. As described in Appendix A, these modes can be calculated from the Helmholtz equations in polar coordinates (A.25):

$$\begin{cases} \nabla_{r\varphi}^2 \hat{E} = -k^2 \hat{E} \\ \nabla_{r\varphi}^2 \hat{H} = -k^2 \hat{H} \end{cases} \quad (2.5)$$

where

$$k^2 = \gamma^2 + \omega^2 \mu \epsilon \quad (2.6)$$

Because the propagation is directed along the z-axis described by $e^{\pm \gamma z}$, the wave equation depends only on the transverse variables r and φ . In this case, it is possible to express the transverse field components E_φ , E_r , H_φ and H_r in terms of the longitudinal components E_z and H_z . The field solutions can be characterized either by transverse-electric (TE) modes or transverse-magnetic (TM) modes: $E_z=0$ or $H_z=0$, respectively.

As shown in appendix A, the fields in the z-direction can be written as (A.33):

$$\begin{cases} E_z = R_E(r) \cdot F_E(\varphi) \cdot e^{-\gamma z} \\ H_z = R_H(r) \cdot F_H(\varphi) \cdot e^{-\gamma z} \end{cases} \quad (2.7)$$

where

$$\begin{cases} R_X(r) = A_X J_m(k \cdot r) + B_X N_m(k \cdot r) \\ F_X(\varphi) = C_X \cos(m \cdot \varphi) + D_X \sin(m \cdot \varphi) \end{cases} \quad (2.8)$$

in which J_m is the Bessel function of order m and N_m is the Neumann function of order m and A_X , B_X , C_X and D_X are constants and $X=\{E,H\}$, depending on the type of field being solved.

At this point the following two conditions are distinguished:

- 1) The magnetic field is transverse to the propagation direction, which means that $H_z=0$. The modes in which electromagnetic waves propagate are called TM-modes.
- 2) The electric field is transverse to the propagation direction, which means that $E_z=0$. The modes in which electromagnetic waves propagate are called TE-modes.

To calculate the TM-modes, besides the condition $H_z=0$, also the boundary condition that the electric field has to vanish on the inner conductor (with radius r_i) and outer conductor (with radius r_o) has to be taken into account:

$$\begin{cases} \hat{E}_z(r_i) = 0 \\ \hat{E}_z(r_o) = 0 \end{cases} \quad (2.9)$$

As a result, the following set of equations has to be solved:

$$\begin{cases} A_E J_m(k \cdot r_i) + B_E N_m(k \cdot r_i) = 0 \\ A_E J_m(k \cdot r_o) + B_E N_m(k \cdot r_o) = 0 \end{cases} \quad (2.10)$$

This set of equations can be solved by calculating the following determinant:

$$\begin{vmatrix} J_m(k \cdot r_i) & N_m(k \cdot r_i) \\ J_m(k \cdot r_o) & N_m(k \cdot r_o) \end{vmatrix} = 0 \quad (2.11)$$

Different k -values (mode numbers) result from (2.11), which give information about the propagation of particular electromagnetic waves. These k -values depend on the order of the Bessel function m and the n^{th} root; therefore usually the mode number is expressed by k_{mn} . From the propagation constant γ and (2.6) the following three conditions can be deduced [38]:

- a) At low frequencies, ω is small, γ is real and the wave does not propagate;
 - b) At an intermediate frequency, ω is intermediate, $\gamma=0$, which is a transition condition (cutoff condition);
-

c) At high frequencies, ω is large, γ is imaginary and the wave propagates through the GIS.

As a result, for each k_{mn} value or mode number, the corresponding cutoff frequency can be determined from equation (2.6) with $\gamma=0$. The cutoff frequencies of the TM-modes up to 1800 MHz, which can propagate in the used laboratory setup of figure 3.10, are shown in figure 2.9 (solid bars).

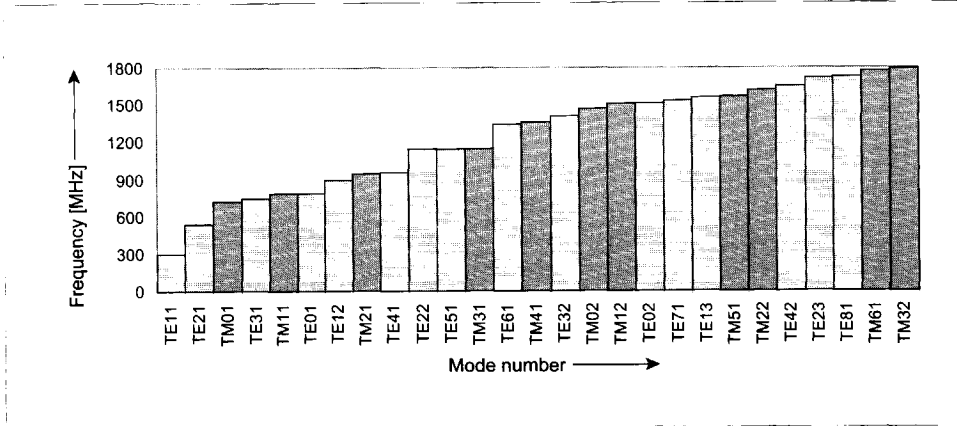


Figure 2.9: Cutoff frequencies for higher-order TE modes (striped bars) and TM modes (solid bars) for a GIS with conductor radius of $r_i=64$ mm and enclosure radius of $r_o=267$ mm.

In a similar way the cutoff frequencies of the TE-modes can be calculated by solving equation (2.12):

$$\begin{vmatrix} J'_m(k_{mn}r_i) & N'_m(k_{mn}r_i) \\ J'_m(k_{mn}r_o) & N'_m(k_{mn}r_o) \end{vmatrix} = 0 \quad (2.12)$$

The corresponding cutoff frequencies of the TE-modes are also displayed in figure 2.9, indicated by striped bars.

2.4.3 RESONANCES

TEM and higher-order TE and TM modes, propagating through the GIS, are partly absorbed in, and partly reflected and transmitted at discontinuities. Standing waves occur, which result in a measurable pattern

of resonance frequencies, for example as shown in the frequency spectrum of figure 2.11a. This spectrum was measured in a 2 m long part of the GIS between two spacers, see figure 2.10. To calculate the resonance frequencies, we investigated a similar part with length L as described by Kurrer [39].

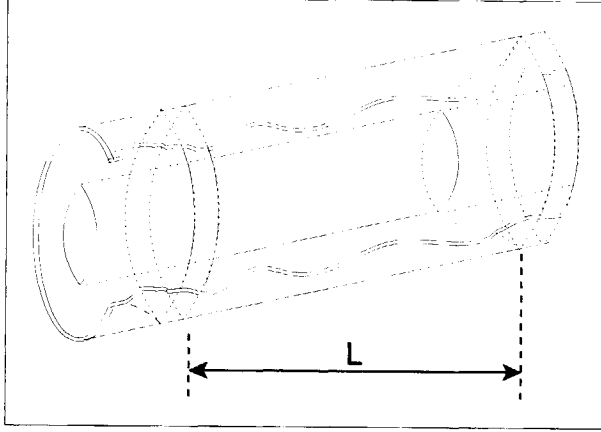


Figure 2.10: Possible resonance cavity inside a GIS, formed by two spacers and distance L between both spacers.

The electric-field and magnetic-field components can be described by (2.7). Looking only to the electric field component inside the cavity, forward and backward propagating waves occur, which are described by:

$$E_z = R_E(r) \cdot F_E(\varphi) \cdot (e^{-j\gamma z} - e^{+j\gamma z}) \quad (2.13)$$

in which $R_E(r)$ is only a function of r and $F_E(\varphi)$ is only a function of φ . This expression can be rewritten to:

$$E_z = R_E(r) \cdot F_E(\varphi) \cdot \frac{\sin(\gamma z)}{-2j} \quad (2.14)$$

To solve these equations, we assumed that the resonance cavity has two lossless aluminum hatch covers. As a result the electric field component has to vanish at both hatch covers and to fulfill these boundary conditions, $\sin(\gamma z)$ at $z=0$ and $z=L$ has to become zero, resulting in the following equation:

$$\gamma \cdot L = n \cdot \pi \rightarrow n = 1, 2, \dots \quad (2.15)$$

Using (2.6) the resonance frequencies can be calculated using:

$$f_{mnk} = \frac{1}{2\pi\sqrt{\varepsilon\mu}} \sqrt{\left(\frac{n\pi}{L}\right)^2 + k_{mn}^2} \quad (2.16)$$

The resonances in a 2 m long GIS enclosure have been calculated in order to estimate the possible frequencies of a frequency spectrum, see figure 2.11.

From figure 2.11 the following can be seen:

- 1) As indicated in the figure, the main spectral lines of the measured frequency spectrum can be estimated by calculation. However, at higher frequencies more and more modes are able to propagate and introduce many resonances. As a result, many frequencies can be expected.
 - 2) Some measured peaks occur at lower frequencies which are unexpected. However, we can explain these frequencies by the propagation of frequencies from other compartments. For example the measured peak of 115 MHz is introduced by the 0.65 m ($\frac{1}{4}\lambda$) compartment next to the investigated compartment of 2 m.
-

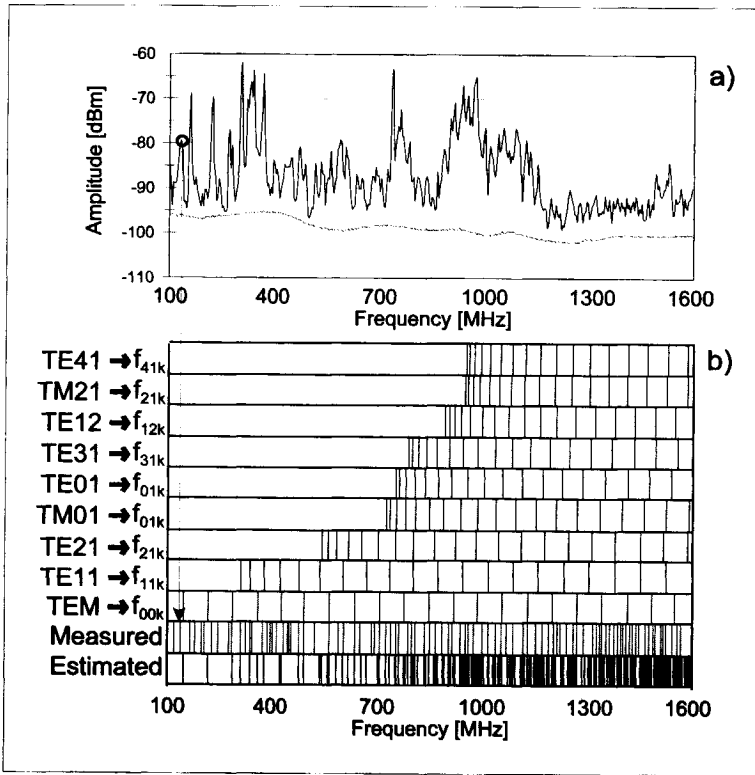
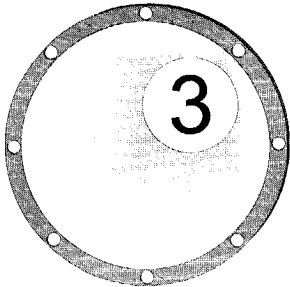


Figure 2.11:

- a) Measured frequency spectra from a free moving particle
- b) Comparison of all measured peaks in the frequency spectrum of a) with the calculated resonances (two lowest rows). The upper nine rows show the calculated resonance peaks for the TEM mode and first eight higher order modes.



CHAPTER 3 ADVANCED PD ANALYSIS

3.1 INTRODUCTION

Due to external noise, which is frequently present in the field (on-site), the use of a standardized measuring system according to IEC 60270 [12] is quite difficult. Moreover, often a part of the substation has to be de-energised in order to connect the measuring equipment. To solve this problem, we used a UHF PD detection system as shown in figure 3.1.

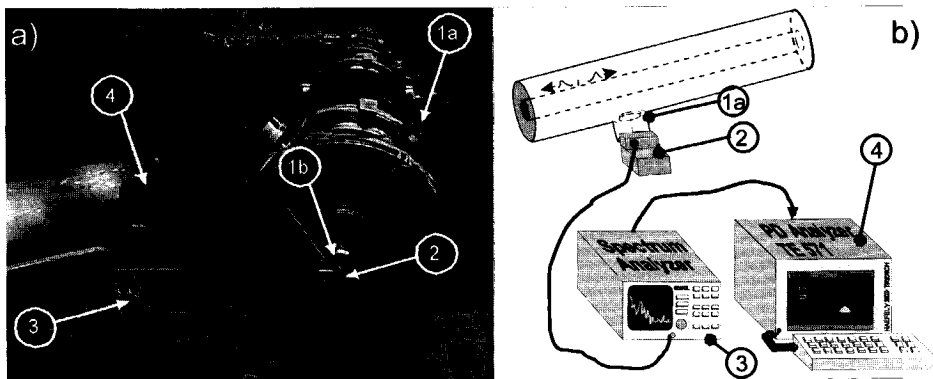


Figure 3.1: VHF/UHF measuring system consisting of:

1. UHF couplers 1a) internal;
 1b) external;
2. pre-amplifier;
3. spectrum analyser;
4. PC.

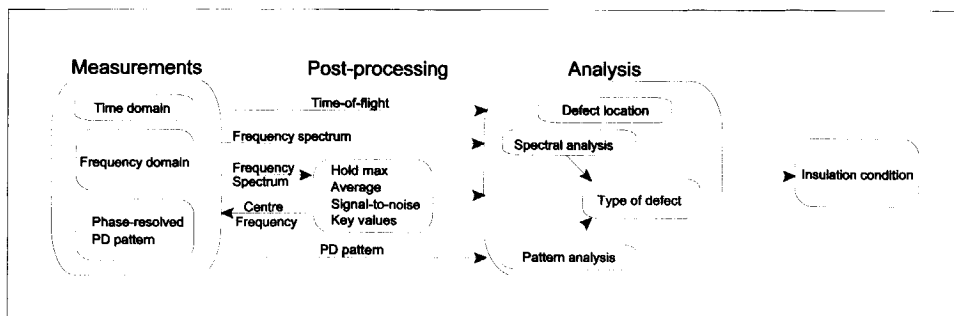


Figure 3.2: *UHF measuring procedure:*

- *Measurements in time domain, frequency domain or phase-resolved;*
- *Post-processing of obtained frequency spectra to obtain:*
 - *a centre frequency for a UHF phase-resolved measurement;*
- *Analysis to determine:*
 - *the defect location;*
 - *the type of insulation defect.*

Figure 3.2 shows the three different parts about the UHF measuring procedure which are described in this chapter: measurements, post-processing and analysis.

The UHF measuring technique makes use of the high-frequency electromagnetic waves (em-waves) excited by PD pulses [11, 17], as described in chapter 2. To pick up the em-waves, either internal or external UHF couplers (receiving antenna's) can be used. Recently, internal UHF couplers are usually mounted in new equipment and were also used for the measurements described in this thesis. However, in older substations, which have no internal UHF couplers mounted, other types of couplers, such as external spiral antennas or internal capacitive voltage sensors can also be used [40].

The signals picked up by the couplers are amplified by a 25 dB amplifier and measured by a spectrum analyser or fast oscilloscope, figure 3.1. As indicated in figure 3.2, three types of measurements have been performed:

1) Time domain

The pulse emitted by a PD source propagates in both directions along the GIS. As a result, the source may be located by measuring the time difference between the wave fronts arriving at UHF couplers on either side

of the PD source [11]. To measure the time difference of PD pulses in SF_6 that have rise times as short as tens of picoseconds and are travelling with approximately the speed of light, we used a fast digitizing oscilloscope with a 3 GHz bandwidth (Tektronix TDS 694C).

2) Frequency domain

A spectrum analyser analyses the coupler's signals in the frequency domain, to obtain a frequency spectrum (up to 1.8 GHz in case of the HP 8590L spectrum analyser we have used). In Appendix B, experiments are described, which have been performed to optimise the following important spectrum analyser settings: sweep time, total time of a measurement and post-processing.

3) Phase-resolved PD pattern

A spectrum analyser can also analyse the coupler's signals in the time domain, resulting in similar phase-resolved PD patterns that are obtained with a standardized measuring circuit, see chapter 5. For this purpose we used the SA to demodulate the signals into the range of a few MHz (3 MHz in case of the HP 8590L) in the following way:

- The centre frequency f_c of the SA is set to the selected measuring frequency,
- The measured span is set to zero: the zero span mode of the SA,
- The sweep time is set to 20 ms and synchronised with the voltage source to obtain PD patterns correlated to the 50 Hz sine wave.

3.2 SIGNAL PROCESSING OF UHF SPECTRA

It is known that for proper use of a spectrum analyser, the input signal has to be continuous and stable in magnitude, pulse shape etc. [66]. A PD pulse however, cannot be considered as a stable input signal. As described in Appendix B, we measured 20 sweeps using a sweep-time of 5 seconds and a resolution bandwidth of 3 MHz. In case a UHF frequency spectrum of a section in the gas-insulated system under investigation has been determined accordingly, the information on active partial discharge (PD) sources has to be revealed. In this section, post-processing techniques of the information gained during several sweeps in the measuring period are described. As a result, a suitable centre frequency f_c can be selected to measure a phase-resolved PD pattern.

3.2.1 MAX HOLD FREQUENCY SPECTRUM

Usually a stable frequency spectrum is processed from the maximum amplitudes over the series of sweeps as shown in figure 3.3a and 3.3b. This method is most suitable to detect PD pulses with a low repetition rate (≤ 50 Hz) because every detected pulse will be recorded. This implicates also a disadvantage of this method because high random peaks are treated similarly, which can strongly influence the processed frequency spectrum. Another disadvantage is that nothing can be concluded about the number of the detected pulses at peaks in the frequency spectrum.

Figure 3.3a shows a processed frequency spectrum from the maximum amplitudes over the series of twenty sweeps and is not influenced by large peaks. Figure 3.3b shows the same spectrum, however, in this case a large peak at 550 MHz can clearly be seen in the spectrum compared to figure 3.3a. Usually, this frequency peak will be selected for further analysis in the time domain, but, as will be discussed below, this frequency peak turns out to be an improper choice for PD analysis in time domain.

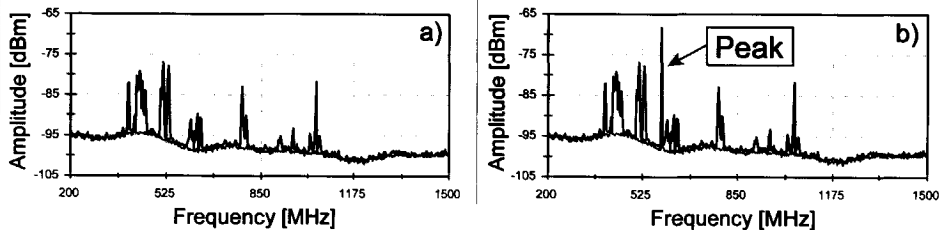


Figure 3.3: Post-processed frequency spectra of a protrusion fixed to the high-voltage conductor using max hold of 20 sweeps of 5 seconds:

- a) not influenced by a high peak;
- b) influenced by a high peak.

3.2.2 AVERAGED FREQUENCY SPECTRUM

Therefore, we prefer to process a stable frequency spectrum by averaging the amplitudes over the series of sweeps as shown in figure 3.4a and 3.4b. This method is in particular suitable for situations with a high PD repetition rate (> 50 Hz). The advantage of this method is that it effectively suppresses high randomly occurring peaks as shown in figure 3.3b, because the measured signals at each frequency are averaged over all X

sweeps. The amplitude of a random peak will be reduced to $(1/X)^{\text{th}}$ of its original size.

Figure 3.4a shows the processed spectrum, where the amplitudes have been averaged over the series of twenty sweeps. Compared to the processed frequency spectrum shown in figure 3.3a, the peaks are reduced by approximately 9 dB. In theory single peaks would be reduced by 26 dB. This means that the measured peaks are rather stable and occur in most of the 20 measured sweeps. Figure 3.4b also shows the averaged frequency spectrum. Compared to figure 3.3b, the high peak is strongly reduced by 22 dB (this reduction approaches the theoretically reduction of 26 dB). As a result, it can be concluded that this is a high single peak and, in contrast to the impression given by the max hold spectrum of figure 3.3b, the 550 MHz peak should not be chosen for a PD measurement.

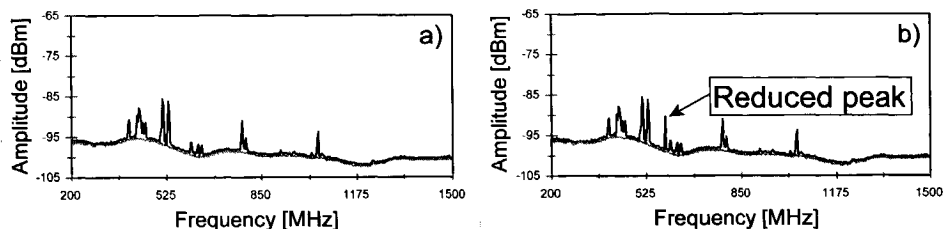


Figure 3.4: Post-processed frequency spectra of a protrusion fixed to the high-voltage conductor using averaging of 20 sweeps of 5 seconds:

- a) not influenced by a high peak;
- b) influenced by a high peak.

Table 3.1: Comparison of the hold max and average methods to process frequency spectra.

	Hold max	Average
PD process repetition rate	< 50 Hz	> 50 Hz
Random peak reduction	no reduction	reduction
Coupler level signal	maximum value	average value

If we compare both processed frequency spectra shown in figures 3.3b and 3.4b, it is clear that the large peak visible in figure 3.3b has been reduced

by 22 dB by the averaging method. In practice, the max hold method is often used. As demonstrated above, it can be advantageous to process both the max hold and averaged spectra. Peaks in the max hold spectrum which are substantially reduced in the averaged spectrum indicate non-repetitive phenomena and have to be excluded from further analysis in the time domain. Table 3.1 summarizes this comparison.

3.2.3 SIGNAL-TO-BACKGROUND NOISE RATIO SPECTRUM

In the previous sections we discussed two post-processing methods to determine the origin of peaks in the frequency spectrum: continuous pulses or high random pulses. In this section we post-process the signal-to-background noise frequency spectra in order to separate continuous noise and PD activity.

First the background noise level is measured, figure 3.5a. Then the GIS system is energized and the signal spectrum is measured, figure 3.5b. It is clear that the small noise peaks indicated with the dotted lines are also present in the PD spectrum. Therefore, under laboratory conditions, we process the ratio between both spectra resulting in the frequency spectrum shown in figure 3.5c. As a result, mainly peaks from PD activity are visible after this processing.

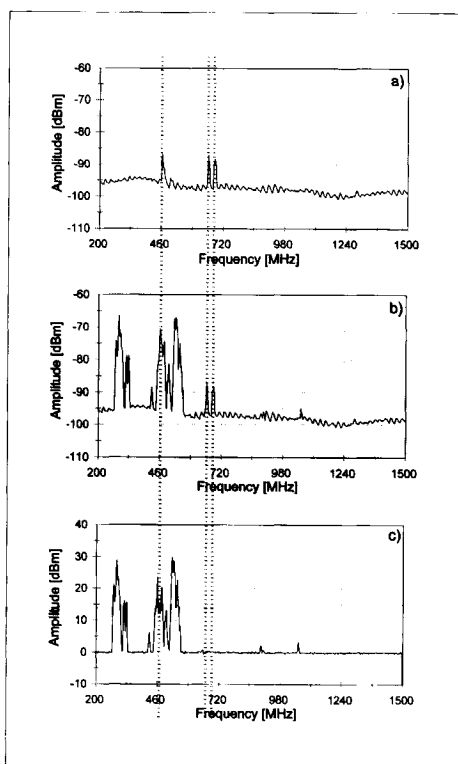


Figure 3.5: Noise suppression under laboratory conditions:

- a) Background-noise spectrum showing three noise peaks, indicated by the dotted lines;
- b) PD spectrum showing two of the noise peaks; the third is obliterated by a signal peak;
- c) The ratio of both spectra.

3.3 TIME-OF-FLIGHT ANALYSIS

Figure 3.6 shows the principles of the time-of-flight analysis to determine the defect location from time-resolved measurements [13].

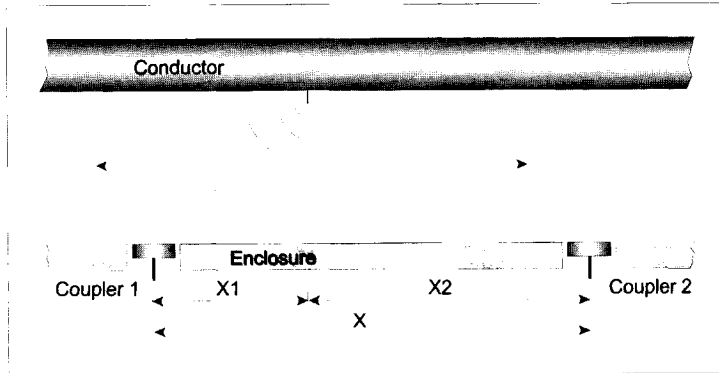


Figure 3.6: The principles of defect location using time-of-flight measurements. The pulses emitted by the PD source are picked up by couplers 1 and 2. From the difference in arrival time between both couplers the location of the defect can be calculated.

The distance X_1 between coupler 1 and the PD source can be calculated with equation (3.1):

$$\begin{cases} t_1 = \frac{X_1}{v} \\ t_2 = \frac{X - X_1}{v} \end{cases} \quad \Delta t = t_2 - t_1 \rightarrow X_1 = \frac{X - v \cdot \Delta t}{2} \quad (3.1)$$

where X is the distance between both couplers, Δt is the difference in the arrival time of the signal at coupler 2 and coupler 1 and v is the propagation velocity of the signal, described by

$$v = \frac{1}{\sqrt{\mu_r \cdot \mu_0 \cdot \epsilon_r \cdot \epsilon_0}} \quad (3.2)$$

In case of a gas, the propagation velocity approaches the speed of light. But in a medium of permittivity ϵ_r , such as spacers, the propagation velocity

is decreased by a factor $\sqrt{\epsilon_r}$. For GIS the propagation velocity can be written in terms of the characteristic impedance Z by

$$v = Z \cdot \underbrace{\frac{2\pi}{\ln\left(\frac{r_o}{r_i}\right)}}_k \cdot \frac{1}{\mu_r \cdot \mu_0} = k \cdot Z \quad (3.3)$$

In other words, the propagation velocity is proportional to the characteristic impedance.

Using time-of-flight measurements, the defect location could be determined within 20 centimetres. So using this method, the GIS compartment containing the PD source can be determined very accurately.

3.4 AMPLITUDE ANALYSIS OF UHF SPECTRA

Lets consider two important PD sources occurring in GIS: a protrusion fixed to the HV conductor and a free moving particle. Both defects produce spectral characteristics, which have to be discerned by spectral analysis. The spectral behaviour has to be compared with other known spectra, to which purpose we defined so-called key values in this section and statistical analysis in section 3.5.

For example, we measured the frequency spectra for:

- different defects (figure 3.7a and 3.7b);
- different UHF couplers: coupler B is an improved version of coupler A (figure 3.7b and 3.7c);
- different coupler locations (figure 3.7b and 3.7d).

The spectra have been processed from 20 sweeps with a sweep time of 5 seconds using the averaging method.

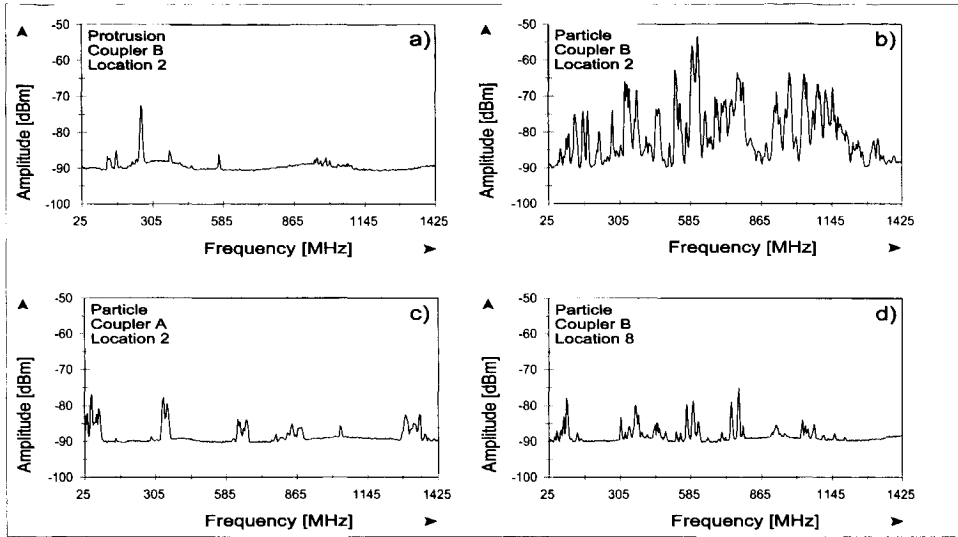


Figure 3.7: Examples of PD frequency spectra obtained using two different couplers at different coupler locations, see figure 3.10:

- a) 15 mm protrusion fixed to the high-voltage conductor with a PD magnitude of 5 pC, measured with coupler type B at location 2
- b) free particle of 25 pC measured with coupler type B at location 2
- c) free particle of 25 pC measured with coupler type A at location 2
- d) free particle of 25 pC measured with coupler type B at location 8

As shown in figures 3.7b and 3.7d the GIS components between the discharging source and the connected UHF coupler attenuate the magnitude of the measured signal. To investigate this effect, we propose four spectral key values to collect information about the amplitudes of the measured signal. In the telecommunications it is common to use decibels as a measure for spectral measurements. A decibel is defined as the logarithmic ratio between the power of the measured signal and 1 mW [41]:

$$dBm = 10 \cdot \log\left(\frac{P_{measured}}{1mW}\right) \quad (3.4)$$

From a frequency spectrum which is built up from N data points ($N=400$ in case of a HP8590L), sampled during one sweep these key values are processed in the following way.

– Measured power in the frequency spectrum (MP)

For the MP key value, all N measured amplitudes S_i from the spectrum are quadratically summed and converted into [dBm]. This key value is proportional to the measured power in the frequency spectrum [41]:

$$MP = 10 \cdot \log \left(\sum_{i=1}^N S_i^2 \right) \quad (3.5)$$

– Average power in the frequency spectrum (AP)

This key value is also a measure of power in the frequency spectrum, however after smoothening neighbouring amplitudes. All N measured amplitudes S_i and S_{i+1} are averaged, squared, summed, divided by the number of data points and converted into [dBm]:

$$AP = 10 \cdot \log \left(\sum_{i=1}^N \left(\frac{S_i + S_{i+1}}{2} \right)^2 \cdot \frac{1}{N} \right) \quad (3.6)$$

– Maximum amplitude of the frequency spectrum (MA)

This key value is the maximum amplitude of the measured spectrum.

$$MA = 20 \cdot \log \left(\max(S_i)_{i=1}^N \right) \quad (3.7)$$

– Averaged area per data point (AR)

This key value is the averaged area of the post-processed signal-to-noise-ratio frequency spectrum (resulting in a series of processed amplitudes S'_x). All N processed amplitudes S'_i and S'_{i+1} of the measured frequency spectrum are averaged, summed and divided by the number of data points:

$$AR = \sum_{i=1}^N \left(\frac{S'_i + S'_{i+1}}{2} \right) \cdot \frac{1}{N} \quad (3.8)$$

We calculate these four key values for the full measured frequency span or for a specific part of the frequency spectrum representing PD activity. In the following three possible applications of the key values are described.

Example 1) *Relation of the PD magnitude measured in pC and dBm*

The amplitude key values have been calculated for the typical spectra of four different defects shown in figure 3.8. Again, the spectra have been processed from 20 sweeps with a sweep time of 5 seconds using the averaging method. Table 3.2 gives a comparison between the amplitude of the frequency spectra measured with the UHF method and the PD magnitude measured in pC according to [12].

Table 3.2: *Comparison PD magnitude measured in pC and the key values calculated from the frequency spectra shown in figure 3.8 (FP is free particle, HV is high-voltage protrusion, FE is floating electrode, LV is low-voltage protrusion).*

	PD magnitude	MP [dBm]	AP [dBm]	MA [dBm]	AR [mV]
FP	25 pC	17.6	-8.4	37.3	3.9
HV	5 pC	-2.4	-28.4	17.1	0.05
FE	2000 pC	32.3	6.3	57.3	9.5
LV	5 pC	-2.6	-28.7	13.6	0.05

We conclude that there is no clear relation between the PD magnitude measured in pC and the values processed from the UHF frequency spectra using the key values. It depends strongly on the type of measured defect and on the location of the defect. E.g. a free particle of 25 pC has much more power in the frequency spectrum than a fixed protrusion of 5 pC. This can be interpreted by the fact that the number of partial discharges from a fixed protrusion is much higher compared to a free moving particle. Due to a certain integration time used in the standardized measuring circuit, several PD pulses from the fixed protrusion can be integrated leading to a higher reading of the standardized measuring circuit. Since the spectrum analyser captures the maximum UHF signal (so no integration of adding up of several pulses), the particle will show higher amplitudes in the frequency spectrum than the fixed protrusion. However, to determine the condition of the insulation, the most important factors are the defect-type, the location of the defect, the PD process and probability for over-voltages, and not the PD magnitude as such.

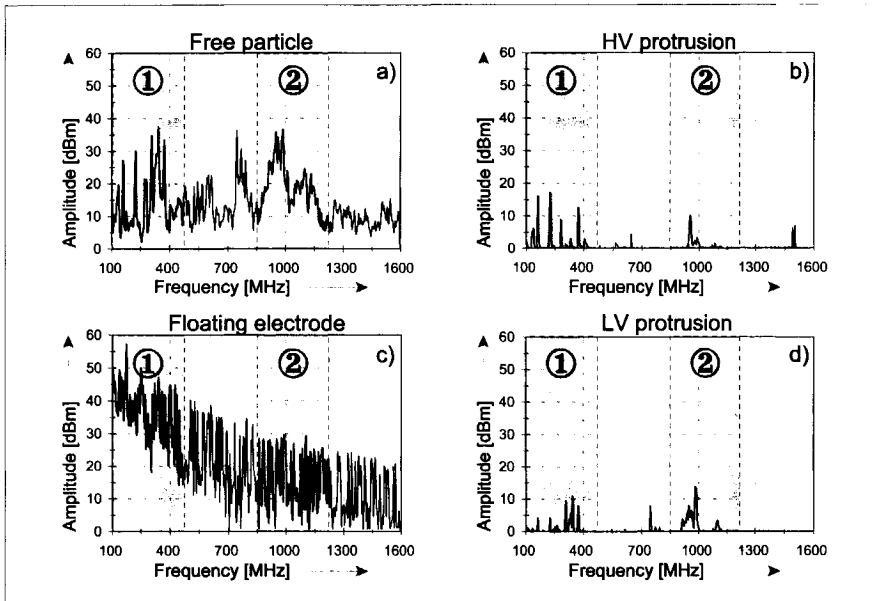


Figure 3.8: Signal-to-noise-ratio spectra measured for different defects using the same configuration:

- 1) Free moving particle
- 2) Protrusion fixed to the high-voltage conductor
- 3) Electrically floating electrode at the high-voltage conductor
- 4) Protrusion fixed to the enclosure

Example 2) Discrimination between insulation defects

Figure 3.8 shows two shaded frequency spans ① and ②. Frequency span ① is between 100 MHz and 475 MHz and frequency span ② is between 850 MHz and 1125 MHz. Comparison of both spans shows that the amplitudes of the frequency spectra of an electrically floating electrode and of the protrusion fixed to the conductor are greater in span ① than in span ②. The amplitudes of the frequency spectra of the free particle and the protrusion fixed to the enclosure are greater in span ② than in span ①. We have observed that the location of the protrusion (high-voltage conductor or enclosure) has an influence on the frequency spectrum. This confirms the fact that frequencies in the low-frequency region (TEM modes) are easy to excite at the inner conductor while the high-frequency region (TE modes) is easy to excite at the enclosure [42].

For easy comparison of the measured power in the frequency span of both shaded areas in the frequency spectra, we processed the key value AR in both areas. In figure 3.9 the key value AR in the high-frequency span ② (V_H) is plotted against the key value AR in the low-frequency span ① (V_L).

After plotting the line $V_H = V_L$ it is possible to distinguish two groups:

Group 1: $V_H > V_L$ (the ratio of V_H and V_L is greater than 1)

In this group frequency spectra from the free particle and protrusion fixed to the enclosure (LV protrusion) are situated. Both PD processes occur at the enclosure side and, as stated above, shows that frequencies in the high-frequency region (TE and TM modes) are easier to excite at the enclosure.

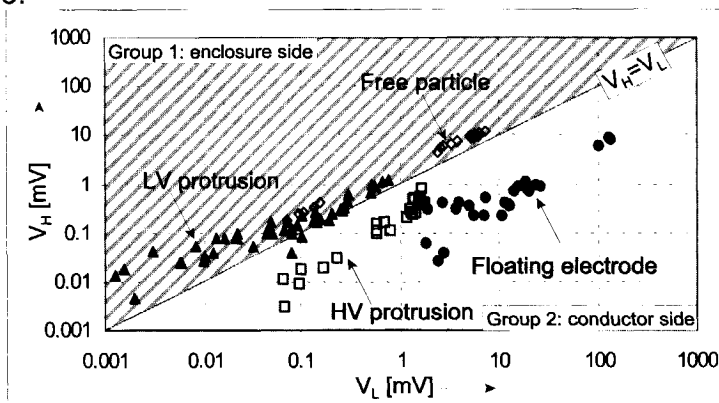


Figure 3.9: By comparing the key value AR in the low-frequency span V_L (between 100 MHz and 475 MHz) and high-frequency span V_H (between 850 MHz and 1225 MHz) it is possible to distinguish two groups of frequency spectra: originating from defects on the high-voltage conductor or on the enclosure.

Group 2: $V_H < V_L$ (the ratio of V_H and V_L is smaller than 1)

In this group frequency spectra from the electrically floating electrode and protrusion fixed to the high-voltage conductor (HV protrusion) are situated. These PD processes occur at the central conductor and, again as stated above, shows that frequencies in the low-frequency region (TEM modes) are easier to excite at the central conductor.

So we can use key values for discrimination between some defects. To improve frequency-spectra-based discrimination we added statistical analysis of frequency spectra, which will be described in section 3.5.

Example 3) Analysis of propagation effects

A 380 kV GIS (Alstom, Fluobloc T155) laboratory setup has been used to model PD sources, to create reference data for different insulation defects and to study the risk of insulation defects, see figure 3.10.

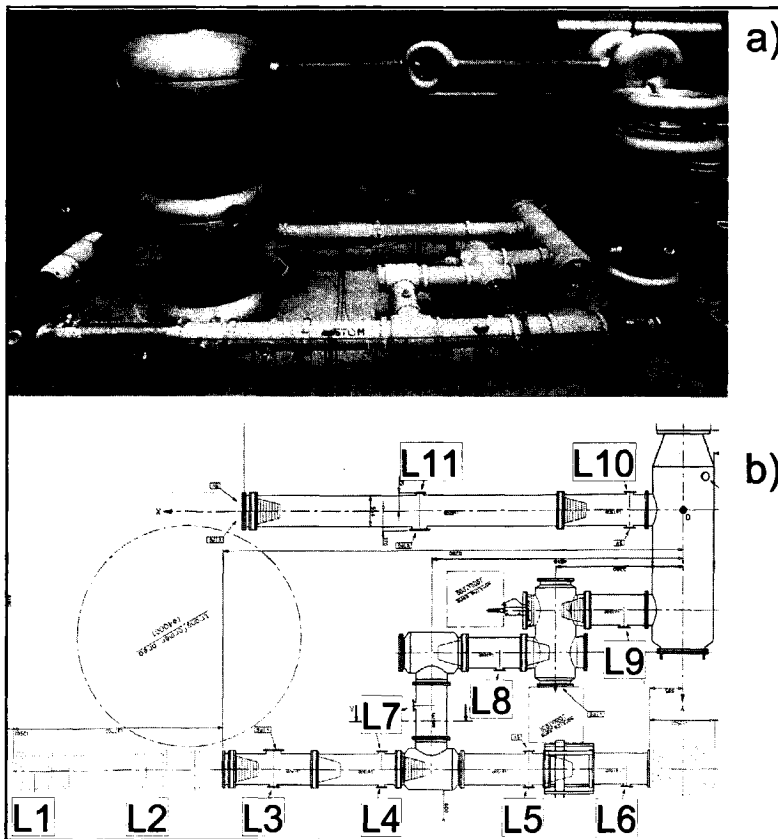


Figure 3.10: Laboratory setup as used for the measurements described in this thesis. The test setup comprises different busbar lengths (1, 1.4, 1.5, 2, and 6.5 metres), a T-junction, a bend, a disconnecter, a circuit breaker and a current transformer.

To find correlations between on-site and laboratory tests, we used the same type of equipment in the laboratory as in the 380 kV substation in Meeden, The Netherlands, where we performed many on-site measurements. To investigate the influence of GIS components on the UHF PD signals, the setup is equipped with eleven UHF couplers. Because the high-frequency signals are influenced differently by the different GIS components, we mounted UHF couplers before and after each GIS component, see figure 3.10.

The key value AR has been calculated from the frequency spectra of a free moving particle (located at position 1) at different coupler locations. As expected, the value of this key value decreases with increasing distance between the source and the coupler, see figure 3.11.

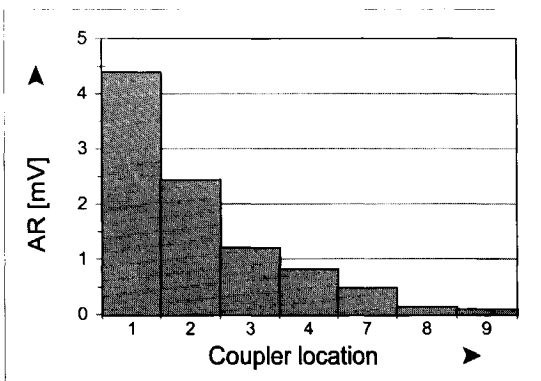


Figure 3.11: Influence of the distance between the PD source and the UHF coupler analysed using the key value AR.

3.5 STATISTICAL ANALYSIS OF FREQUENCY SPECTRA

In the previous section we showed that it is possible to distinguish two groups of frequency spectra (thus two groups of different defects) using the ratio of key values processed for two frequency spans. However, clear differences between the frequency spectra of defects in the same group can be seen. In this section, we investigate the use of statistical analysis of typical frequency spectra to discriminate defects in the same group.

Consider the frequency spectrum which consists of a series of amplitudes S_i , having a set of peaks K_i . A peak is locally defined as $K_i = S_i$ if

$$(S_i > S_{i-1}) \wedge (S_i > S_{i+1}) \quad (3.9)$$

We used two kinds of windows for further analysis:

- 1) Amplitude windows
- 2) Frequency windows

3.5.1 AMPLITUDE WINDOWS

The range of amplitudes of the frequency spectrum is divided into N windows, with a window size Δa of

$$\Delta a = \frac{K_{\max} - K_{\min}}{N} \quad (3.10)$$

in which

$$\begin{cases} K_{\max} = \text{MAX}(K_j)_{j=1}^m \\ K_{\min} = \text{MIN}(K_j)_{j=1}^m \end{cases} \quad (3.11)$$

So now the following amplitude windows A_i can be defined by (3.12):

$$\begin{cases} A_1 = [K_{\min}, K_{\min} + \Delta a) \\ A_2 = [K_{\min} + \Delta a, K_{\min} + 2 \cdot \Delta a) \\ \vdots \\ A_N = [K_{\min} + (N - 1) \cdot \Delta a, K_{\max}] \end{cases} \quad (3.12)$$

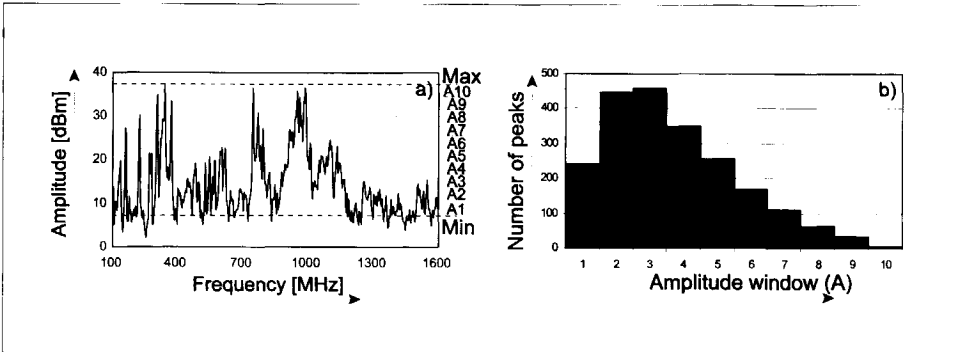


Figure 3.12: Amplitude window analysis:

- a) Division of the frequency spectrum into ten amplitude windows
- b) The resulting amplitude distribution vs. amplitude-window number.

In figure 3.12a the division of the frequency spectrum into $N=10$ windows is shown; figure 3.12b shows the resulting distribution.

3.5.2 FREQUENCY WINDOWS

The measured frequency span is divided into M frequency windows in which the average amplitude of peaks is calculated. A frequency window is defined by

$$\Delta f = \frac{\text{Stopfrequency} - \text{Startfrequency}}{M} \quad (3.13)$$

So now the following frequency windows F_i are defined by

$$\begin{cases} F_1 = [\text{Startfrequency}, \text{Startfrequency} + \Delta f] \\ F_2 = [\text{Startfrequency} + \Delta f, \text{Startfrequency} + 2 \cdot \Delta f] \\ \vdots \\ F_M = [\text{Startfrequency} + (M - 1) \cdot \Delta f, \text{Stopfrequency}] \end{cases} \quad (3.14)$$

In each of these frequency windows, the average of the peaks is defined by

$$AF_k = \frac{\sum_{j=1}^{x_k} K_{kj}}{x_k} \quad (3.15)$$

where x_k is the total number of peaks in span F_k .

The processing of the frequency spectrum of figure 3.13a using frequency windows with $M=20$ leads to the histogram spectrum of figure 3.13b. In addition, for further analysis we apply the amplitude window method to this histogram spectrum. In figure 3.13b the division of the frequency spectrum into $N=10$ amplitude windows is shown. Figure 3.13c shows the resulting distribution.

Although the same frequency spectrum as shown in figures 3.12a and 3.13a is analysed, the processed distributions differ. The defined distribution as shown in figure 3.12b and 3.13c can be analysed further by applying statistical moments [16]. In this way we can characterise a frequency spectrum by a few numbers only.

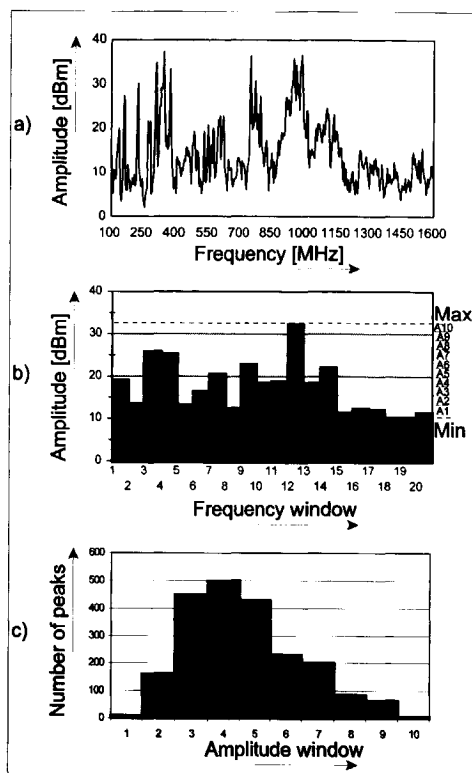


Figure 3.13: Frequency window analysis:

- a) Division of the frequency spectrum into $M=20$ frequency spans;
- b) Spectrum translated into twenty average values;
- c) The resulting distribution.

For example, the characterisation of the spectra of two typical frequency spectra of a free moving particle and a protrusion fixed to the high-voltage conductor is demonstrated in figure 3.14.

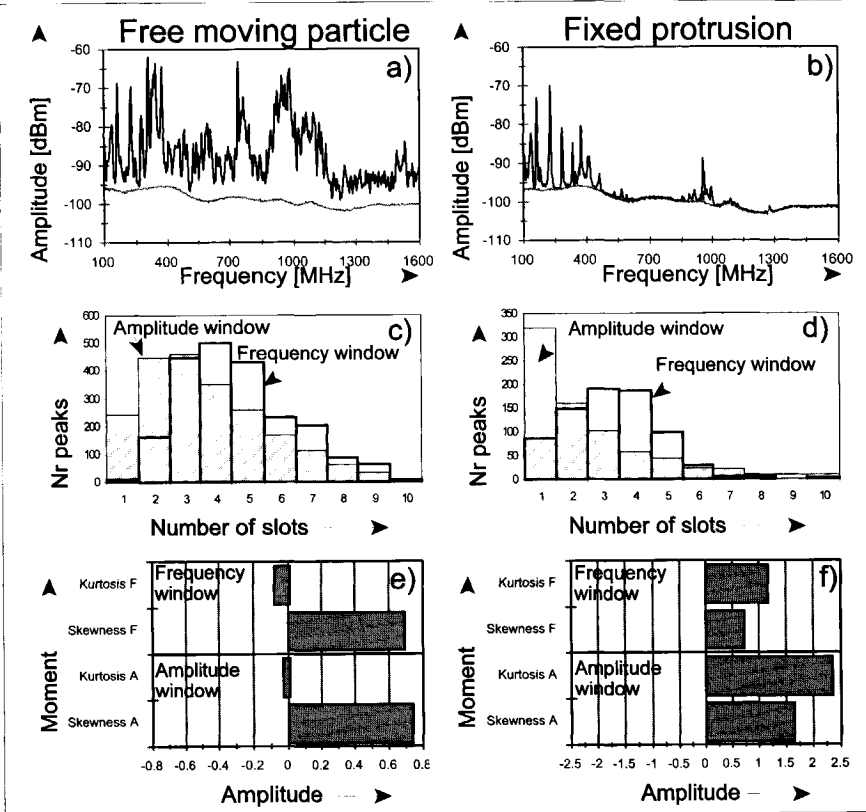


Figure 3.14: Example of statistical analysis of frequency spectra:

- a) Spectrum of a free moving particle
- b) Spectrum of a protrusion fixed to the HV conductor
- c) Distributions of a free moving particle
- d) Distributions of a protrusion fixed to the HV conductor
- e) Characterisation of a free moving particle
- f) Characterisation of a fixed protrusion

To discriminate between both spectra, we used statistical analysis. The distributions based on the amplitude-window method and on the frequency-window method are shown in figure 3.14c for a free moving particle and in figure 3.14d for the fixed protrusion.

The 3rd (skewness) and 4th (kurtosis) statistical moments have been processed for these four distributions to analyse the shape of the distributions, figure 3.14e and 3.14f. A clear difference between both characterisations can be seen, which means that it is possible to discriminate between different spectra and, in this case, between different defects.

After analysis of many measurements we had to conclude that these four quantities do not provide enough information to discriminate between occurring defects. Therefore, we also applied the statistical moments to the low-frequency span and to the high-frequency span as indicated in figure 3.8. Also the ratio of the UHF signal in the low frequency span and in the high frequency span is used. As a result, the frequency spectra are characterised by a feature vector consisting of thirteen parameters.

3.6 ANALYSIS OF PHASE-RESOLVED PD PATTERNS

It is known that a relationship exists between the shape of phase-resolved PD patterns and the discharge source (type of defect) [22]. Each discharging defect with its geometry, location in insulation, dielectric properties and local field is characterized by a specific PD sequence. Analysis of these sequences has shown to be a good means to distinguish the different discharge sources [22]. The PD pulses are grouped with respect to intensity and phase angle using digital processing. Different phase-resolved PD distributions or patterns can be processed, for example:

- 1) $H_{q_{max}}(\varphi)$: distribution of maximum discharge values
- 2) $H_{q_n}(\varphi)$: distribution of average values of discharges
- 3) $H_n(\varphi)$: distribution of the number of discharges
- 4) $H(q)$: distribution of discharge magnitude
- 5) $H(p)$: distribution of discharge energy magnitude
- 6) $H_q(\varphi, n)$: 3-dimensional distribution of discharge value

After a PD measurement has been finished, further analysis of the obtained phase-resolved PD patterns comprised two steps: feature extraction and statistical analysis [22-47].

Feature extraction aims to reduce the dimensionality of the PD patterns by processing characteristic properties from the PD pattern [43]. In this thesis, statistical features, such as skewness and kurtosis, have been used to derive a so-called 'fingerprint' as described by Gulski [16] or feature vector.

Further analysis of these derived fingerprints is classification and discrimination. The purpose of discrimination is to find groups of similar fingerprints. These fingerprints can be used to create a database consisting of different defects. The purpose of classification is to determine the similarity of a fingerprint processed from a new measurement with a data base containing fingerprints of known defects.

Several techniques for discrimination of fingerprints, such as mapping techniques, cluster analysis and fractal features are described in [43, 45]. In this thesis only cluster analysis has been used. Cluster analysis

tries to recognise groups in a number of feature vectors without a priori knowledge. A detailed description of clustering techniques can be found in [43, 45]. Figure 3.15 shows a simplified example how cluster analysis works. Here five feature vectors consisting of one feature are analysed. First, the two vectors a and c which have the smallest distance (i.e. which are the most similar) are connected, see figure 3.15a. They are replaced by one new feature vector, for instance by taking the average. In this way, the number of vectors is decreased by one. These steps are repeated until the last vectors are connected, see figure 3.15b-d.

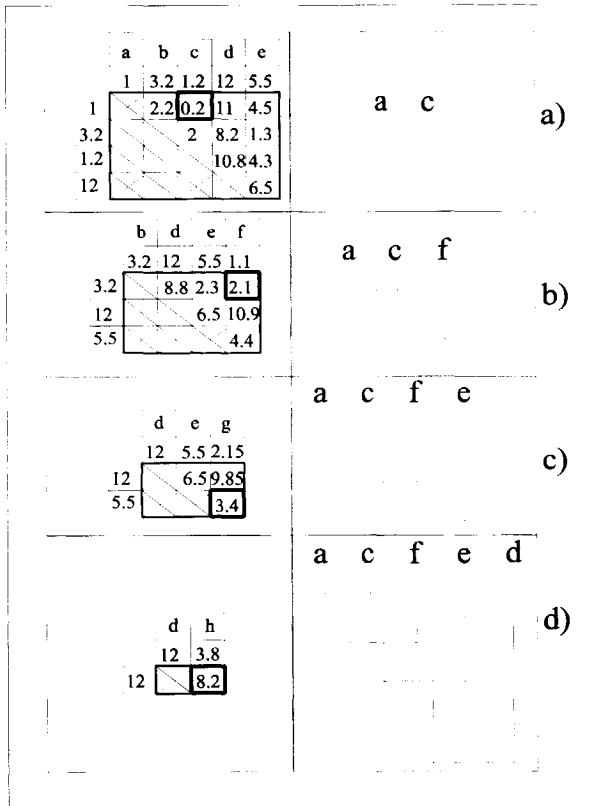


Figure 3.15: Example of cluster analysis of fingerprints using the tree structure as obtained from different defects [48].

For classification of PD measurements the centour score method has been used in this thesis [43, 45]. This method uses fingerprint populations of known discharge defects in a database. It compares the fingerprint of the new PD measurement with the centre of each population. The centour score is defined as the percentile rank of the fingerprints that are further away from the centre of the known discharge population than the fingerprint of the new PD measurement. This has been illustrated in figure 3.16.

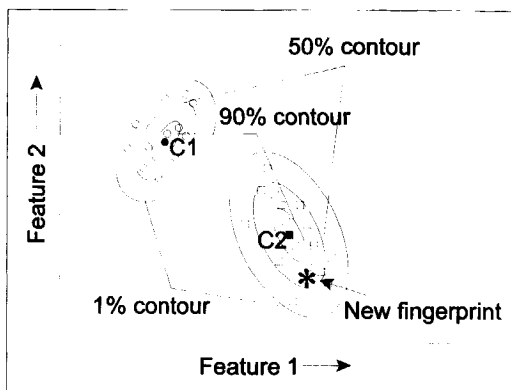


Figure 3.16: Border formation with the centour score method. ○: fingerprints of defect A (center C1); □: fingerprints of defect B (center C2) [43].

An example of the outcome of the PD pattern classification of an on-site measured PD pattern with a database developed in the laboratory, is shown in figure 3.17.

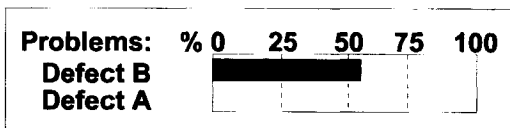


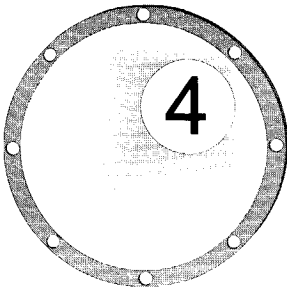
Figure 3.17: Outcome of the PD pattern classification using the centour score method of an on-site obtained PD pattern with a laboratory developed database.

3.7 CONCLUSIONS

We have shown that application of post-processing techniques, such as processing a frequency spectrum by averaging several sweeps, improves the possibility to recognise the occurrence of random and intermittent noise peaks in the measuring results. If the background noise frequency spectrum can be measured and is stable in time, the processing of the signal-to-noise ratio frequency spectrum can further improve the discrimination between spectral peaks from noise and PD pulses.

Key values have been defined, which were used to describe the amplitude and power of the measured frequency spectra. It was shown that there is no unique relation between the PD magnitude measured in pC and the spectral content. By comparing key values processed for the low-frequency span and the high-frequency span of the frequency spectra we could discriminate between two classes of PD sources. It also allows us to demonstrate the attenuation effect during the propagation of electromagnetic waves through the GIS.

The discrimination between different PD sources based on spectral analysis, has been refined by assessment of statistical parameters. As a result, frequency spectra have been characterized by a feature vector consisting of thirteen features. This enabled us to discriminate between different defects, such as fixed protrusions, free particles and electrically floating electrodes.



CHAPTER 4
SENSITIVITY OF THE UHF
MEASURING CIRCUIT

The magnitude of the electromagnetic waves (em-waves) propagating through GIS components is reduced, mainly due to attenuation and reflections. The attenuation of the signals due to ohmic losses in the conductors is very small; average values for the first 4 propagation modes (TE: 01, 11, 21 and 31 and TM: 01, 11, 21 and 31) are shown in table 4.1 [21, 39].

Table 4.1: Overview of typical attenuation values due to ohmic losses for different propagating modes as known from literature.

	TEM	TE($f > f_c$)	TM ($f > f_c$)
Kurrer [39]	2..3 dB/km	0..4 dB/km	3..10 dB/km
Wanninger [21]	0..3 dB/km	1..2 dB/km	4..6 dB/km

As stated by Hampton, in practice rather high signal reductions of 1-2 dB/m have been measured, which cannot only be attributed to ohmic losses [8, 21, 39]. In the following, the reduction of the waves propagating through a GIS due to reflections at different discontinuities inside the GIS is analysed. Using transmission line modelling, the positions of UHF couplers could be determined to ensure a certain sensitivity of the UHF measuring circuit.

4.1 REFLECTION AND TRANSMISSION OF EM-WAVES

As shown in chapter 2, electromagnetic waves can propagate through GIS by many different modes. Moreover, each of these modes is influenced by discontinuities in the GIS, which can be described by transmission line modelling. Each model is also frequency dependent and due to the many possible propagation modes, the resulting model will be rather complex.

To model the influence of a discontinuity we use the notation shown in figure 4.1 [35]. Signals propagating into the z-direction have only transverse components of the electric and magnetic fields.

These transverse components of the electric and magnetic field at the boundary have to be continuous, which is described by [35]:

$$\begin{cases} \hat{E}_i + \hat{E}_r = \hat{E}_t \\ \hat{H}_i + \hat{H}_r = \hat{H}_t \end{cases} \quad (4.1)$$

Using transmission line models to describe each discontinuity, it is possible to define reflection and transmission coefficients. The reflection and transmission coefficients depend on the differences in impedances at the discontinuity. It is known from [36] that the impedances for the different modes in different materials can be calculated by:

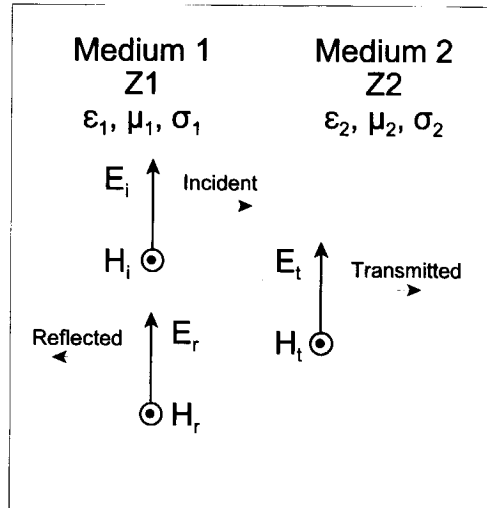


Figure 4.1: Reflection and transmission of electromagnetic waves at an interface of two different materials.

$$\begin{cases} Z_{TEM} = \sqrt{\frac{\mu}{\epsilon}} \cdot \frac{\ln(r_o/r_i)}{2\pi} \\ Z_{TM} = \sqrt{\frac{\mu}{\epsilon}} \cdot \sqrt{1 - \left(\frac{f_c}{f}\right)^2} \cdot \frac{\ln(r_o/r_i)}{2\pi} \\ Z_{TE} = \sqrt{\frac{\mu}{\epsilon}} / \sqrt{1 - \left(\frac{f_c}{f}\right)^2} \cdot \frac{\ln(r_o/r_i)}{2\pi} \end{cases} \quad (4.2)$$

in which Z_{TEM} , Z_{TM} and Z_{TE} are the characteristic impedances in case of respectively TEM-wave, TM-wave or TE-wave propagation, f_c is the cutoff frequency of the wave-mode and r_i and r_o are the inner respectively outer radii. As a result, the reflection and transmission coefficient for the discontinuity shown in figure 4.1 can be calculated by:

$$\begin{cases} r = \frac{E_r}{E_i} = \frac{Z_2 - Z_1}{Z_2 + Z_1} \\ t = \frac{E_t}{E_i} = \frac{2 \cdot Z_2}{Z_2 + Z_1} \end{cases} \quad (4.3)$$

where r is the reflection coefficient, t the transmission coefficient and Z_1 and Z_2 the impedances as indicated in figure 4.1.

4.2 SIGNAL REDUCTION CAUSED BY A SPACER

One of the most occurring elements in a GIS is the spacer. In this section we investigated the propagation of em-waves through one or two spacers.

4.2.1 TRANSMISSION LINE MODEL OF A SPACER

To define a transmission line model of a spacer, we have modelled the conical spacer by a disk in a similar way as Kurrer [39]. However, to include the influence of resonances, we modelled a larger GIS section as shown in figure 4.2. Here, six points of interest have been indicated:

- points ① and ④ are the positions of the UHF couplers C_1 resp. C_2 where the signals are measured;
- points ②-③ and ⑤-⑥ are the GIS-spacer transitions.

Each of these points is defined as a discontinuity and each discontinuity can be described by a reflection r and transmission t coefficient, which have also been indicated in figure 4.2.

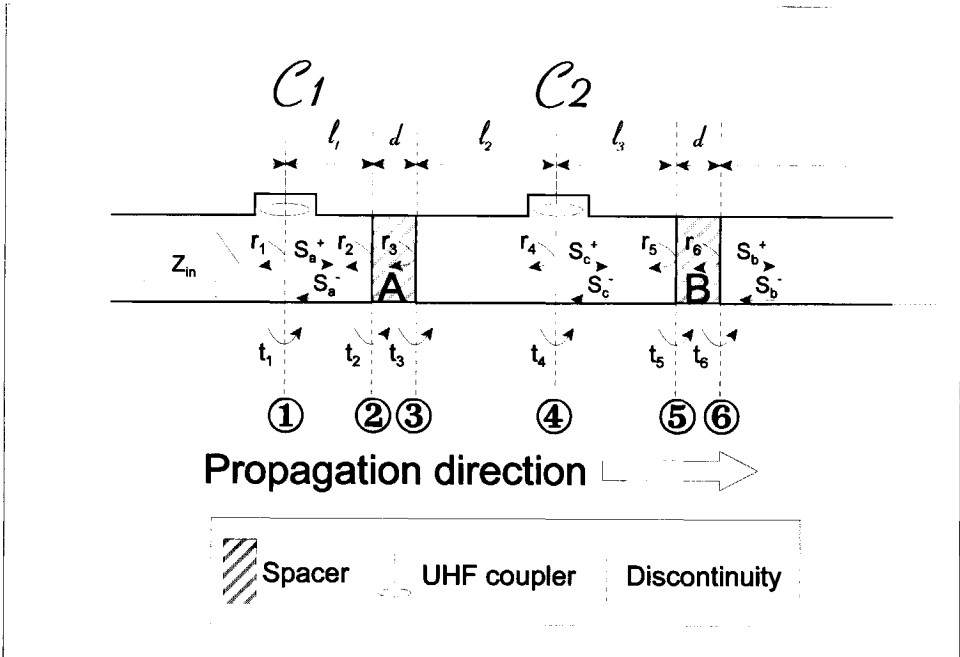


Figure 4.2: Model to investigate the influence of a spacer on em-waves propagating from coupler C_1 to coupler C_2

To determine the influence of spacer A, assume that the em-waves are propagating in the direction from UHF coupler C_1 to UHF coupler C_2 . The first discontinuity which the em-waves encounter is coupler C_1 (discontinuity ①). Because there is no change in impedance at this discontinuity, no reflection of the waves will occur. Therefore, reflection coefficient r_1 equals zero ($r_1=0$) and the transmission coefficient t_1 equals one ($t_1=1$).

Then the em-waves arrive at discontinuity ② which is spacer A. At this discontinuity the waves will be partly reflected (r_2) and partly transmitted

(t_2). Also part of the waves will be absorbed, however, this corresponds to about 1% of the signal attenuation which has been observed for spacers. At discontinuity ③ again reflection and transmission of the waves occur. Due to reciprocity it can be stated that $r_3 = -r_2$. Then the waves arrive at coupler \mathcal{C}_2 . However, after ℓ_3 metres the waves encounter spacer B and will be partly reflected at discontinuities ⑤ and ⑥. This results in backward propagating waves S_c^- , which add up with the forward propagating S_c^+ waves. So the signal measured at coupler \mathcal{C}_2 is not only due to forward propagating waves, but also due to backward propagating waves. Therefore, this second spacer B also has to be taken into account in order to estimate the signal at coupler \mathcal{C}_2 . After spacer B an infinitely long tube has been assumed so no backward propagating waves will occur there.

All these discontinuities result in a complex combination of backward and forward travelling waves, which all have to be taken into account for the calculation of the signals at UHF couplers \mathcal{C}_1 and \mathcal{C}_2 . It is known that each discontinuity in figure 4.2 can be characterised by a scattering or wave-transmission chain matrix [50]:

$$\begin{bmatrix} S_a^+ \\ S_a^- \end{bmatrix} = \prod_{i=1}^n A_i \begin{bmatrix} S_b^+ \\ S_b^- \end{bmatrix} \quad (4.4)$$

where $n=6$ in our case and the scattering matrices are defined as

$$A_i = \frac{1}{t_i} \begin{bmatrix} e^{\gamma_i \cdot d_i} & r_i e^{-\gamma_i \cdot d_i} \\ r_i e^{\gamma_i \cdot d_i} & e^{-\gamma_i \cdot d_i} \end{bmatrix} \quad (4.5)$$

With this formula we calculated the change in the signals propagating through the spacer between both couplers as is shown in figure 4.3. The following can be concluded:

- 1) The change in the propagating em-waves depends on the frequency of the propagating wave;
 - 2) Depending on the frequency, attenuation or amplification of the em-waves can be expected;
 - 3) Amplification of the em-waves is due to the resonances which occur between both spacers;
-

- 4) Around 1000 MHz, the signal reduction is negligible. This means that the waves are fully transmitted so that the impedance seen at the entrance of the spacer Z_{in} equals the impedance of the GIS. This occurs if half of the wavelength of the propagating em-wave fits in the thickness of the spacer. Then the transmission through the spacer equals 1 at the following frequencies:

$$f = \frac{k}{2d\sqrt{\mu\epsilon}} \quad k = 1, 2, 3, \dots \quad (4.6)$$

in which $\mu = \mu_0$, $\epsilon = \epsilon_r \epsilon_0$ with $\epsilon_r = 5.3$ and d is the thickness of the spacer ($d = 0.064$ m), resulting in the following frequencies:

$$f = 1017 \cdot k \text{ [MHz]} \quad k = 1, 2, 3, \dots \quad (4.7)$$

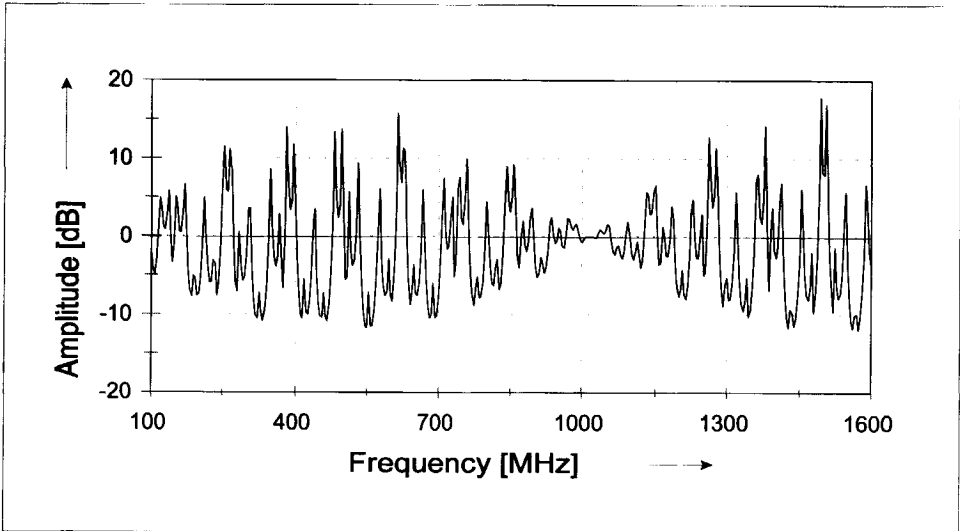


Figure 4.3: The change in the frequency spectrum by one spacer modelled using the configuration shown in figure 4.2, with $l_1 = 1.2$ m, $l_2 = l_3 = 3.25$ m and $d = 0.064$ m.

We analysed the result of figure 4.3 experimentally in figure 4.4. Here the frequency spectrum measured before the spacer is shown. Next to this spectrum, the measured and estimated frequency spectra after propagating through one spacer are shown.

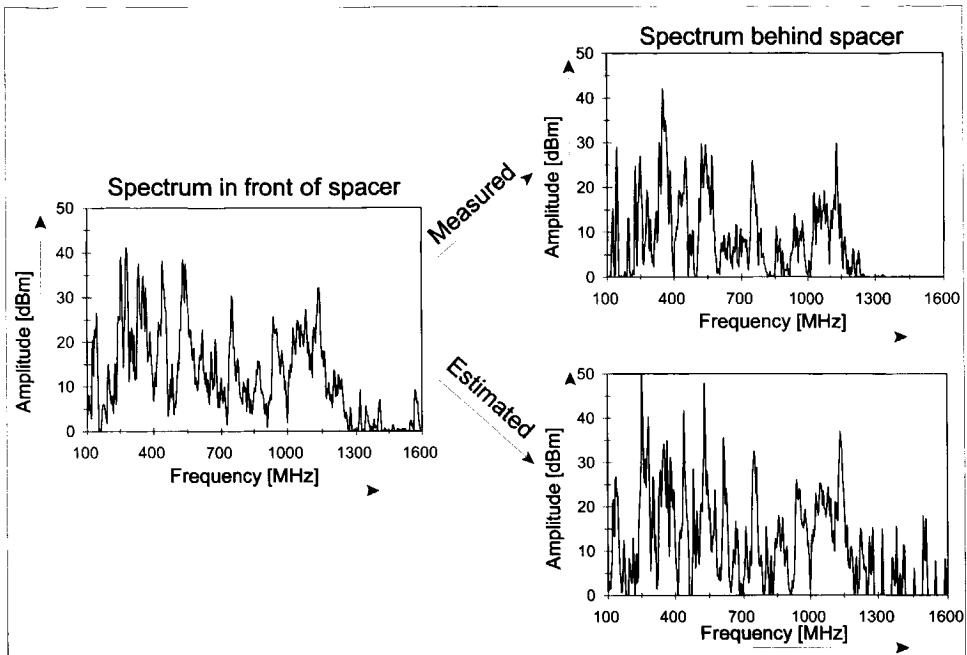


Figure 4.4: *Measured frequency spectrum in front of the spacer and the measured and estimated frequency spectra after the em-waves traversed one spacer.*

In figure 4.4 can be seen that the measured and estimated frequency spectra show differences. On the whole, the estimated spectrum looks bigger than the measured spectrum. We can conclude that:

- the amplification of waves due to resonances we estimated and showed in figure 4.3 is too high. In contrast, the measured spectrum shows reduction at almost all frequencies.
- As expected, the estimated spectrum is almost not changed around 1000 MHz. However, the measured frequency spectrum shows reduction in this frequency range. This can be explained by the assumption of lossless wave propagation.

In Appendix C, a method to further analyse the measured and estimated frequency spectra is described.

4.2.2 TRANSMISSION LINE MODEL OF TWO SPACERS

In a similar way the influence of two spacers on the propagating em-waves has been determined according to the model shown in figure 4.5a. The signal change introduced by two spacers is shown in figure 4.5b. Compared to figure 4.3, the following differences can be seen:

- less resonances, because the lengths of the tubes are smaller;
- the em-waves are more attenuated.

Like in figure 4.3, almost no change can be concluded around 1000 MHz.

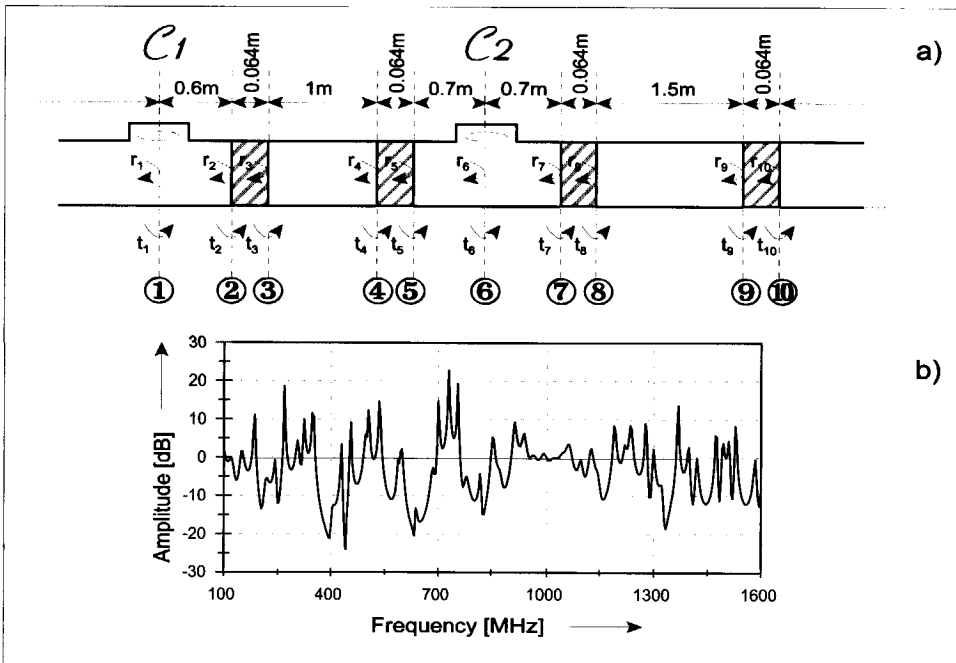


Figure 4.5:

- a) Model used to investigate the influence of two spacers on em-waves propagating from coupler C_1 to coupler C_2 ;
- b) The modelled change in the frequency spectrum by two spacers.

We analysed the result of figure 4.5 experimentally in figure 4.6. Here the frequency spectrum measured before the spacer is shown. Next to this spectrum, the measured and estimated frequency spectra after propagating through two spacers are shown.

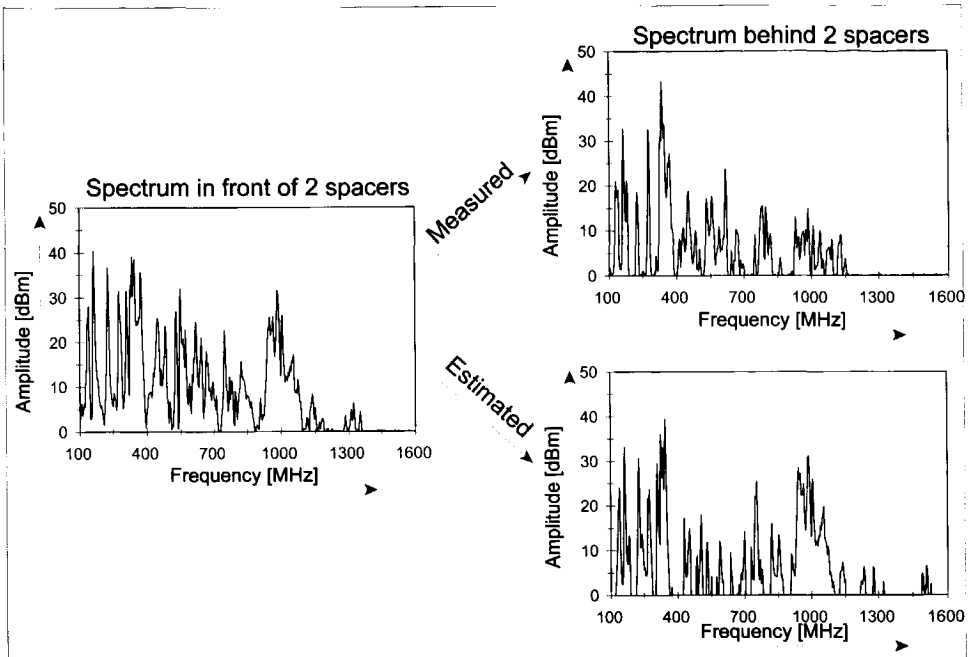



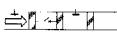
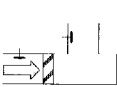





Figure 4.6: *Measured frequency spectrum in front of the first spacer and the measured and estimated frequency spectra after the em-waves traversed two spacers.*

In figure 4.6 can be seen that the measured and estimated frequency spectra mainly show a large difference in the frequency span around 1000 MHz. This can be explained by the small signal change which has been estimated in this frequency span, as can be seen in figure 4.5b. We can conclude that using a disk model instead of the real cone-shaped spacer is too simple to estimate propagation of em-waves. Therefore, we investigated the propagation effects in GIS using measurements. Appendix C describes a procedure how we calculated the reflection and transmission coefficient for each GIS component. A summary of the results is given in section 4.3.

4.3 REFLECTION COEFFICIENTS OF GIS COMPONENTS

From the performed measurements, we calculated the reflection coefficients of each GIS component following the procedure which is described in Appendix C. The results are summarised in table 4.2. As shown in Appendix C the reflection coefficient for a spacer theoretically calculated using a model and processed from a series of measurements are similar. We used the ratio of the measured signal before the spacer and after the spacer as indicated in the table to process the reflection coefficient. From measurements in other configurations the ratio of the measured signals before and after the other components have been used to process their corresponding reflection coefficients.

Table 4.2: Overview of the reflection coefficients of different GIS components.

Component	Config	Reflection	Component	Config	Reflection
Spacer		-0.35	Circuit breaker		-0.67
Bend		-0.41	T-junction		+0.02
		-0.60			-0.41
Dis-connector		-0.66	Bushing		-0.65

4.4 COMPARISON SIGNAL REDUCTION FROM ARTIFICIAL AND PARTIAL DISCHARGE PULSES

Next we have to investigate how far signals are comparable, which are received from artificial sources (injected in the GIS) and from realistic partial discharge sources. Therefore, we analysed PD measurements from free particles and fixed protrusions to verify the previously obtained signal reduction (ratio of the voltage measured before the spacer and measured after the spacer) results for a spacer. The defects were investigated under different conditions such as the type of gas (pure SF_6 or $\text{SF}_6\text{-N}_2$ mixture) and gas pressure. Figure 4.7 shows the probability distributions of the ratio of incoming waves and outgoing waves for a spacer: one distribution obtained for artificial pulses and one distribution obtained for partial discharge pulses. Because the artificial pulses are very stable in amplitude and pulse-shape, the distribution is rather narrow. In contrast, the distribution of partial discharge pulses is broad because partial discharge pulses are rather unstable and change from pulse to pulse. However, the distributions overlap and a correlation of 0.98 was calculated.

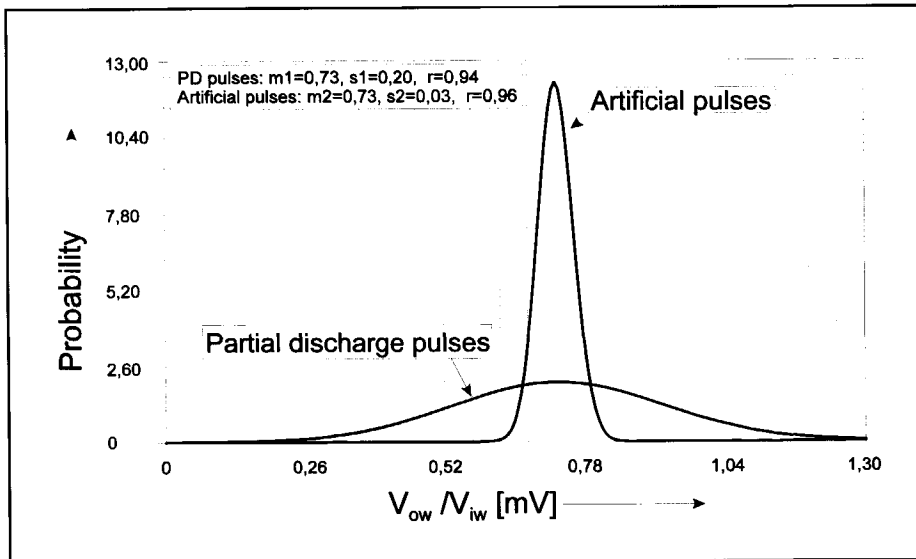


Figure 4.7: Comparison of the distributions of the signal reduction measured using artificial pulses and partial discharge pulses from free particles and fixed protrusions for the spacer between location 3 and 4.

4.5 SIGNAL REDUCTION OF GIS

In the previous sections, the signal reduction of GIS components has been investigated. As a result, the change in the UHF magnitude by a GIS component in a particular configuration is known. It is interesting to investigate the possibility to combine these signal reductions of single GIS components to estimate the total signal reduction of more complex GIS sections and for field applications.

4.5.1 GIS SECTIONS

In this section the signal reduction of different GIS sections, consisting of several GIS components, is estimated. For this purpose we used the estimated reflection coefficients summarised in table 4.2. The estimated values are verified using experiments with similar GIS configurations.

As an example, we estimated the signal reduction between coupler locations 8 and 11 of the laboratory setup shown in figure 3.10. In this case artificial pulses are injected in the UHF coupler at location 7 and measured at UHF couplers at location 8 and 11, see figure 4.8.

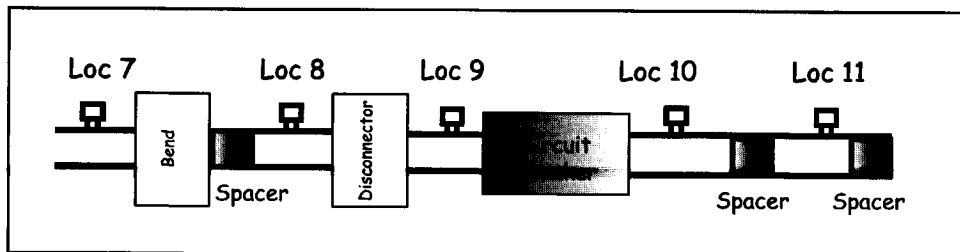


Figure 4.8: Model of the GIS part from location 8 to location 11. Each component has been substituted by its corresponding scattering matrix to calculate the signal reduction between location 8 and 11.

The pulses injected at the UHF coupler at location 7 result in em-waves which propagate into the direction of coupler 8. At location 8 we measured a frequency spectrum with a key value (MP) of 9.7 dB. The scattering matrix of each discontinuity has been determined using equation (4.5) and the reflection coefficients summarised in table 4.2. Using equation (4.4) the signal reduction of the GIS section between couplers 8 and 11 was

calculated: 7 dB. As a result, the UHF signal measurable at the UHF coupler at location 11 was estimated to be 2.7 dB.

To validate this result, we measured the UHF signal at the UHF coupler at location 11: 1.3 dB. This means that the measured signal reduction between the couplers at location 8 and 11 is 8.4 dB. The signal reduction could be estimated with an accuracy of 15%. This accuracy can be explained by the fact that the estimated reflection coefficients summarised in table 4.2 have an accuracy of 5%.

4.5.2 A REAL SUBSTATION

We performed a similar investigation as described in section 4.5.1 on-site in the 380 kV substation in Meeden, The Netherlands. So we injected pulses in one of the UHF couplers, estimated the signal reduction of the GIS section under investigation and compared the result with actual measured data. Figure 4.9 shows the different configurations in the substation which have been used for the tests.

The following GIS section types have been analysed:

- 1 between couplers B and C:
lengths of 8 m (phase 1) or 10 m (phase 2 and 3), bend, current transformer (phase 3), lengths of 8 m (phase 1) or 3 m (phase 2 and 3);
- 2 signals propagating from B to A:
lengths of 10 m, spacer, lengths of 10 m (phase 1) or 9 m (phase 2) or 8 m (phase 3);
- 3 signals propagating from D to E
lengths of 3 m, disconnector, lengths of 3 m, disconnector;

The results are summarised in table 4.3.

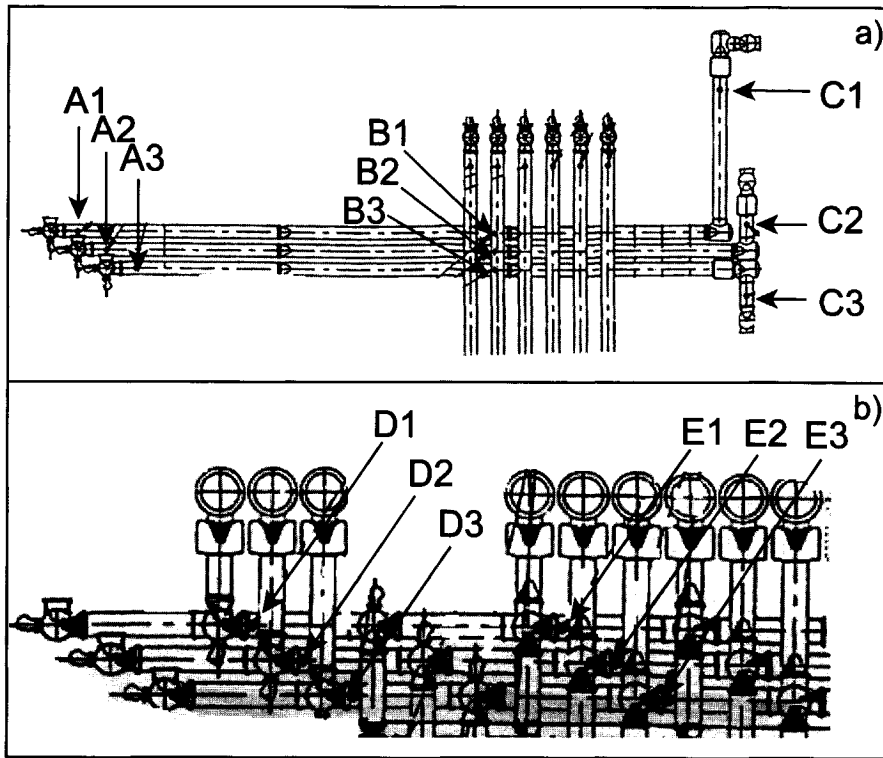


Figure 4.9: Two parts of the 380 kV substation in Meeden, which have been used to estimate the signal reduction of GIS sections consisting of:
a) spacers, a bend and a current transformer
b) two disconnectors
in which A_x , B_x , C_x , D_x and E_x are UHF couplers and $x=1,2,3$ is the phase in which the UHF coupler is located.

As can be seen in figure 4.9, three almost identical configurations have been investigated for each type of GIS section. In several situations, large differences between estimated and measured signal reduction values can be observed. On the whole, the error in the estimated signal reduction (compared to the measured signal reduction) is larger compared to the estimated signal reduction of GIS sections investigated in the laboratory setup described in section 4.5.1.

Table 4.3: Comparison of the signal reduction calculated from the reflection coefficients and from experiments.

Section type	Input Location	Output Location	Measured signal reduction [dB]	Estimated signal reduction [dB]	Busbar reduction [dB/m]	Adjusted busbar reduction [dB/m]
1	B1	C1	9.4	7.2	0.2	-0.1
	B2	C2	14.9	7.3	0.6	0.3
	B3	C3	12.3	7.3	0.3	0.1
2	B1	A1	2.8	1.2	0.1	-0.2
	B2	A2	9.0	1.2	0.4	0.2
	B3	A3	2.3	1.2	0.1	-0.2
3	D1	E1	3.8	5.8	-0.3	-0.6
	D2	E2	9.8	5.8	0.7	0.4
	D3	E3	7.0	5.8	0.2	0.0
Average busbar reduction [dB/m]:					0.2	0.0

The GIS sections of type 2 have long busbars and only one spacer. In the laboratory setup only short parts have been investigated and the influence of the length of busducts was negligible. Moreover, in almost all investigated configurations (except once for type 3) the estimated signal reduction is smaller compared to the measured signal reduction. This observation can imply that the influence of length plays a bigger role on-site compared to the relatively small laboratory setup.

From the measured signal reduction values, an average busbar reduction of 0.2 dB/m could be estimated as shown in the 6th column of table 4.3. This value has been used to correct the estimated signal reduction. Although there are still differences between the measured and adjusted estimated signal reduction values (as shown in the 7th column of table 4.3), the average busbar reduction is reduced to 0 dB/m. However, an average busbar signal reduction of 0.2 dB/m is large compared to the values

mentioned at the beginning of this chapter (< 0.01 dB/m) which can be explained by additional resonances.

4.6 SENSITIVE POSITIONING OF UHF COUPLERS

4.6.1 COUPLER LOCATIONS

It has been shown that each GIS component influences the amplitude of the em-waves propagating through the GIS. As a result, em-waves excited by partial discharge activity somewhere in the GIS will result in different UHF signals if measured at different coupler locations. Moreover, couplers located at a certain distance away from the PD source will measure nothing. Therefore, several UHF couplers have to be mounted in a GIS taking the following into account:

- 1) Ensure enough sensitivity in the full setup to detect all partial discharges of given type and magnitude.
- 2) Use as few UHF couplers as possible in order to minimise the costs.

The used procedure to position the UHF couplers with a 5 pC sensitivity in GIS comprises the following steps:

- 1) Determine the required sensitivity of the measuring setup according to the IEC 60270 recommendations (5 pC) [12];
- 2) Determine the corresponding magnitude of the signal measured using a UHF measuring circuit;
- 3) Determine the maximum allowable signal reduction which still ensures detection of the defect with above specified sensitivity;
- 4) Using the transmission line models as described before, the full GIS setup is divided into sections which have a signal reduction as close as possible to the maximum allowable signal reduction taking a certain safety factor into account. A UHF coupler has to be located before and after each of these GIS sections.

Table 4.4 shows the measured UHF signal levels and measured in pC according to [12] for fixed protrusions and free particles. We can conclude that both defects giving the same PD magnitude give completely different results when measured with the UHF technique. For example, the UHF signal for a partial discharge of 5 pC generated by a protrusion is 0.05 mV, whilst the UHF signal of a partial discharge of 5 pC generated by a free moving particle is 0.66 mV.

Table 4.4: *The value of UHF signals as measured for a HV protrusion and a free particle compared to the measured PD magnitudes in pC.*

		PD Magnitude (IEC 60270)			
		5 pC	8 pC	18 pC	23 pC
UHF signal [mV]	Type of defect				
	Protrusions	0.05	0.07	0.24	0.35
	Free Particle	0.66	0.88	2.47	3.90

The UHF detection circuit has enough sensitivity if the detecting UHF couplers are located in such a way, that partial discharge activity of 5 pC can be detected at any location in the setup [51]. Moreover, the UHF measuring equipment has a lower detection limit of 0.01 mV. So we can accept a reduction of the signal by a factor of 5 between the fixed protrusion and the detecting coupler. In case of free particles we can accept a reduction of the signal between the particle and the detecting coupler by a factor of 66.

Because the allowable signal reduction differs for both defects, we can estimate the coupler locations for both defects. In both cases the first coupler is situated near the circuit breaker, as indicated in figure 4.10:

- coupler-number 1 inside the square for fixed protrusions and
- coupler-number 1 inside the circle for free particles.

To determine the location of the next required coupler in case of fixed protrusions, we defined a GIS section between this coupler and coupler 1 consisting of the disconnector. The signal is reduced in this GIS section by a factor of 1.7, which is less than the maximum allowable signal reduction. So we can enlarge the GIS section until we reach a signal reduction by a factor 5. As a result we need a second coupler as indicated by the 2 inside the square in figure 4.10. For this setup we have sufficient sensitivity to detect a 5 pC fixed protrusion using two UHF couplers.

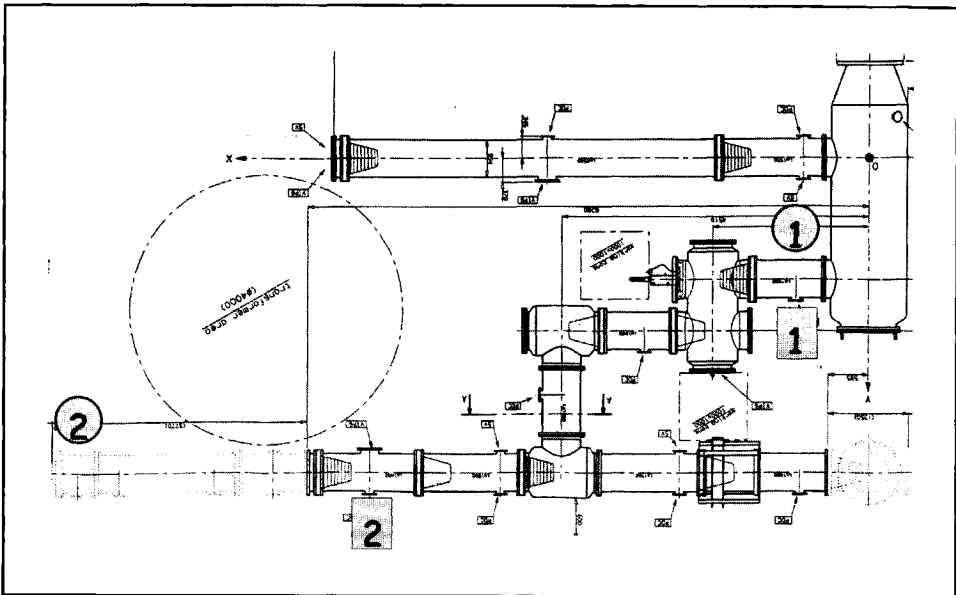


Figure 4.10: The UHF coupler positions to guarantee enough sensitivity to detect partial discharge activity of 5 pC:

- two couplers in case of a protrusion fixed to the high-voltage conductor which are indicated by squares;
- two couplers in case of free moving particles which are indicated by the circles.

We repeated the above described procedure for a free moving particle. Also in this case two couplers are necessary to detect a free moving particle in this setup which are indicated in figure 4.10 by 1 and 2 inside a circle. So we can conclude that, depending on the type of defect that has to be detected, the number and location of the UHF couplers change. This means that to reach enough sensitivity to detect all defects with 5 pC magnitude, the worst case has to be taken into account; i.e. the defect which radiates the smallest UHF signals: fixed protrusions. Protrusions, however, are in most cases removed during commissioning testing. As stated before, free particles are the main cause of breakdown. Therefore, it is recommended to optimise the number and locations of the couplers for free particles.

4.6.2 CIGRE SENSITIVITY CHECK

In the previous section we determined the necessary locations of UHF couplers to have sufficient sensitivity to detect free particles and fixed protrusions with a PD magnitude of 5 pC. To check the proposed locations we applied the sensitivity check proposed by the CIGRÉ WG 15/33.03 [51]. For this sensitivity check a two-step procedure is followed:

Step 1: Laboratory tests

The laboratory tests comprise the following parts:

- Introduce a PD level of 5 pC in a representative GIS setup. Position the discharge source near coupler 1 (figure 4.11);
- Use a spectrum analyser to measure the frequency spectrum of the discharges at coupler 2;
- Inject artificial pulses in coupler 1 with an amplitude $V_{\text{artificial}}$; this has to result in a UHF signal similar to the UHF signal from the PD source which has been checked by comparing the key-values for both spectra. As a result $V_{\text{artificial}}$ corresponds for this particular setup (GIS and VHF/UHF detection circuit) a sensitivity of at least 5 pC.

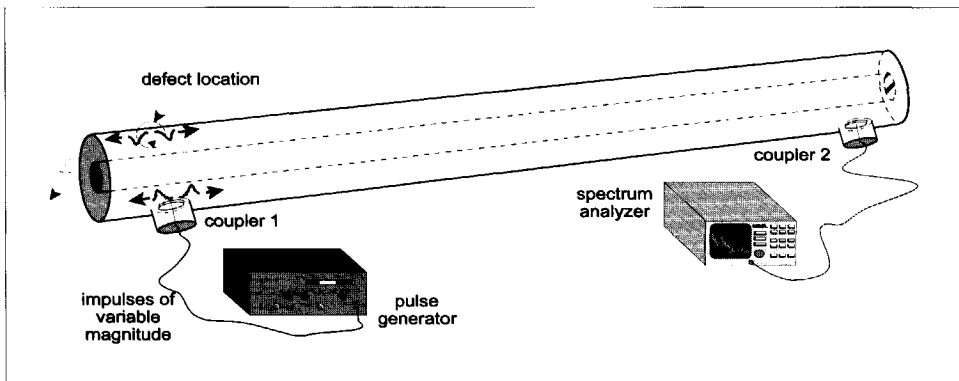


Figure 4.11: Laboratory setup for measuring the UHF signal magnitude of an artificial defect.

Step 2: On-site tests

GIS of the same type can now be checked on site by injection of $V_{\text{artificial}}$ pulses in one coupler. If the pulses are detected on the neighbouring couplers the 5 pC sensitivity between both couplers for this GIS section has been proved on site.

4.6.2.1 STEP 1: LABORATORY TESTS

This section describes the first step of the sensitivity check. First a protrusion was fixed to the HV conductor in the test-vessel. At a voltage level of 64 kV we measured a PD level of 5 pC according to the IEC 60270 recommendations and the frequency spectrum shown in figure 4.12a. Then the pulse generator is connected to coupler 1. The frequency spectrum is measured again at coupler 2. Injection of artificial pulses of 1.45 V resulted in a similar spectrum as of a protrusion of 5 pC, see figure 4.12b.

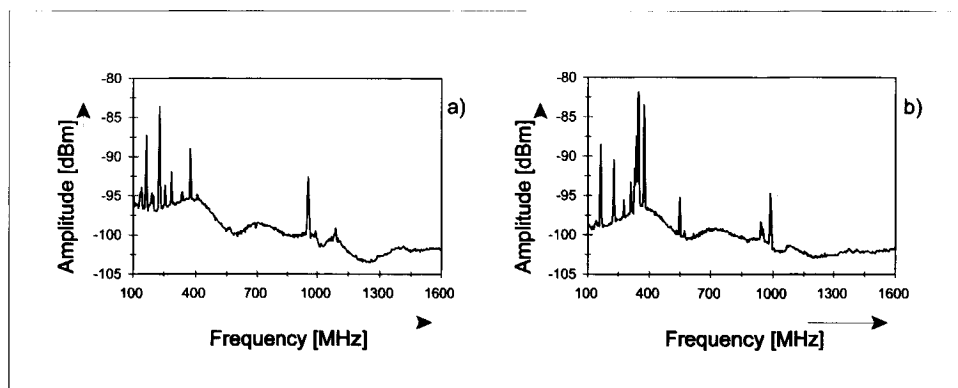


Figure 4.12: Frequency spectra measured at coupler 2 resulting from
a) a protrusion fixed to the HV conductor with a PD magnitude of 5 pC.
b) artificial impulses of 1.45 V injected at coupler 1 to simulate a protrusion on the HV conductor of 5 pC.

The same procedure was repeated for a free moving particle. The frequency spectrum measured at coupler 2 is shown in figure 4.13a. In this case the PD magnitude was 5 pC at a voltage level of 160 kV. Injection of artificial pulses of 10 V on coupler 1 results in the a frequency spectrum at coupler 2, see figure 4.13b.

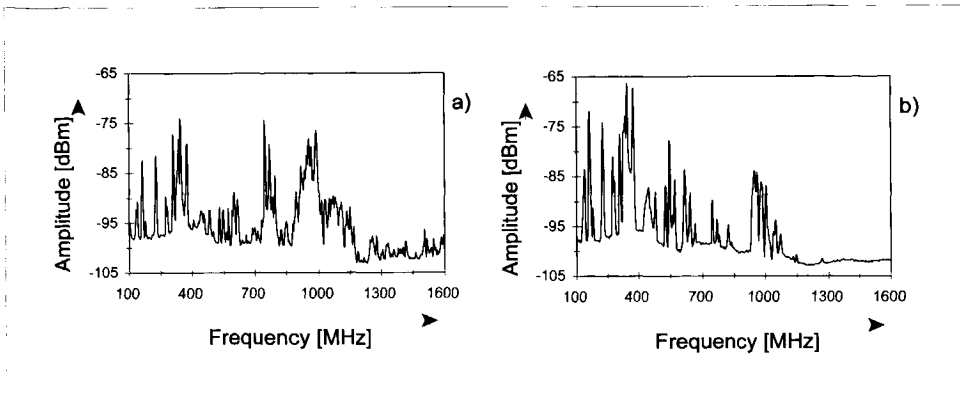


Figure 4.13: Frequency spectra measured at coupler 2 resulting from
a) a free moving particle with a PD magnitude of 5 pC.
b) artificial impulses of 10 V injected at coupler 1 to simulate a free moving particle of 5 pC.

4.6.2.2 STEP 2: ON-SITE TESTS

At the beginning of this chapter, we determined the coupler locations to reach a sensitivity of 5 pC for free particles and fixed protrusions in the test setup in Delft. Here we check the sensitivity to verify the determined locations. For this purpose, we carry out the following measurements:

- 1) To check the sensitivity of the proposed coupler locations for free moving particles, we inject 10 V pulses in coupler 1 (which is location L1, shown in figure 3.10). If these pulses can be detected at coupler 2 (location L9), the sensitivity check for free moving particles is successful;
- 2) To check the sensitivity of the proposed coupler locations for a fixed protrusion, we inject 1.45 V pulses in coupler 1 (which is location L3, shown in figure 3.10). If these pulses can be detected at coupler 2 (location L9), the sensitivity check for protrusions is successful.

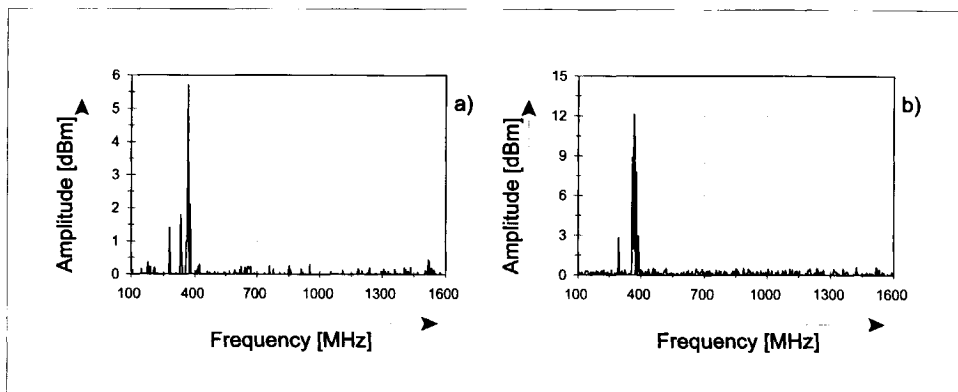


Figure 4.14: Frequency spectra measured resulting from

- a) artificial impulses of 10 V injected at coupler 2 and detected at coupler 1 to verify the sensitivity between these couplers for free moving particles which generate PD pulses with a 5 pC magnitude.
- b) artificial impulses of 1.45 V injected at coupler 2 and detected at coupler 1 to verify the sensitivity between both couplers for fixed protrusions which generate PD pulses with a magnitude of 5 pC.

The sensitivity check to free particles is shown in figure 4.14a. Although only a small signal is left, it is still detectable. So we can conclude that there is enough sensitivity between both couplers to detect free particles generating PD pulses of a magnitude of 5 pC.

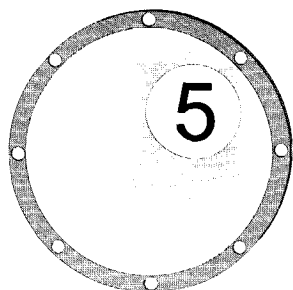
The sensitivity check to protrusions is shown in figure 4.14b. Again, a small signal is still detectable. As a result, fixed protrusions generating PD pulses of 5 pC magnitude between both couplers will be detected.

From this sensitivity check we can conclude that, using the estimated coupler locations, the UHF measuring circuit has enough sensitivity to detect either protrusions or free particles with a PD magnitude down to 5 pC at least.

4.7 CONCLUSIONS

In this chapter we have analysed the influence of GIS components on the propagation of electromagnetic waves through the GIS. The following conclusions can be drawn:

- a) The ratio of the UHF signal processed from the frequency spectrum measured at the UHF coupler before the GIS component under investigation and measured behind this GIS component is approximately constant;
 - b) This ratio not only depends on the GIS component under investigation, but is also determined by the complete configuration which is used for the investigation;
 - c) Each GIS component can be represented by reflection and transmission coefficients;
 - d) Based on calculations it is possible to estimate the UHF coupler locations to ensure a 5 pC detection sensitivity to protrusions and free moving particles, which can be verified with a sensitivity check.
 - e) The UHF signal is a better measure for the PD current than the apparent charge.
-



CHAPTER 5

EXPERIMENTAL RESULTS

At the moment, most gas-insulated lines and long busbars in GIS are filled with pure SF_6 . During the last 5 years a new generation of GIL has been developed, in which SF_6 - N_2 gas mixtures are used for insulation properties instead of pure SF_6 . Recently the first new type of GIL has been installed in Geneva, Switzerland [54]. So the question arises if the pure SF_6 gas can readily be exchanged by SF_6 - N_2 gas mixtures. Therefore, we investigated the PD processes originating from the same defects under the same conditions (similar operating voltage level and configuration) in pure SF_6 and SF_6 - N_2 gas mixtures with similar dielectric strength.

5.1 PD DETECTION SYSTEM ACCORDING TO IEC 60270

Besides the UHF measuring system to detect partial discharges (PD's) in GIS, we also used a standard PD measuring system based on the IEC 60270 recommendations [12]. This standard PD detection circuit is composed of a coupling capacitor, a coupling device and a PD detector, see figure 5.1. It is based on the charge displacement in the terminals to the GIS [25]. The coupling capacitor makes the required closed circuit for the charge displacement. It should be of the same order of magnitude as the capacitance of the GIS (about 40 pF/m in the case of our test setup). The coupling device converts the input current (discharge displacement in the leads) into voltage pulses. These voltage pulses are registered by a PD detector and can be further analysed.

In the standard measuring system, the partial discharge magnitude is the most important quantity. Therefore, a calibration procedure is required to measure the PD magnitude with acceptable accuracy. Calibration of the measuring system, with the test object in the test circuit, is carried out by injecting short-duration current pulses of known charge magnitude in the terminals of the test object. The calibration must be performed for the range of the expected PD magnitudes. In this way, the relation between the reading of the PD detector and the injected charge is known. More details on the calibration procedure can be found in [12].

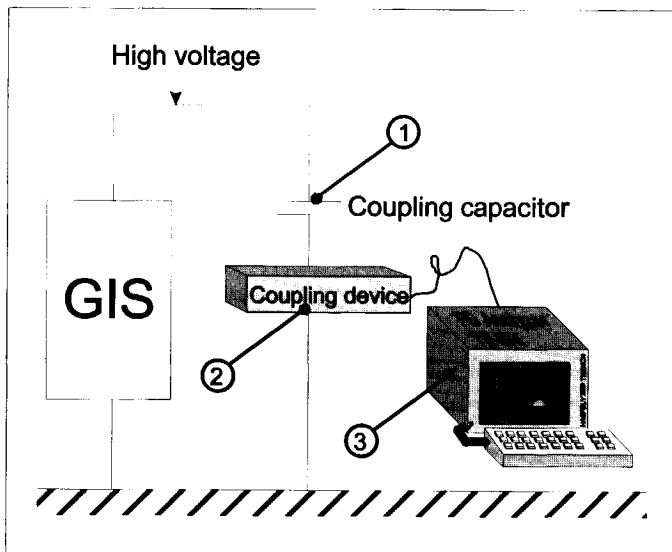


Figure 5.1: IEC 60270 measuring circuit as has been used for partial discharge measurements [25]:

- 1) Coupling capacitor which provides a closed circuit for the discharge displacement;
- 2) Coupling interface which contains a measuring impedance and pulse-shaping;
- 3) PD detector.

5.2 PROTRUSION FIXED TO THE HIGH-VOLTAGE CONDUCTOR

In this section, PD phenomena from a 15 mm protrusion fixed to the high-voltage conductor, as shown in figure 2.4, in pure SF_6 and SF_6 - N_2 mixtures are investigated. In particular, corresponding gases are analysed: 4.5 bar pure SF_6 , 11.5 bar 5% SF_6 - N_2 mixture and 9.5 bar 10% SF_6 - N_2 mixture.

5.2.1 PD INCEPTION AND BREAKDOWN VOLTAGE

The partial discharge inception voltage (PDIV) U_i is the lowest voltage at which repetitive partial discharges are observed in the test arrangement when the voltage is gradually increased from a lower value at which no PD's are observed [12]. The PD inception voltage levels for pure SF_6 , a 5% SF_6 - N_2 mixture and a 10% SF_6 - N_2 mixture have been measured, figure 5.2a. Figure 5.2b shows a comparison of the PDIV and the AC breakdown voltage (BDV) of a fixed protrusion in gases with similar dielectric strength

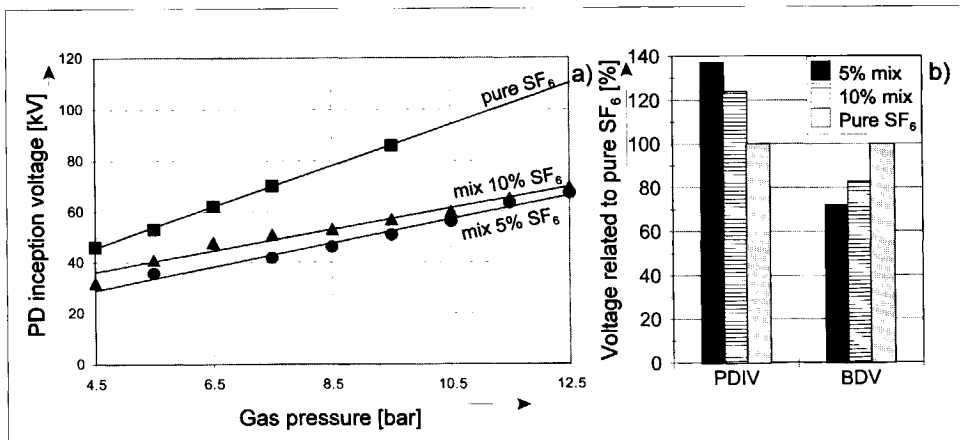


Figure 5.2:

- a) PD inception voltage for a protrusion fixed to the HV conductor as function of the gas pressure for different gases:
- PDIV pure SF_6 ;
 - ▲ PDIV 10% SF_6 - 90% N_2 mixture;
 - PDIV 5% SF_6 - 95% N_2 mixture.
- b) Comparison of PD inception voltage (PDIV) and breakdown voltage (BDV) for gases with different percentages of SF_6 but with similar dielectric properties, related to the BDV of 4.5 bar pure SF_6 .

(lightning impulse). It can be concluded that although the inception voltage is higher in the mixtures in the presence of a protrusion, the breakdown voltage is lower as compared to 4.5 bar pure SF_6 . This will be explained in more detail in the next section.

From figure 5.2 the following can be concluded:

- The PDIV increases linearly with the pressure [52];
- The PDIV increases with the amount of SF_6 in the gas mixtures;
- For gases with corresponding dielectric strength, the PDIV is the highest in the 11.5 bar 5% SF_6 - 95% N_2 gas mixture, followed by the 9.5 bar 10% SF_6 - 90% N_2 gas mixture and the 4.5 bar pure SF_6 [53].

5.2.2 PHASE-RESOLVED PD PATTERNS

Depending on the protrusion geometry, gas and electric field, different characteristic types of PD patterns can be measured, see figure 5.3. At the inception voltage, discharges will occur around the negative half of the sine wave of the applied voltage as shown in figure 5.3a. If the applied voltage is larger than the PDIV, streamer activity will occur in both halves of the sine wave, see figure 5.3b. Moreover, if the applied voltage is close to the breakdown voltage, also leaders occur in case of pure SF_6 and breakdown follows, figure 5.3c [24, 55].

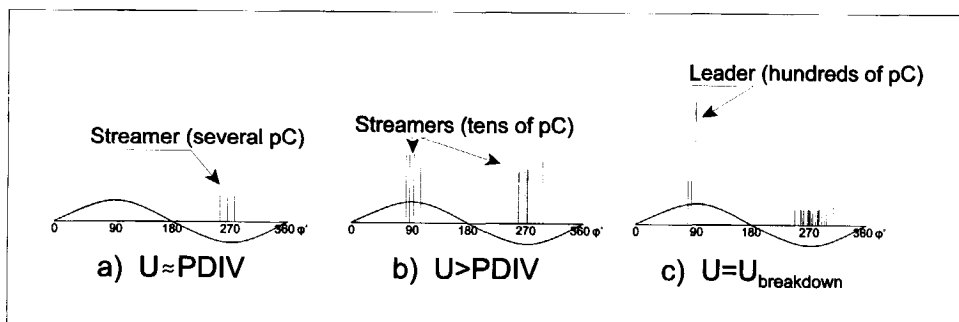


Figure 5.3: Different PD processes for fixed protrusions from inception to breakdown:

- a) at the PD inception voltage;
- b) above the PDIV;
- c) at the breakdown voltage.

Figure 5.4 shows examples of the PD patterns obtained at the same voltage level in the three types of investigated gases. For all three patterns can be concluded that already streamer activity is present. Moreover, in the mixtures, the PD levels are much higher than in pure SF_6 . Using a standard measuring circuit, the discharges in the negative half of the sine wave in case of the gas mixtures were below the measuring threshold and could not be measured.

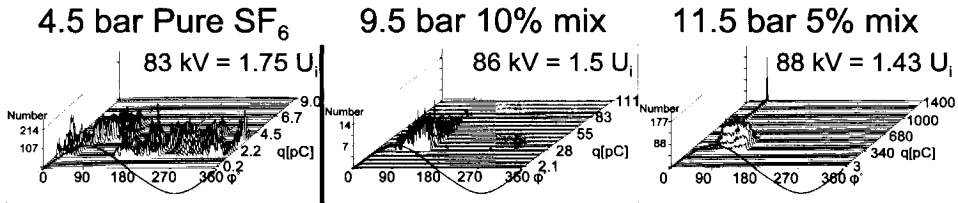


Figure 5.4: Phase-resolved PD patterns of a HV protrusion measured in the three corresponding pressurised gases at similar voltage levels.

As was already shown in figure 5.2, the PDIV U_i of the same defect is the lowest for pure SF_6 and the greatest in the 5% SF_6 - 95% N_2 gas mixture. So although the PD inception voltage is higher in mixtures, the PD process is closer to breakdown which has been confirmed by breakdown tests, see figure 5.2b.

In case of similar configurations and at the same operating voltage it can be concluded that:

- 1) the same defect in a gas mixture (at corresponding dielectric strength as pure SF_6) is closer to breakdown than if it is in pure SF_6 ;
- 2) the criticality of such defect increases with decreasing SF_6 content.

This results in:

- 1) a better detectability of discharging protrusions in SF_6 - N_2 ;
- 2) higher priority for better quality control in case of SF_6 - N_2 gas insulated equipment.

5.2.3 PD MAGNITUDE

A comparison of the PD magnitude originating from the protrusion fixed to the HV conductor in the three different gases is shown in figure 5.5. In this case we applied a test voltage of 20% above the inception voltage. The following can be observed:

- 1) At lower gas pressures (up to 8.5 bar), the magnitude of the discharges in the negative half of the sine wave (PD^-) increases linearly with the gas pressure and are larger than the discharges in the positive half of the sine-wave (PD^+);
- 2) Around 8.5 bar, the slope of the linear fit suddenly increases: the discharges in the positive half of the sine wave (PD^+) grow more rapid than the discharges in the negative half of the sine wave (PD^-);
- 3) At higher gas pressures (8.5 bar and above) the PD magnitude also increases linearly with the gas pressure;
- 4) The PD magnitude decreases with a higher SF_6 content in the gas.

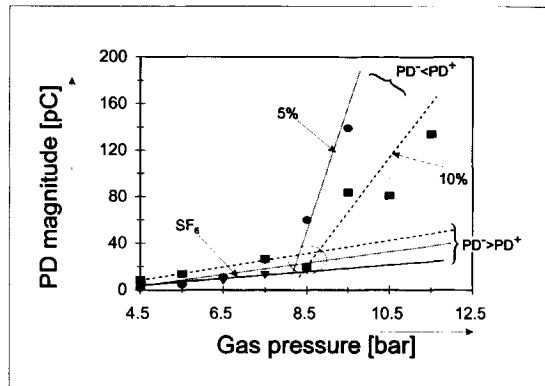


Figure 5.5: *PD magnitude of a HV protrusion at 1.2 times the inception voltage as function of the gas pressure for*

- ▼ Pure SF_6
- 10% SF_6-N_2 mixture
- 5% SF_6-N_2 mixture

The increase in the PD magnitude at a gas pressure of 8.5 bar can be explained by the active PD process:

- 1) at lower gas pressures, only discharges in the negative half of the sine wave has been observed;
- 2) at higher gas pressures, also discharges in the positive half of the sine wave has been observed.

5.2.4 UHF FREQUENCY SPECTRA

We also applied the UHF measuring circuit to detect PD activity. Figure 5.6 shows examples of the measured frequency spectra.

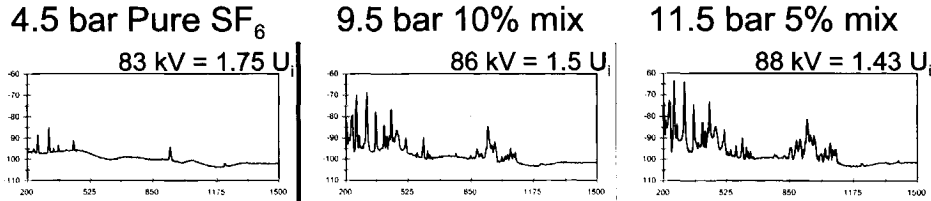


Figure 5.6: Frequency spectra measured for a HV protrusion in the three corresponding pressurised gases at similar voltage levels, averaged from 20 sweeps of 5 seconds.

Similar to the measuring results obtained with a standard measuring circuit as shown in the PD patterns of figure 5.4, also the frequency spectra change, see figure 5.6. In particular the number of peaks and the magnitude of the peaks in the spectra change. To compare the PD magnitude and the frequency spectra, the key value AR has been processed and plotted against the PD magnitude measured in pC, see figure 5.7. Although the results show scatter, it is possible to define a linear relation between the PD magnitude and the key value AR processed from the UHF frequency spectra.

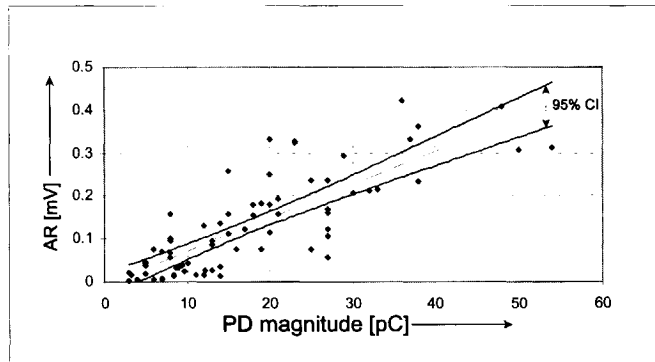


Figure 5.7: The relation between the PD magnitude measured in pC and the key value AR processed from the corresponding frequency spectra for a protrusion fixed to the HV conductor obtained at different voltage levels and in different gas mixtures. The 95% confidence intervals are also indicated.

5.2.5 UHF PHASE-RESOLVED PD PATTERNS

As described in section 3.1 a spectrum analyser can also measure phase-resolved patterns (POW's), which are comparable to the PD patterns measured with a standard measuring circuit. To obtain the PD patterns shown in figure 5.8 we tuned the spectrum analyser at a centre frequency of 748 MHz using a resolution bandwidth of 3 MHz. It is important to notice that the PD magnitude is given in μV and not in pC ; it is still not possible to calibrate the narrowband UHF method [51].

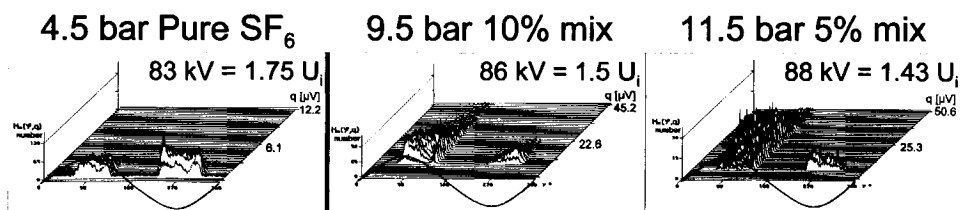


Figure 5.8: Phase-resolved PD patterns measured for a HV protrusion in the three corresponding pressurised gases at similar voltage levels using the UHF measuring technique tuned at a centre frequency of 748 MHz.

The patterns look rather similar to the patterns measured with a standard measuring circuit of figure 5.4. However, a clear advantage of the UHF measuring circuit can be seen in pattern measured in 4.5 bar pure SF_6 : the pattern is less influenced by noise. A second advantage can be observed in the PD patterns obtained in the gas mixtures: besides the discharges in the positive half (which was also measurable with the standard circuit), also the smaller discharges in the negative half can be measured. This confirms the better sensitivity of the UHF measuring system compared to a standard measuring circuit.

5.3 PROTRUSION FIXED TO THE ENCLOSURE

In this section, PD phenomena from a 30 mm protrusion fixed to the enclosure, as shown in figure 2.5, are investigated.

5.3.1 PD INCEPTION AND BREAKDOWN VOLTAGE

The PD inception voltage of a protrusion fixed to the enclosure is determined in a similar way as with the HV protrusion. In contrast to the HV protrusion, the PD pulses at the PD inception voltage will now occur in the positive half of the sine wave [24]. In figure 5.9a the PD inception voltage levels for pure SF_6 , 5% SF_6 - N_2 mixture and 10% SF_6 - N_2 mixture are shown. Figure 5.9b shows a comparison of the PDIV and the BDV of a fixed protrusion in gases with similar dielectric strength. For the same reasons as in the case of a protrusion fixed to the high-voltage conductor it can be concluded that although the inception voltage is higher in the mixtures in the presence of a protrusion, the breakdown voltage is lower.

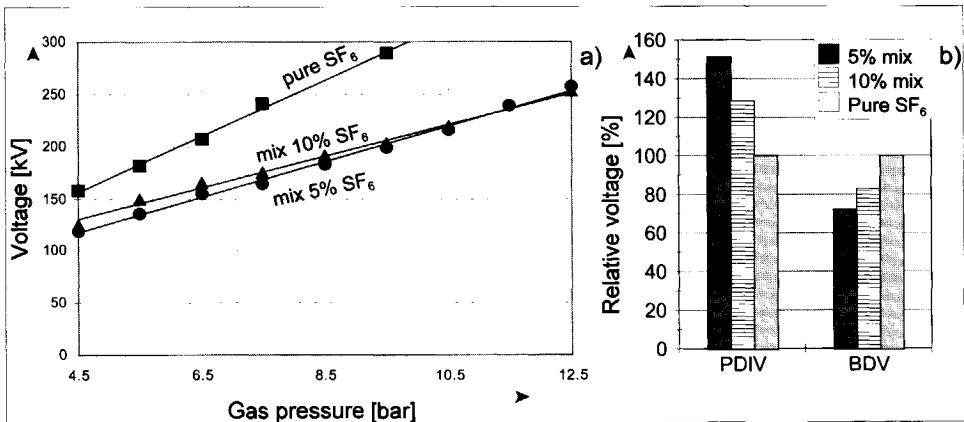


Figure 5.9:

- a) PD inception voltage for a protrusion fixed to the enclosure as function of the gas pressure for different gases:
- PDIV pure SF_6 ;
 - ▲ PDIV 10% SF_6 - 90% N_2 mixture;
 - PDIV 5% SF_6 - 95% N_2 mixture.
- b) Comparison of PD inception voltage (PDIV) and breakdown voltage (BDV) for gases with different percentages of SF_6 but with similar dielectric properties, standardized to pure SF_6 .

From figure 5.9 the following can be concluded:

- The PDIV increases linearly with the gas pressure;
- There is a small difference in the PD inception voltage measured in a 5% and a 10% SF_6 - N_2 gas mixture at the same gas pressure;
- Comparing figures 5.2 and 5.9 shows that the PD inception voltage for a LV protrusion is three times higher than that for the protrusion fixed to the HV conductor; this can be explained by the lower field intensity at the enclosure;
- For gases with corresponding dielectric strength, the PDIV is the highest in the 11.5 bar 5% SF_6 - 95% N_2 gas mixture, followed by the 9.5 bar 10% SF_6 - 90% N_2 gas mixture and the 4.5 bar pure SF_6 .

5.3.2 PHASE-RESOLVED PD PATTERNS

Examples of PD patterns in the three corresponding gas types are compared at the same test voltage, to investigate the influence of the gas on the same defect, see figure 5.10.

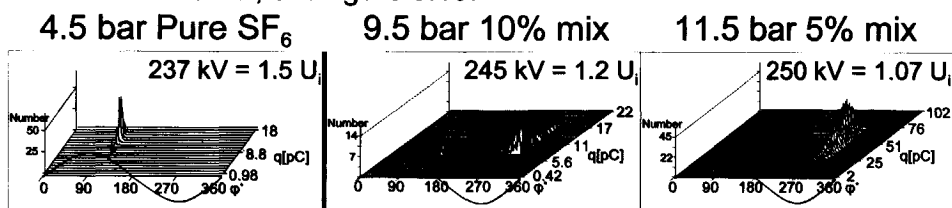


Figure 5.10: Phase-resolved PD patterns measured for a LV protrusion in the three corresponding pressurised gases at similar voltage levels.

Significant differences in the PD patterns measured in the three gases can be seen in figure 5.10. In case of a LV protrusion, the discharging process will start in the positive half of the sine wave of the applied test voltage. From the PD patterns shown in figure 5.10 we can therefore conclude that even at 50% above the inception voltage, no discharge activity during the negative half of the sine wave occurs. In contrast, the PD patterns obtained in the gas mixtures show already discharge activity in the negative half at the same applied test voltage, which was in this case 7-20% above the inception voltage. Similar to the protrusion fixed to the high-voltage conductor, the PD process in case of gas mixtures closer to a breakdown. This has been confirmed by breakdown tests, which have been summarized in figure 5.9b.

Like the protrusion fixed to the high-voltage conductor, it can be concluded that (in case of similar configurations and at the same operating voltage):

- 1) the same defect in a gas mixture (at corresponding dielectric strength as pure SF_6) is closer to breakdown than if it is in pure SF_6 ;
- 2) the criticality of such defect increases with decreasing SF_6 content.

Although the PD magnitude does not say anything about the criticality of a discharging defect, comparison of the PD magnitude for similar defects under the same conditions can be used to indicate differences in the risk. Therefore, we compared the PD magnitudes of protrusions in table 5.1. Because the PD magnitude increases with decreasing SF_6 content, it is confirmed that the criticality of the same defect also increases.

Table 5.1: Comparison of PD magnitude of fixed protrusions in pure SF_6 and gas mixtures.

	100% SF_6	10% SF_6	5% SF_6
HV protrusion	7 pC	80 pC	700 pC
LV protrusion	18 pC	20 pC	100 pC

5.3.3 PD MAGNITUDE

A comparison of the PD magnitude originating from the protrusion fixed to the LV conductor in the three different gases is shown in figure 5.11. In this case, we applied a test voltage of 20% above the inception voltage. From figure 5.11 the following can be observed:

- 1) At lower gas pressures (up to 9.5 bar), the PD magnitude of the discharges increases linearly with the gas pressure;

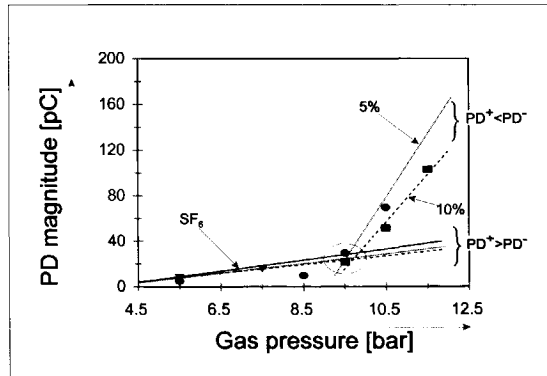


Figure 5.11: PD magnitude of a LV protrusion at 1.2 times the inception voltage as function of the gas pressure for

- ▼ Pure SF_6
- 10% $\text{SF}_6\text{-N}_2$ mixture
- 5% $\text{SF}_6\text{-N}_2$ mixture

- 2) Around 9.5 bar, the slope of the linear fit changes because the discharge also activity in the negative half of the sine wave increases;
- 3) At higher gas pressures (9.5 bar and above) the PD magnitude also increases linearly with the gas pressure;
- 4) The PD magnitude decreases with a higher SF_6 content in the gas.

5.3.4 UHF FREQUENCY SPECTRA

Again, we also applied the UHF measuring circuit to detect PD activity. Figure 5.12 shows examples of measured frequency spectra.

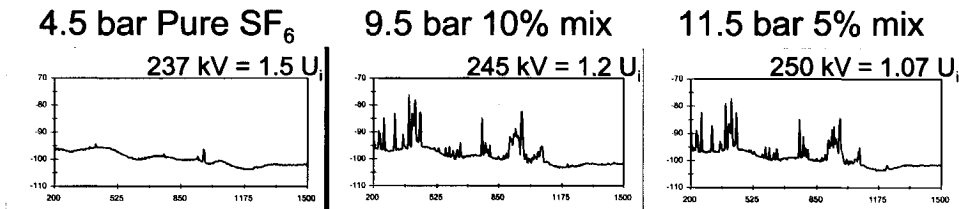


Figure 5.12: Frequency spectra measured for a LV protrusion in the three corresponding pressurised gases at similar voltage levels, averaged from 20 sweeps of 5 seconds.

Similar to the change in the PD magnitude obtained with a standard measuring circuit as shown in the PD patterns of figure 5.10, also the frequency spectra change, see figure 5.12; in particular the number of peaks and the magnitude of the peaks in the spectra.

5.3.5 UHF PHASE-RESOLVED PD PATTERNS

We used the spectrum analyser, tuned at a centre frequency of 955 MHz with a resolution bandwidth of 3 MHz, to measure phase-resolved PD patterns, see figure 5.13. Again, it is important to notice that the PD magnitude is given in μV and not in pC .

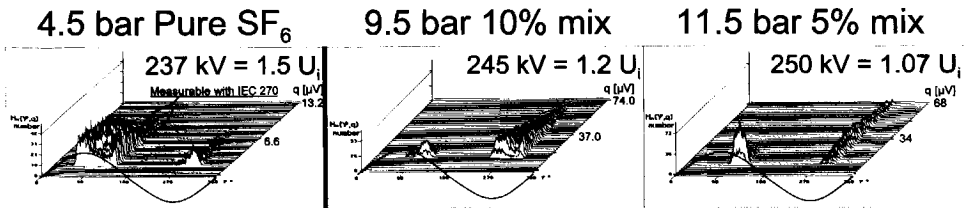


Figure 5.13: Phase-resolved PD patterns measured for a LV protrusion in the three corresponding pressurised gases at similar voltage levels using the UHF measuring technique tuned at a centre frequency of 955 MHz.

The patterns look rather similar to the patterns measured with a standard measuring circuit of figure 5.10. However, a clear difference of the patterns measured in 4.5 bar pure SF_6 can be seen: the pattern measured with a standard measuring circuit shows only the top part of the pattern, obtained with the UHF measuring circuit, as indicated in figure 5.13. Again this confirms the improved sensitivity of the UHF measuring system compared to a standard measuring circuit.

5.4 FREE MOVING PARTICLES

Measurements similar to those for the HV and LV protrusion have been carried out for the 15 mm long free particle shown in figure 2.6.

5.4.1 INCEPTION VOLTAGE

In the case of a free moving particle it is complicated to define the PD inception voltage. Visually we observed three different stages in the particle movement:

- 1) *shuffling particle*: the particle just starts to move really slowly and a very small contact-noise-like PD activity is measured as shown in the PD pattern in figure 5.19;
- 2) *moving particle*: the particle starts moving, accompanied with higher PD activity and the PD pattern changes, see figure 5.19;
- 3) *jumping particle*: the particle starts to jump and sometimes stays airborne for a few cycles.

In the following we refer to the voltage level of the first stage as the inception voltage.

We compare the voltage levels of the three gases at which the particle just starts to move (shuffling particle) in figure 5.14. These voltage levels show to be independent of the gas type and gas pressure, and, as explained in [32], the movement of a particle mainly depends on its geometry and the applied electric field.

The ignition voltage levels of the three different stages of movement are shown in figure 5.15 for a 5% SF_6 - N_2 gas mixture. Again, the gas pressure has no influence on the voltage levels. Similar results have also been obtained in pure SF_6 and in a 10% SF_6 - N_2 mixture.

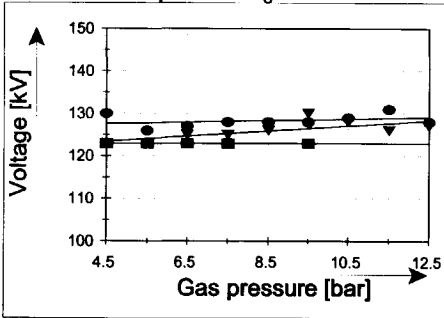


Figure 5.14: Voltage level at which a free particle just starts to move as function of the gas pressure in different gases:

- Pure SF_6
- ▼ 10% SF_6 - N_2 mixture
- 5% SF_6 - N_2 mixture

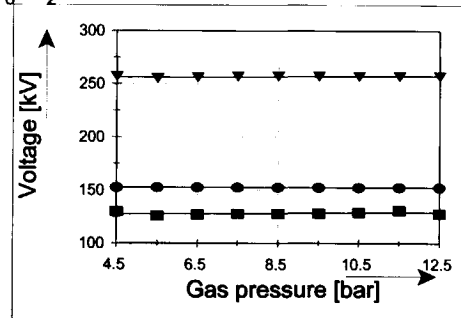


Figure 5.15: The three different voltage levels (or movement stages) at which a free particle:

- gives contact-noise-like PD
- starts to dance
- ▼ starts to jump

The results have been obtained in a 5% mixture.

5.4.2 PHASE-RESOLVED PD PATTERNS

In figure 5.16 examples of phase-resolved PD patterns measured with a standard measuring circuit are shown. In this case, we applied a test voltage of 1.6 times the inception voltage. Besides the influence of external disturbances, no differences in the PD patterns measured in the different gas types can be observed. Due to the noise level, it was not possible to measure the PD patterns right at the inception voltage (stage 1). This means that the PD magnitudes are smaller than the noise level of about 5 pC.

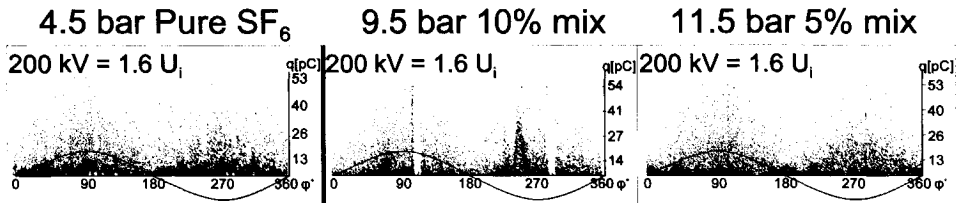


Figure 5.16: Phase-resolved PD patterns measured for a free particle in the three corresponding pressurised gases at similar voltage levels.

5.4.3 PD MAGNITUDE

A comparison of the PD magnitude of a free moving particle for the three investigated gases is shown in figure 5.17. A voltage level of 1.6 times the inception voltage was applied. The following can be seen in this figure:

- 1) A PD magnitude between 35-45 pC has been measured and is almost constant over the full 4.5-12.5 bar pressure range;
- 2) Like the lift-off voltage, the PD magnitude is independent of the type of gas.

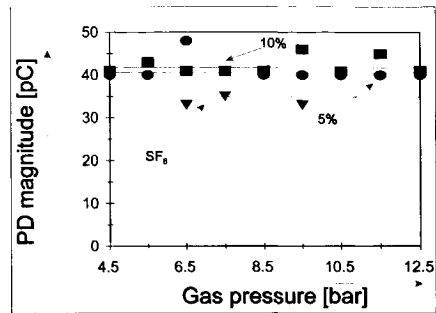


Figure 5.17: PD magnitude of a free particle at 1.6 times the inception voltage as function of the gas pressure for

- ▼ Pure SF_6
- 10% $\text{SF}_6\text{-N}_2$ mixture
- 5% $\text{SF}_6\text{-N}_2$ mixture

5.4.4 UHF FREQUENCY SPECTRA

Figure 5.18 shows examples of frequency spectra originating from a free particle measured at different voltage levels. Even at the ignition voltage of the first stage of particle movement, PD signals are clearly visible in the spectrum, while these were not detectable with the standard measuring circuit.

The shape of the frequency spectra shown in figure 5.18 can be separated into two types:

- 1) The spectra at the inception voltage of the first stage of particle movement;
- 2) The spectra at higher voltage levels.

This means that the three different stages which could be observed visually are not all visible in the frequency spectra.

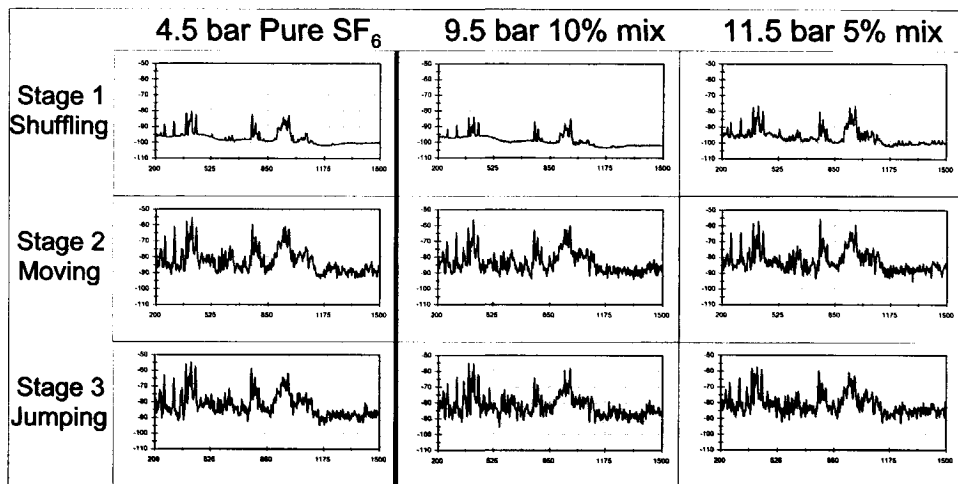


Figure 5.18: Frequency spectra measured for a free particle in the three corresponding pressurised gases at different voltage levels, processed from 20 sweeps of 5 seconds using averaging.

5.4.4 UHF PHASE-RESOLVED PD PATTERNS

To measure UHF phase-resolved PD patterns we tuned the spectrum analyser at a centre frequency of 748 MHz using a resolution bandwidth of 3 MHz. In contrast to the standard measuring circuit, we are able to measure partial discharges in stage 1 with the UHF method, where the particle is only shuffling, see figure 5.19.

As shown in the PD patterns in figure 5.19, the pulses are grouped around the zero-crossings of the applied test voltage. As known [24], such a pattern is typical for contact noise which can be expected from the particle behaviour in the first stage.

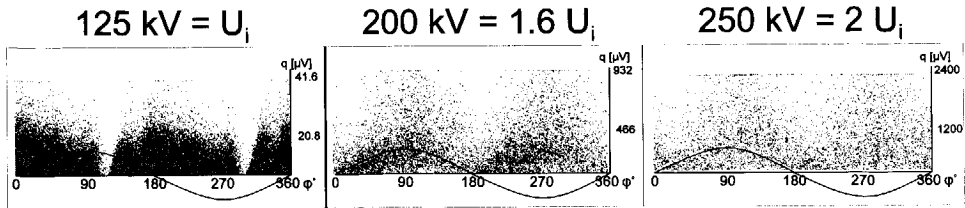


Figure 5.19: Phase-resolved PD patterns measured for a free particle in 10% mixture at the three different stages.

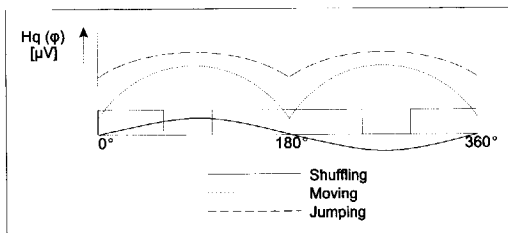


Figure 5.20: Typical phase-resolved PD patterns measured in each of the three stages in the particle movement.

Once the particle starts to move, it depends on the particle geometry and the applied test voltage as shown in [32, 56, 57]. The charge of the particle depends on the applied electric field, and therefore has a sinusoidal distribution as shown in figure 5.20. To go from the moving stage to the jumping stage, the applied voltage has to

increase and therefore the discharge magnitude also increases.

So analysis of PD patterns can be used to discriminate between stage 1 respectively stages 2 and 3 of the particle movement. To discern stage 2 from stage 3 further analysis is required and is described in chapter 7.

5.5 SUMMARY AND CONCLUSIONS

We have compared several PD-related phenomena of three types of PD sources: protrusions fixed to the high-voltage conductor or fixed to the enclosure, and free moving particles. These PD sources were investigated in pure SF_6 and in gas mixtures consisting of 5% SF_6 - 95% N_2 and 10% SF_6 - 90% N_2 . As shown in section 2.1, an SF_6 - N_2 gas mixture containing 5% SF_6 has to be pressurized at 11.5 bar and an SF_6 - N_2 gas mixture containing 10% SF_6 at 9.5 bar to have the same lightning impulse strength as 4.5 bar pure SF_6 . The above mentioned PD sources have been

compared in these three gas types at similar voltage levels to investigate their influence on the AC insulation strength.

In case of protrusions, the following can be concluded:

- 1) the PD inception voltage increases linearly with the gas pressure;
- 2) mixtures are more sensitive to protrusions than pure SF₆;
- 3) better quality control is required in case of SF₆-N₂ gas insulated equipment;

In case of free particles, the following can be concluded:

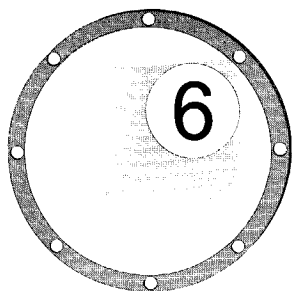
- 1) the gas has no influence on the PD inception voltage which is approximately constant;
- 2) three different stages in the movement of the particle has been observed: shuffling, moving, jumping;
- 3) the PD pattern measured from a shuffling particle differs from the moving and jumping particle, which are similar;
- 4) the frequency spectra measured for the three stages of movement are different in number of peaks and magnitude of the peaks;
- 5) the PD patterns and frequency spectra originating from free particles are highly similar in the three investigated gases;
- 6) no difference in the sensitivity for free particles has been observed in pure SF₆ and mixtures.

From the PD patterns analysed in this chapter it can be concluded that:

- there are no significant differences in PD patterns obtained using a standard measuring circuit and the UHF measuring circuit for all investigated defects;
- the type of gas (pure SF₆ or SF₆-N₂ gas mixtures) has no influence on the shape of the (typical) PD patterns measured for the three investigated gases.

This means that knowledge (phase-resolved PD patterns) gathered with both measuring circuits and in different gas-types is exchangeable. Moreover, the UHF measuring circuit:

- shows to be more sensitive due to better noise suppression;
 - gives additional information in the obtained frequency spectra which can improve the defect recognition.
-



CHAPTER 6

APPLICATION OF ON-SITE UHF PD INSPECTIONS

Since several years, UHF couplers are optional means for on-line PD detection in newly-build gas-insulated substations. However, many older existing substations are in service, without internal UHF couplers. To estimate the dielectric condition of such systems by measuring PD, external UHF couplers can be mounted in front of inspection windows, gas-rupture disks or spacers. Also, capacitive voltage sensors have effectively been used. In the following, the application of on-site and on-line PD diagnostics in a 380 kV GIS in the Netherlands will be illustrated.

6.1 ON-SITE GIS DIAGNOSTICS

To guarantee the required reliability of the 380 kV GIS in Meeden, several inspections are necessary:

- 1) Dewpoint measurements of the SF_6 gas in all compartments;
- 2) Gas pressure checks in all compartments;
- 3) Measurements of the amount of by-products of SF_6 ;
- 4) Checking the contact velocity of the circuit breakers;
- 5) Visual inspection of all connections of the installation;
- 6) Checks of the functioning of the secondary equipment;

These inspections are necessary to guarantee the required reliability of the substation.

In addition to this existing maintenance program, we proposed the on-line monitoring of the condition of the insulation material using the UHF PD measuring technique. A measuring procedure, which is described in Appendix D, has been applied to the 380 kV substation in Meeden, the

Netherlands. As an example, since December 12, 1996, we have performed UHF measurements on the coupler in the encircled area shown in figure 6.1. The signals at this coupler have been measured during ten inspection sessions over a time-period of four years. Figure 6.2 shows the key value average power processed from the obtained frequency spectra for all measuring dates.

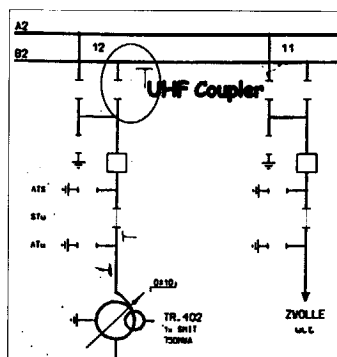


Figure 6.1: Part of the 380 kV substation. PD signals have been detected and monitored in the encircled area, during several measuring sessions over a time-period of four years.

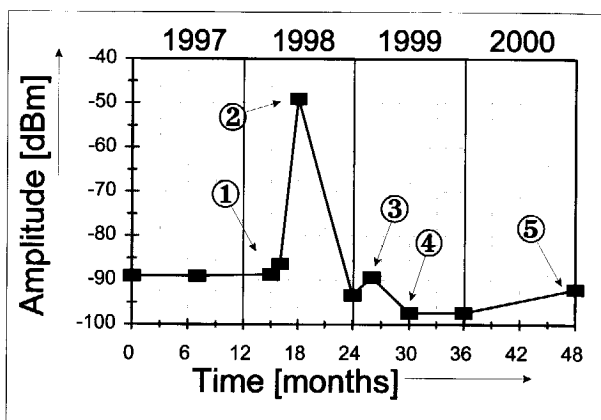


Figure 6.2: Trend analysis during a period of four years of key-value average power as has been calculated for the measurements obtained at one of the UHF couplers in the 380 kV GIS in Meeden, The Netherlands.

Point ①

Figure 6.3a shows the frequency spectrum measured on October 14, 1997. In this case there is no indication of any PD activity. Figure 6.3b shows the frequency spectrum measured on March 13, 1998. Some clear peaks can be observed causing the increase in the trend at point ①, as indicated in figure 6.2. The increase is probably introduced by a PD source, which has a PD pattern as shown next to the spectrum.

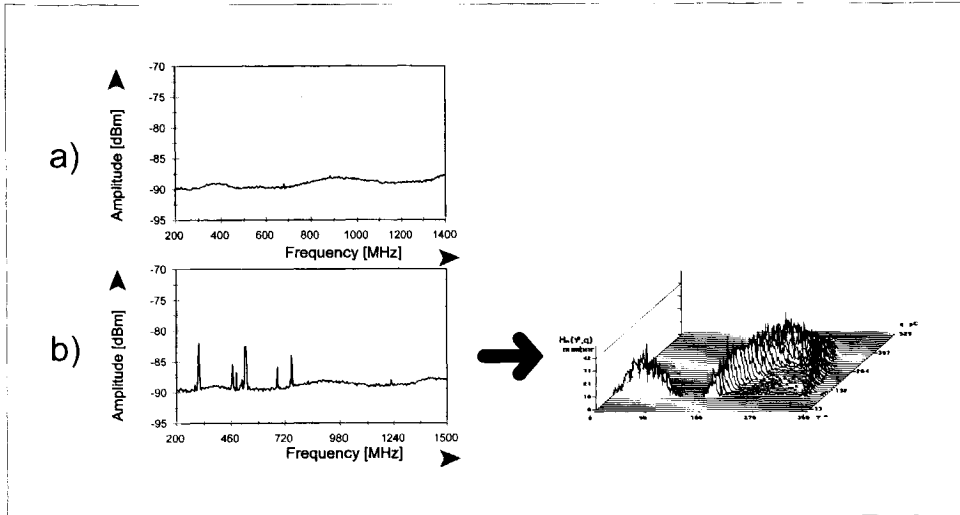


Figure 6.3 : *Frequency spectra and PD patterns measured:*

- a) *before 17-4-98;*
- b) *at 17-4-98.*

If we compare this PD pattern with the reference database, no similarities with any of the defects investigated in the laboratory can be concluded. Therefore, we compared the PD pattern with PD patterns shown in literature. We concluded that this type of PD pattern is probably originating from a void in a spacer [58, 59] and added this pattern to the reference database for comparison with future measurements.

Point ②

Figure 6.4a shows the frequency spectrum measured June 25, 1998. A huge increase in the amplitude compared to figure 6.3b can be observed. Also, the PD pattern is completely different.

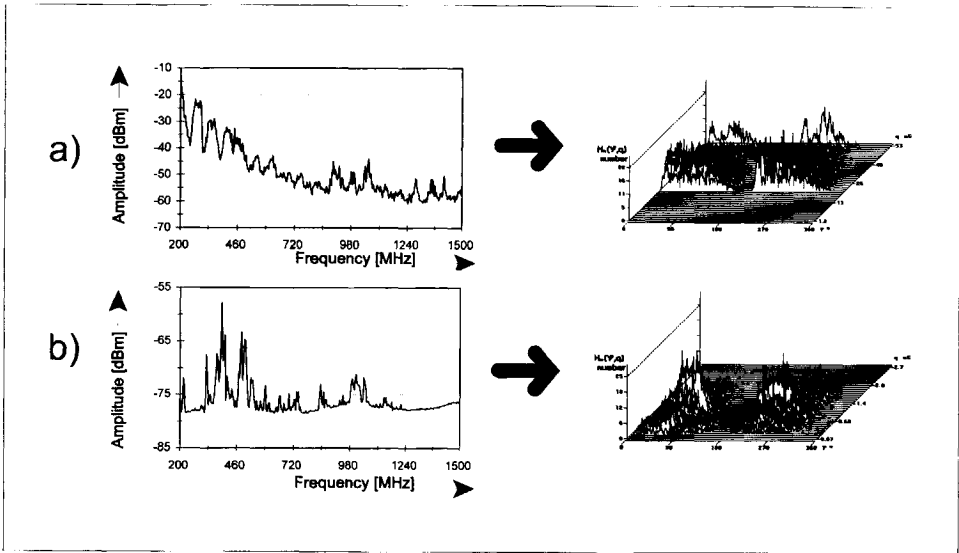


Figure 6.4: Frequency spectra and PD patterns measured:
a) at 15-6-98;
b) of a floating electrode modelled in the laboratory.

Again we compared the PD patterns with the reference database, see figure 6.5. In this case the measurement shows a large similarity with an electrically-floating electrode.

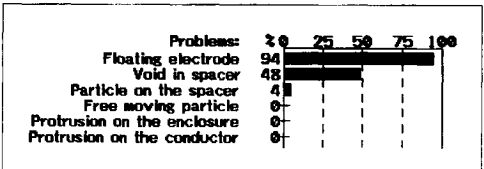


Figure 6.5: Outcome of the PD pattern recognition of the on-site measured PD pattern with the reference database obtained in a laboratory setup.

Figure 6.4b shows the frequency spectrum measured in a laboratory setup (consisting of similar equipment as the substation) from an electrically-floating part. Indeed, the similarities between the PD patterns measured in the substation and in the laboratory confirm the result from the analysis shown in figure 6.5.

Moreover, in the laboratory, a calibrated PD level of 400 pC was measured which means that the PD magnitude measured in the substation is probably larger than this value. This means that the signals are much

higher than the allowed 5 pC and it was decided to repair the defect. During the repair it was found that the PD signals were indeed coming from an electrically-floating screen; this screen and its connections have been replaced.

Point ③

During the tests after repair the spectrum shown in figure 6.7a was measured. In this case no peaks can be observed. Also no PD activity could be measured. Two months later, the frequency spectrum shown in figure 6.7b was measured. Again, some peaks can be observed and the PD pattern from a void in a spacer is measured again. This has been confirmed by statistical analysis, see figure 6.6.

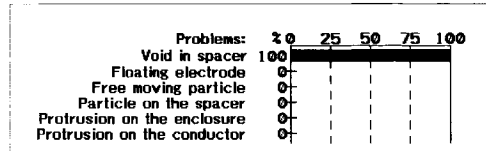


Figure 6.6: Outcome of the PD pattern recognition of the on-site measured PD pattern with the reference database obtained in a laboratory setup.

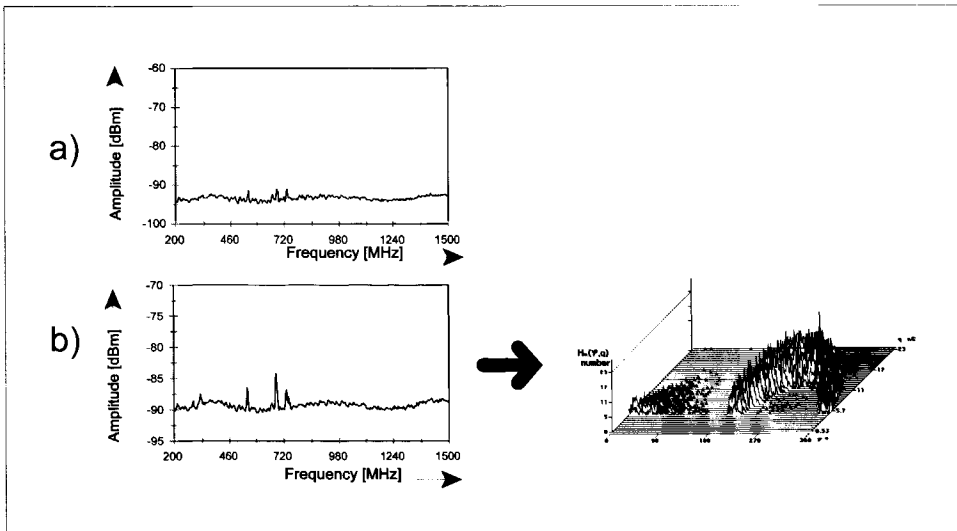


Figure 6.7: Frequency spectra and PD patterns measured:
a) during the tests after repair, at 5-12-98;
b) at 12-2-99.

As known for discharges in voids, statistical time lag delays inception of the discharges in the void [59]. This confirms the assumption that the measured PD activity is coming from a void in the spacer. Therefore, the periodic inspections at this particular coupler will continue, to monitor any future changes in the spectra.

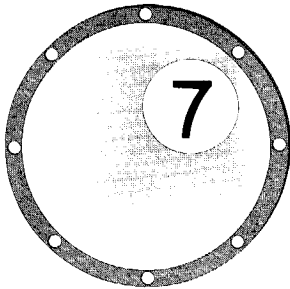
Points ④ and ⑤

The decrease in the trend at point ④ and increase in the trend at point ⑤ as shown in figure 6.2 can be explained by adjustments made to the amplifiers. Furthermore, we observed no changes in the frequency spectra and PD patterns.

6.2 CONCLUSIONS

Based on the investigations described in this thesis we defined a procedure for additional maintenance purposes of GIS. This procedure has been successfully applied in several substations in the Netherlands. In the 380 kV GIS in Meeden, The Netherlands, we revealed for instance the presence of an electrically floating electrode. We can conclude that:

- 1) Periodic inspections on GIS give valuable insight in the insulation condition, so that possible changes in its lifetime condition can be recognised;
 - 2) Calculation of frequency spectrum based key values is an effective means to indicate changes in the obtained spectra;
 - 3) The PD patterns and frequency spectra of an electrically-floating part which we measured on-site under operation conditions, show strong similarities with the PD patterns and frequency spectra measured from a modelled electrically-floating part in a laboratory setup.
-



CHAPTER 7 INSULATION CONDITION ASSESSMENT

According to the definition as given by the Society for Risk Analysis, risk analysis is *an analytical process to provide information regarding undesirable events* [60]. Risk assessment is the process of establishing information regarding acceptable levels of a risk of a defect to the insulation system [60]. In this thesis, critical defects are those defects which are at the threshold of being harmful to the dielectric integrity of the GIS under normal AC operating stresses [7]. For undesirable events in the insulation system of SF₆ gas-insulated systems an analysis process to assess the risk (called risk analysis process) involves the following four steps in condition assessment [61]:

- 1) detection (described in chapters 3 and 4);
- 2) identification (this chapter);
- 3) location (described in chapter 3) and
- 4) risk assessment of the defect (this chapter).

In this chapter a first approach of the risk analysis process is described. Except for the detection and location of the defect, which have been described in chapter 3 and 4, the topic of this chapter will be the identification and risk assessment of the detected defect.

7.1 PD IDENTIFICATION IN PURE SF_6 AND $\text{SF}_6\text{-N}_2$ MIXTURES

7.1.1 STATISTICAL ANALYSIS OF PD PATTERNS

Figure 7.1 shows typical phase-resolved PD patterns obtained for the three types of defects. It is clear that at similar voltage levels:

- the gas has no significant influence on the PD pattern of a free particle;
- the gas has a significant influence on the PD pattern of fixed protrusions.

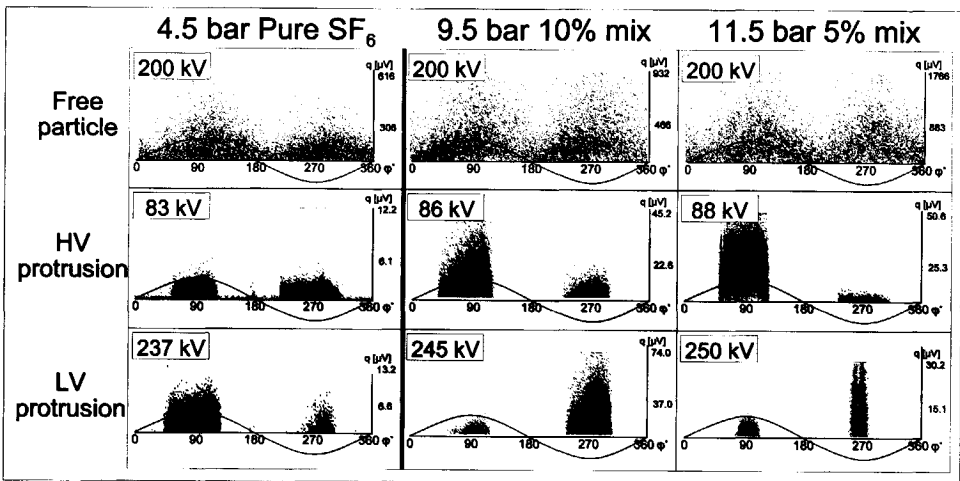


Figure 7.1: Typical PD patterns of a 10 mm free particle, a 15 mm protrusion fixed to the HV conductor (HV protrusion) and a 30 mm protrusion fixed to the enclosure (LV protrusion), obtained in 4.5 bar pure SF_6 and corresponding pressurised $\text{SF}_6\text{-N}_2$ mixtures.

The result of statistical analysis of PD patterns has been visualised in figure 7.2a. To clarify the result, we show only two of the 31 features which are processed from each phase-resolved PD pattern, as described in section 3.6. In the plot we can define two clusters. In one of these clusters, all measurements for a free moving particle collect together distinctively.

The measurements obtained from protrusions fixed to the high-voltage conductor (HV protrusion) as well as from those fixed to the enclosure (LV

protrusion) are mixed in the other cluster. So we conclude that this method is not capable of discriminating between both types of protrusions.

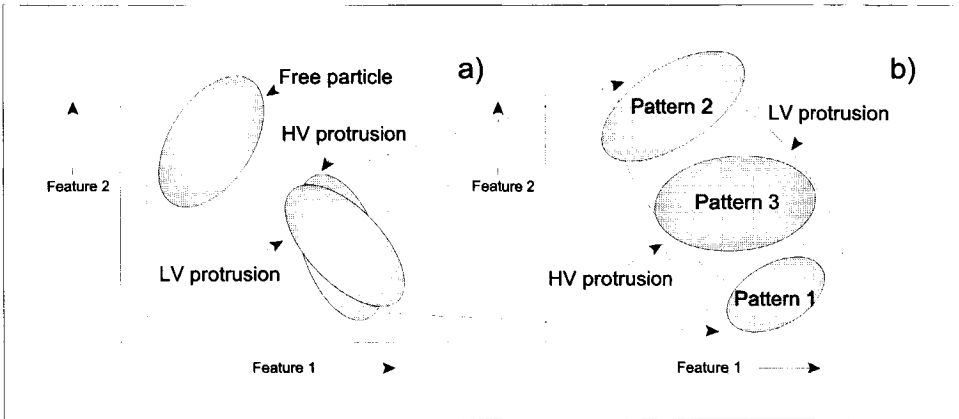


Figure 7.2: Cluster-formation after statistical analysis of phase-resolved PD patterns defined for

- a) different defects;
- b) different patterns in case of fixed protrusions.

Further analysis of the about two hundred PD patterns from fixed protrusions present in the reference database, resulted in three smaller clusters, as shown in figure 7.2b. In each of these smaller clusters, only measurements with one particular type of PD pattern were clustered. These three typical patterns are shown in figure 7.3. As explained in section 5.2.2, the type of pattern depends on the PD process:

- 1) Streamer discharges in negative half of the sine wave (inception);
- 2) Streamer discharges in both negative and positive half of the sine-wave (pattern type 2) or
- 3) mainly leader discharges (close to breakdown).

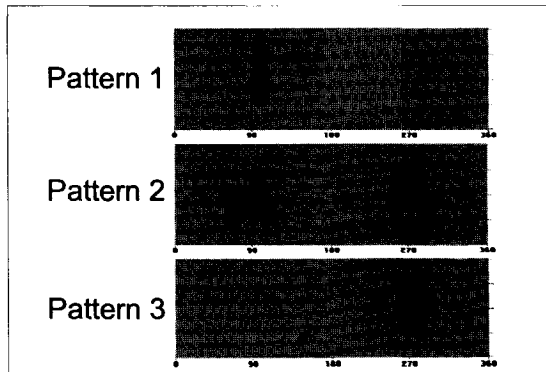


Figure 7.3: Different types of patterns measured for protrusions fixed to the high-voltage conductor or to the enclosure.

Table 7.1 shows the pattern types (as shown in figure 7.3) for each stage in the discharging process of fixed protrusions. So to state something of the risk of the protrusion we have to know the type of protrusion and the discharging process.

Table 7.1: *Different stages for protrusions fixed to the high-voltage conductor (HV-side) or fixed to the enclosure (LV-side), defined from inception (stage 1) to close to breakdown (stage 3). The PD patterns are shown in figure 7.3.*

Defect	Stage 1	Intermediate	Stage 3
HV-side	Pattern 3	Pattern 2	Pattern 1
LV-side	Pattern 1	Pattern 2	Pattern 3

As a result, we can conclude that only analysis of PD patterns is not sufficient for identification in case of protrusions. In section 7.1.2 we applied spectral analysis to improve the identification of defects.

7.1.2 STATISTICAL ANALYSIS OF FREQUENCY SPECTRA

In the previous section we applied statistical analysis to the phase-resolved PD patterns to discriminate between different defects. This was possible for free particles and fixed protrusions. However, in case of protrusions, depending on the different protrusion conditions, different PD patterns are generated. As a result, it was not possible to determine whether the protrusion was fixed to the high-voltage conductor or to the enclosure.

Therefore, we additionally applied statistical analysis to the frequency spectra as described in section 3.5. Frequency spectra obtained from the three investigated defects in the three gas-types are shown in figure 7.4.

We can conclude that:

- 1) As was the case for the phase-resolved patterns, the gas has no significance influence in case of the free particle; moreover, the spectra are also completely different from the fixed protrusions as was also the case with the PD patterns;

- 2) For the fixed protrusions, only a few peaks can be seen in the spectra in case of pure SF_6 , corresponding to the low discharge activity which has been observed in the phase-resolved patterns;
- 3) In the gas mixtures much more and higher peaks can be observed, resulting from the increased discharge activity.

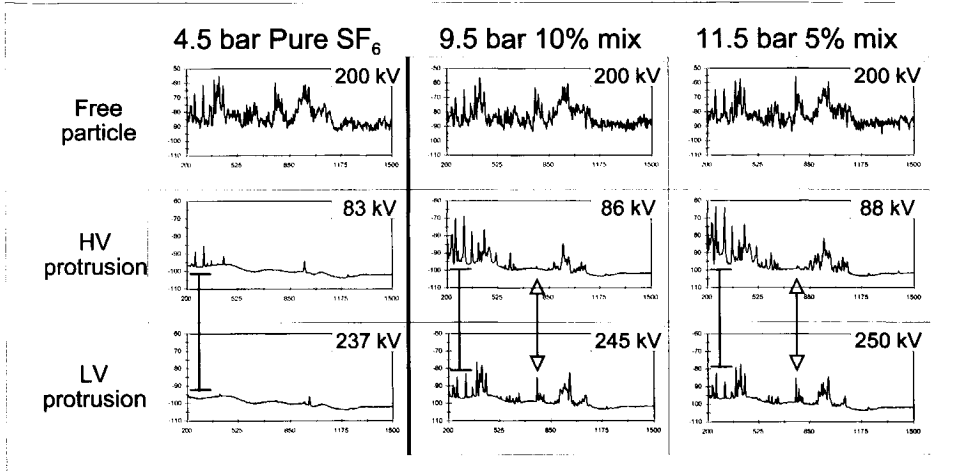


Figure 7.4: Typical frequency spectra of a 10 mm free particle, a 15 mm protrusion fixed to the HV conductor (HV protrusion) and a 30 mm protrusion fixed to the enclosure (LV protrusion), obtained in 4.5 bar pure SF_6 and corresponding pressurised $\text{SF}_6\text{-N}_2$ mixtures, processed from 20 sweeps of 5 seconds.

The main difference in the spectra of the fixed protrusions can be found in the amplitude of peaks in the low-frequency span between 100 and 350 MHz and the high-frequency span between 750 and 1100 MHz as indicated in figure 7.4.

A simplified explanation for this difference can be found in how the em-

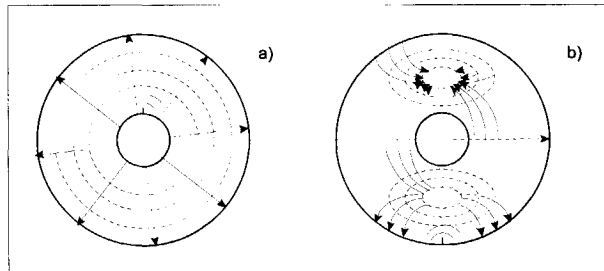


Figure 7.5: Excitation of electromagnetic waves in case of a protrusion fixed to:

- a) the high-voltage conductor: easy excitement of TEM modes: lower frequencies;
- b) the enclosure: easy excitement of higher order modes: higher frequencies.

waves are excited, see figure 7.5 [42]. This figure just shows two examples but in general this explains that TEM modes (low-frequency waves) are easier excited if the defect is located at the high-voltage conductor and higher order modes (high-frequency waves) if the defect is located at the enclosure.

The result of statistical analysis of frequency spectra has been visualised in figure 7.6. To clarify the result, we show only two of the thirteen features which are processed from each frequency spectrum. In the plot we can define three clusters. Each cluster contains measurements containing only one type of defect. So in contrast to the cluster analysis of PD patterns shown in figure 7.2, in the case of figure 7.6 there is no mix of measurements from different protrusions. So we can conclude that also the frequency spectra, measured from free or fixed defects in pure SF₆ or gas mixture, contain defect-specific information.

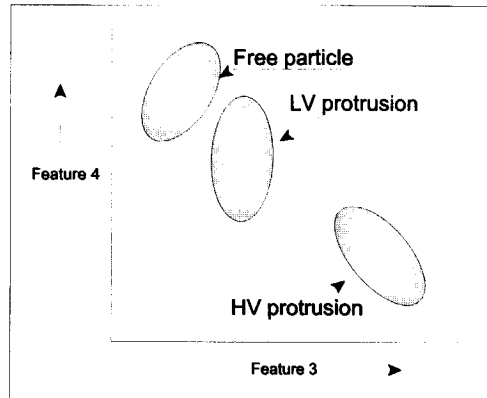


Figure 7.6: Cluster-formation after statistical analysis of frequency spectra for different defects.

7.1.3 CONCLUSIONS STATISTICAL PD IDENTIFICATION

From the previous sections can be concluded that:

- Both phase-resolved PD pattern analysis and frequency spectra analysis can be used to identify free particles;
- To discriminate between protrusions fixed to the high-voltage conductor and fixed to the enclosure only frequency spectra analysis has proven to be successful;
- To analyse the active PD process of fixed protrusions, phase-resolved PD pattern analysis has shown to be successful.

Table 7.2 shows a comparison of the polarity, amplitude and intensity of PD patterns and frequency spectra obtained for the three investigated defects in the three investigated corresponding pressurised gases.

Table 7.2: Comparison of PD patterns and frequency spectra originating from a free particle and fixed protrusions, in corresponding pressurised gases under the same test conditions.

	HV protrusion		LV protrusion		Free particle	
	PD pattern	Spectrum	PD pattern	Spectrum	PD pattern	Spectrum
4.5 bar pure SF ₆	Both polarities Low amplitude	Higher amplitude in low freq. span Low amplitude Low intensity	Both polarities Low amplitude	Higher amplitude in high freq. span Low amplitude Low intensity	Diffuse Low amplitude	High amplitude High intensity
9.5 bar 10% SF ₆ - 90% N ₂	Positive polarity High amplitude	Higher amplitude in low freq. span High amplitude High intensity	Negative polarity High amplitude	Higher amplitude in high freq. span High amplitude High intensity	Diffuse Low amplitude	High amplitude High intensity
11.5 bar 5% SF ₆ - 95% N ₂	Positive polarity Higher amplitude	Higher amplitude in low freq. span Higher amplitude Higher intensity	Negative polarity Higher amplitude	Higher amplitude in high freq. span Higher amplitude Higher intensity	Diffuse Low amplitude	High amplitude High intensity

7.2 CRITICALITY UNDER AC VOLTAGE CONDITIONS

In this section, the criticality of fixed protrusions and free particles for the AC insulation strength is analysed. In the following tables, overviews of the sensitivity of different detection methods to find critical defects are given by Feser [62, 63].

Table 7.3: *Detection of critical defects under AC conditions in GIS investigated in a laboratory setup using a PD measuring circuit according to IEC 60270 [62, 63].*

Defect	Critical length	PD magnitude	Detection in 420 kV GIS
Free particle	2-5 mm	5-25 pC	3 mm
Protrusion	1-2 mm	~ 1 pC	1 mm
Particle fixed on spacer	2-3 mm	~ 1 pC	3 mm
Floating electrode	-	> 100 pC	Yes
Void in spacer	-	-	Yes

From table 7.3 can be concluded that, in case of laboratory conditions, it is possible to detect critical defects in a 420 kV GIS, using a PD detection circuit according to the IEC 60270 recommendations. In practice, such conditions cannot be achieved in the field during on-line measurements. It can also be concluded that the PD magnitude does not give any information regarding the criticality of a defect. For example, a floating electrode produces PD activity of several hundreds of pC and is not immediately dangerous for the insulation condition, whereas a protrusion giving 1-2 pC discharge activity is very critical. Therefore, it is necessary to determine the discharging process, i.e. is the PD process at inception or close to a breakdown, using advanced PD diagnosis. This will be the topic of the next sections. The sensitivity for certain defects of the UHF measuring technique during on-line measurements on GIS has been investigated by Feser [62, 63] and is summarised in table 7.4.

Table 7.4: Comparison of the sensitivity of the UHF method during field measurements (on-site/on-line monitoring) on practical 420 kV GIS's with the critical defects determined in the laboratory [62, 63].

Defect	Critical length	UHF on-line detection in 420 kV GIS
Free particle	2-5 mm	5 mm
Protrusion*	1-2 mm	8 mm
Particle fixed on spacer*	2-3 mm	12 mm
Floating electrode	-	yes
Voids in solid material	-	yes

*These defects are removed during commissioning

Table 7.4 shows the sensitivity of on-line monitoring of a 420 kV GIS using the UHF technique. From the table can be concluded that it is possible to detect free particles, electrically floating electrodes and voids in solid material. It is not possible to detect critical particles fixed to conductors or spacers. However, such defects are removed during proper commissioning testing. In the following two examples of risk analysis of fixed and free particles are shown.

7.2.1 FIXED PROTRUSIONS

Lets analyse the risk of a fixed protrusion using for example the phase-resolved PD pattern from figure 7.7a. For this purpose we compared the measured PD pattern with the PD patterns stored in our reference database. Inside this database, different types of protrusions are stored, having several types of PD patterns. The outcome is shown in figure 7.7b and the defect is identified as a fixed protrusion: 90% similarity with the cluster of protrusions fixed to the enclosure and 76% similarity

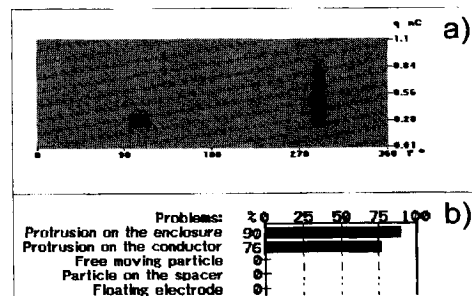


Figure 7.7: a) Phase-resolved PD pattern from a fixed protrusion and b) the statistical defect recognition based on phase-resolved PD pattern analysis.

with the cluster of protrusions fixed to the high-voltage conductor. This can be explained by the large overlap of the clusters of fixed protrusions as was already shown in figure 7.2a. Moreover, the 14% difference in the similarity is smaller than the standard deviation of each cluster and therefore nothing can be concluded about the position of this protrusion: fixed to the high-voltage conductor or enclosure.

Therefore, above-mentioned defects are further analysed by combined PD pattern analysis and spectral analysis, see figure 7.8. From the PD pattern analysis can be concluded that the pattern is originating from a fixed protrusion, giving partial discharge activity of pattern type 3. From spectral analysis we can conclude that the protrusion is fixed to the enclosure.

Comparing this with knowledge stored in an expert system, a high risk of this defect stage is concluded. In this way a criticality warning is attributed to the defect.

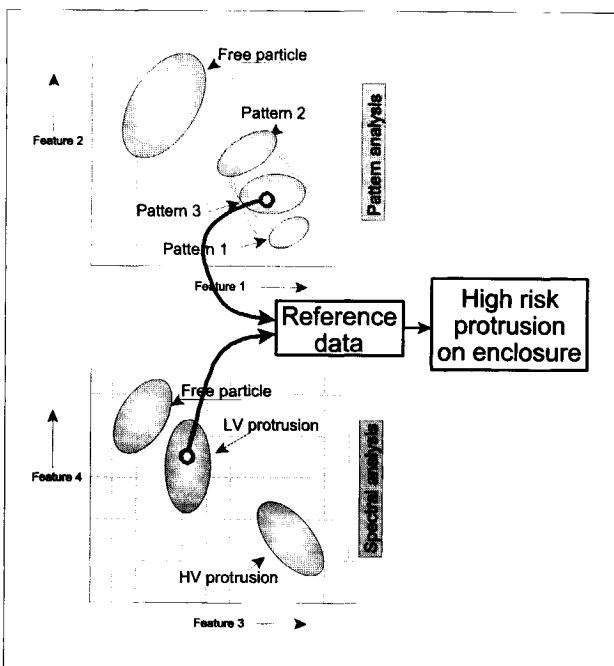


Figure 7.8: Risk assessment of a fixed protrusion.

7.2.2 FREE PARTICLES

Another defect in GIS that can be very dangerous for the dielectric strength, is the free moving particle. Especially when a particle approaches the high-voltage conductor, breakdown can occur [7]. As stated before, three stages have been observed in the behaviour of a free moving particle:

- 1) *shuffling particle;*
- 2) *moving particle;*
- 3) *jumping particle.*

It is clear that the third stage, the jumping particle, is the most critical one because it can reach the high-voltage conductor [7]. Risk assessment of free particles means that we can recognise jumping particles. From the PD patterns shown in figure 5.19 can be concluded that it is not possible to discriminate between moving and jumping particles based on the PD patterns.

Typical frequency spectra measured for each stage in the movement of a free particle is shown in figure 7.4. It shows processed frequency spectra using an averaging or max-hold technique over the 20 measured sweeps [65]. In all three situations it is clear that the hold-max frequency spectrum (gray line) is larger than the averaged frequency spectrum (black line). To

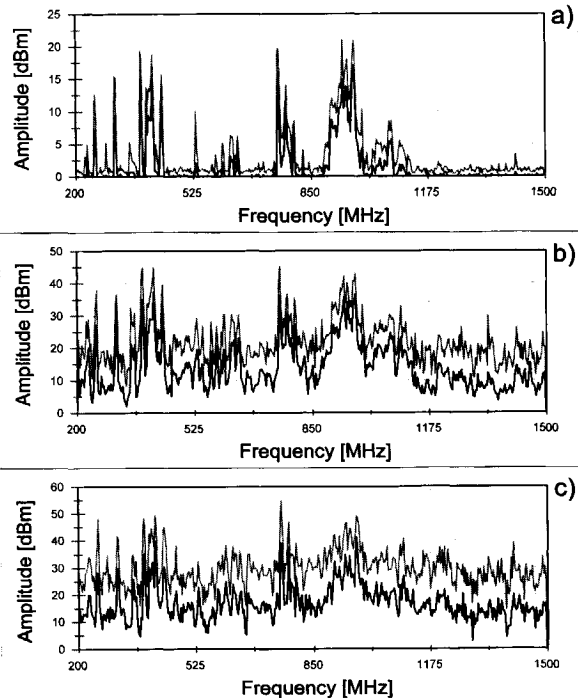


Figure 7.9: Max-hold (gray line) and averaged (black line) frequency spectra measured for a free particle when it is a) shuffling, b) moving and c) jumping.

compare the spectra, the key value AR has been calculated, see table 7.5.

Table 7.5: Key value AR calculated from the post-processed frequency spectra of a shuffling, moving and jumping particle, using an averaging or hold-max processing technique.

Defect	Averaged spectrum	Hold-max spectrum
Shuffling	0.18 mV	0.94 mV
Moving	6.3 mV	22.6 mV
Jumping	5.8 mV	28.8 mV

Table 7.5 confirms that the amplitudes in the max-hold frequency spectrum exceed the averaged amplitudes. However, once the particle starts jumping, the amplitude of the averaged spectrum decreases, whereas the amplitude of the max-hold spectrum increases. We will explain this by analysing three individual sweeps as shown in figure 7.10:

Stage 1: shuffling particle:

Compared to the dancing and jumping particle, the peaks in the frequency spectra of the shuffling particle have a very low amplitude and all measured sweeps are almost similar.

Stage 2 moving particle:

When the particle starts moving, but not jumping, the amplitude of the peaks in the frequency spectrum increases significantly and, again, all measured sweeps are almost similar.

Stage 3: jumping particle:

When the particle starts jumping, the frequency spectra are again different: the maximum amplitude of the peaks in the frequency spectra has increased again, but 'empty' parts are also observed in the spectra, which are indicated by arrows. These empty parts imply that no detectable PD activity occurs. This means that the particle does not hit the enclosure and is somewhere in the gap between the enclosure and conductor (this will be explained in more detail, using figure 7.11). This was confirmed by visual observation during the measuring period. If we post-process the spectrum

by averaging the measured sweeps, the result will be reduced due to these empty parts.

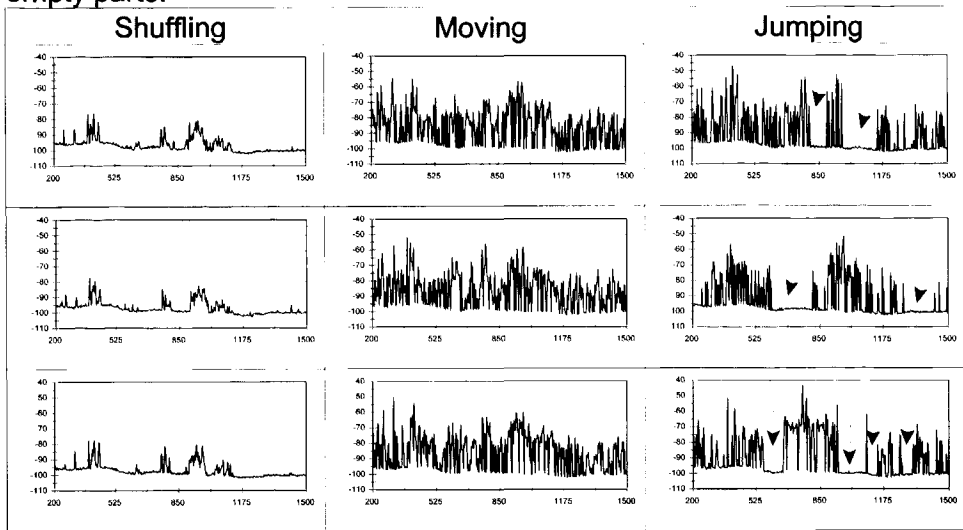


Figure 7.10: Three single frequency spectrum sweeps of 5 seconds, measured for each stage in the particle movement.

These empty parts can be explained by the way the spectrum analyser captures a frequency spectrum. A spectrum analyser effectively performs a Fourier analysis of a (continuous) input signal. Like a radio receiver it tunes at consecutive frequencies and captures the amplitude of the spectral content of the input signal at the tuned frequency. It takes a certain amount of time for the SA to tune at all frequencies in the frequency spectrum, called sweep time. As shown in figure 7.11, during the sweep time, the discharging signal at the input of the SA changes with each discharge. Therefore, the final captured frequency spectrum is build from several discharge signals. Moreover, if the particle is jumping, for example at t_3 as indicated in figure 7.11, there is no discharge activity and therefore no input signal. This results in the empty part of the frequency spectrum.

So the empty parts occurring in a frequency spectrum have nothing to do with no spectral content of the discharging signal. This can be seen in the Fourier spectra at times t_1 , t_2 and t_4 which obviously have no empty parts. Only due to the minimal amount of time required to capture a frequency spectrum, these empty parts appear as soon as the particle is jumping and, for some time, no discharge activity occurs. Because the particle

movement is a random process, the empty parts in the spectra can change from sweep to sweep, as shown in the three sweeps of jumping particles in figure 7.10.

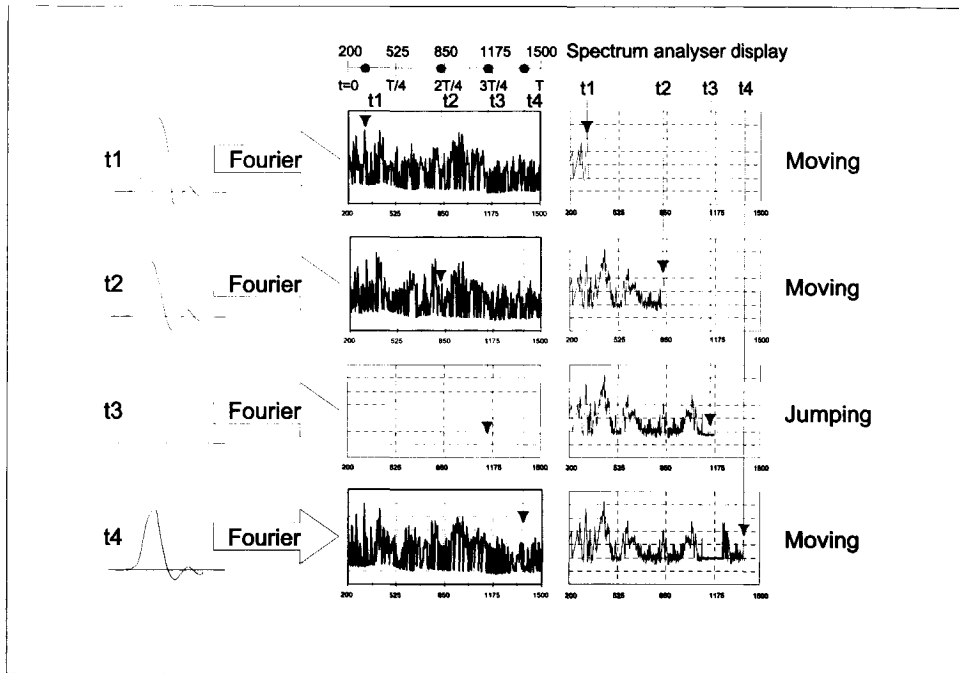


Figure 7.11: Capturing a frequency spectrum of a discharging defect using a spectrum analyser (SA).

In case of free particles, criticality risk assessment means that jumping particles and not-jumping particles can be distinguished. From table 7.5 can be concluded:

- If the particle is moving the ratio between both AR values is almost constant: $AR_{HM} \approx 3.6 \cdot AR_{AV}$;
- If the particle start jumping the ratio between both AR values is also constant, but is increased: $AR_{HM} \approx 5.0 \cdot AR_{AV}$.

Therefore we processed and analysed the ratios of about 80 measurements. As a result, we processed the probability density distributions for the found ratio between the AR of the hold max spectrum and of the averaged spectrum. The result is shown in figure 7.12. It is clear that the ratio of moving and jumping particles are differently distributed. As can be seen, the significance of the difference between both distributions is σ .

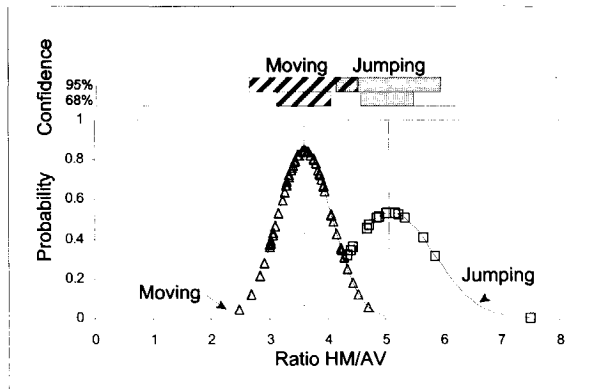


Figure 7.12: Probability density distribution for moving and jumping particles:

- △ Measured points moving particles;
- Measured points jumping particles.

Another way of displaying these results is by cumulative probability distributions shown in figure 7.13.

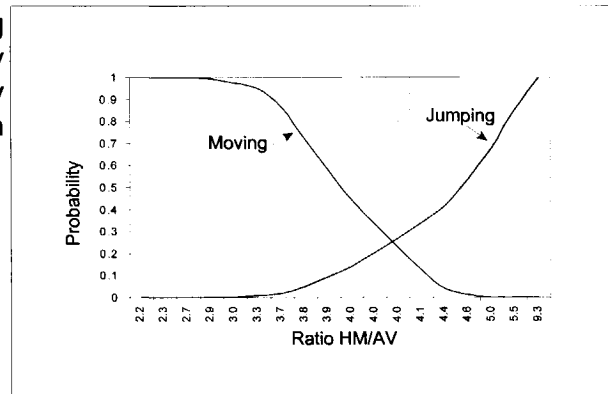


Figure 7.13: Cumulative probability distribution for moving and jumping particles.

The results shown in figures 7.12 and 7.13 were obtained with only one type of particle, in one type of GIS configuration. Therefore, we investigated six other particles in the laboratory setup and in a 150 kV and 380 kV GIS setup. An overview of the investigated particles is given in table 7.6. The particle number indicates one of the in total eighteen experiments which have been performed. In all experiments we were able to observe the particle movement. In 13 experiments, the particles were only moving and in the other 5 experiments, the particles were jumping.

Table 7.6: *Other types of particles investigated in the 420 kV test set-up.*

	Particle number:	Length [mm]:	Width [mm]:	Thickness [mm]:
	8, 9, 14	10	2.8	0.5
	10, 11	13	1	0.1
	3, 4, 13, 16, 18	24	2.8	0.5
	17	6	0.4	0.4
	5, 6, 7	7.6	2.8	0.5
○	1, 2, 12, 15	5	5	spherical

Evaluation of moving particles

For 13 particles we knew that they were only moving inside the GIS and not jumping. We used the following procedure to estimate the probability that the investigated particles were either moving or jumping:

- 1) We measured 20 sweeps using the spectrum analyser to process the averaged and hold max frequency spectra;
- 2) We processed the key-value AR of both averaged and hold max spectrum and calculated the ratio;
- 3) Using the cumulative distributions of moving and jumping particles shown in figure 7.13 we calculated the probability that the particle was moving or jumping.

This procedure was carried out for these thirteen particles and the result of this analysis is shown in figure 7.14:

- 1) the hollow bars give the probability that the analysed particle is moving;
- 2) the filled bars indicate the probability that the analysed particle is jumping.

To determine the particle movement, we used a minimum threshold of 50% probability. Next to the graph, the estimated particle movement is written. As can be seen, particles 1 to 9 have a probability larger than 50% that it is moving. Only particle 13 has a probability larger than 50% that it is jumping. Particles 10-12 have a probability below 50% for both moving and jumping and the classification is uncertain. So from the thirteen investigated moving particles, one was incorrectly classified as a jumping particle and the movement of three other particles was uncertain.

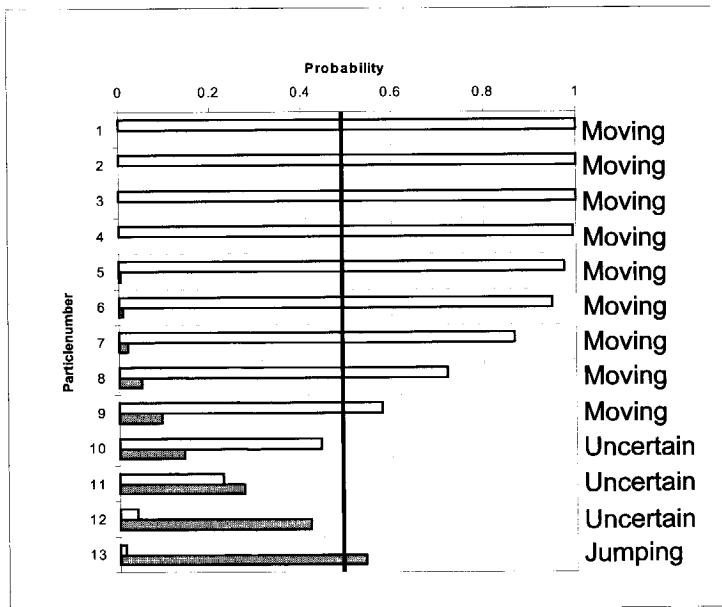


Figure 7.14: Probability analysis of moving particles: the probability that the particle is moving is indicated by the hollow bars, the probability that the particle is jumping is indicated by the filled bars.

Evaluation of jumping particles

The same analysis procedure was carried out for the five particles for which we knew that they were jumping. This result is shown in figure 7.15 and again the hollow bars indicate the probability that the analysed particle is moving and the filled bars indicate the probability that the analysed particle is jumping.

To determine the particle movement, we used again a minimum threshold of 50% probability as indicated in figure 7.15. Next to the graph, the estimated particle movement is written. As can be seen, particles 16 to 18 have a probability larger than 50% that it is jumping. Particles 14 and 15 have a probability below 50% for both moving and jumping and therefore the classification is uncertain. Also important to notice is the fact that none of the jumping particles was classified as a moving particle, which has lower criticality.

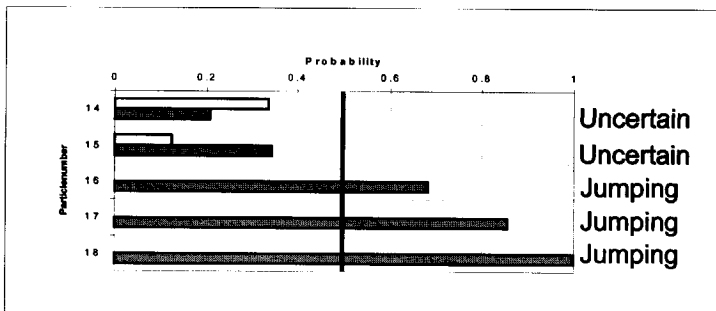


Figure 7.15: *Probability analysis of jumping particles: the probability that the particle is moving is indicated by the hollow bars, the probability that the particle is jumping is indicated by the filled bars.*

7.3 SUMMARY AND CONCLUSIONS

We have compared several PD-related phenomena of three types of PD sources: protrusions fixed to the high-voltage conductor or fixed to the enclosure, and free moving particles. These PD sources were investigated in pure SF_6 and in gas mixtures consisting of 5% SF_6 - 95% N_2 and 10% SF_6 - 90% N_2 .

In case of protrusions, the following can be concluded:

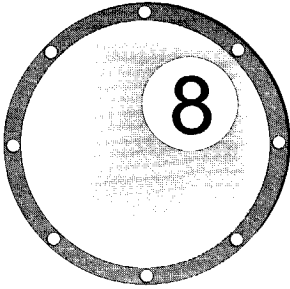
- 1) The PD patterns measured from fixed protrusions in the three gas types at the same test voltage are completely different. In pure SF_6 only small streamer discharges of equal amplitude were measured, while in both gas mixtures already leader activity was measurable.
- 2) As a consequence, the same protrusion under the same testing conditions is closer to a breakdown in the mixtures than in pure SF_6 . So mixtures are more sensitive to protrusions than pure SF_6 .

In case of free particles, the following can be concluded:

- 1) The frequency spectra measured for the three stages of movement are different in number of peaks and magnitude of the peaks;
- 2) The PD patterns and frequency spectra originating from free particles are highly similar in the three investigated gases.

In this chapter we described a first approach of the risk analysis of fixed protrusions and particles for a breakdown under nominal AC power-frequency conditions, using the UHF measuring technique. From the investigations, the following can be concluded:

- 1) The PD magnitude gives no significant information regarding the criticality of a defect;
 - 2) Three types of patterns in PD process of protrusions have been identified. A combined analysis of frequency spectra and PD patterns is necessary to determine the stage of the PD process for fixed protrusions;
 - 3) In case of free particles we observed three stages in the particle movement: shuffling particle, moving particle and jumping particle. The last is the most dangerous one as it can reach the high-voltage conductor;
 - 4) The ratio of the key-value AR processed from the hold max and averaged spectrum is differently distributed for moving and jumping particles;
 - 5) The particle movement evaluated from measuring results obtained with different particles in different configurations was correctly classified in 67% of the cases, was classified 'uncertain' in 28% of the cases and incorrectly in 5% of the cases.
-



CHAPTER 8 CONCLUSIONS

In this thesis we investigated the sensitivity of the ultra-high frequency partial-discharge measuring technique to determine the condition of the high-voltage insulation in gas-insulated systems. The following conclusions can be drawn:

Detection sensitivity

Important features for implementing PD detection to assess the presence of discharging insulation defects are:

- 1) The signal reduction is linear and the linear tendency depends on the type of GIS component and GIS configuration.
 - 2) UHF couplers could be located using transmission line models to ensure enough sensitivity (5 pC) to detect different types of defects.
 - 3) To implement this for long length GIS a correction in the order of 0.2 dB/m is necessary.
-

Partial discharge analysis

Based on PD analysis different conditions of the equipment can be distinguished as follows.

- 4) From measured phase-resolved PD patterns we can distinguish between different PD processes.
- 5) From measured UHF partial discharge frequency spectra we can process spectral peak amplitude distributions which can be statistically analysed to distinguish between different defects.

Dielectric properties of gases

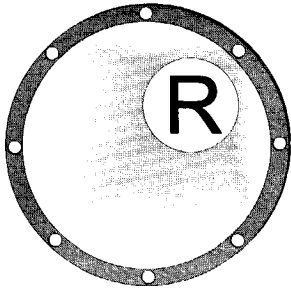
Using different gases, e.g. SF_6 - N_2 gas mixtures, the following aspects need attention.

- 6) To compare pure SF_6 with SF_6 - N_2 gas mixtures the same dielectric conditions, such as similar lightning impulse strength, applied test voltages and equivalent gas pressure have to be taken into account.
 - 7) The presence of N_2 (90% or 95%) in SF_6 results in a higher effective ionisation coefficient. As a result, the PD magnitude of, e.g. fixed protrusions, increases with a decreasing amount of SF_6 and the detectability of similar defects in gas mixtures is equal or better than in pure SF_6 .
 - 8) Due to the lower breakdown voltage in case of defects in gas mixtures higher priority has to be given to quality control compared to SF_6 insulated equipment.
-

Risk assessment

An important part of risk assessment is devoted to the criticality determination of discharging defects for an insulation breakdown.

- 9) The criticality of a defect is not related to the PD magnitude. The criticality of a discharging defect depends on the defect geometry, the partial discharge process and possible by-products.
 - 10) To assess the risk of fixed protrusions for AC breakdown, a combined analysis of frequency spectra and phase-resolved patterns of the defect is necessary.
 - 11) To discriminate between moving and jumping particles, spectral analysis can be used. The most critical stage in the particle movement is jumping and can be recognised using probability distributions processed from spectral analysis.
-



REFERENCES

- [1] W. Mosch, W. Hauschild, *Hochspannungsisolierungen mit Schwefelhexafluorid*, VEB Verlag Technik, Berlin, 1979, ISBN 3-7785-0540-8.
 - [2] H.M. Ryan, G.R. Jones, *SF₆ Switchgear*, Peter Peregrinus Ltd., London, UK, 1989, ISBN 0-86341-123-1.
 - [3] D. Kopejtkova, T. Molony, S. Kobayashi, I.M. Welch, *A twenty-five year review of experience with SF₆ gas insulated substations (GIS)*, CIGRE session 1992, paper 23-101.
 - [4] T.M. Chan, F. Heil, D. Kopejtkova, P. O'Connell, J.P. Taillebois, I. Welch, *Report on the second international survey on high voltage gas insulated substations (GIS) service experience*, CIGRE session 1998, paper 23-102.
 - [5] CIGRE Working Group 23.02, *Report on the Second International Survey on High Voltage Gas Insulated Substations (GIS) Service Experience*, CIGRE Brochure 150, February 2000.
 - [6] CIGRE Working Group 23.02, *Guide For SF₆ Gas Mixtures*, CIGRE Brochure 163, August 2000.
 - [7] Working Group 15.03, *Diagnostic Methods for GIS Insulating Systems*, CIGRE session 1992, paper 15/23-01.
 - [8] B.F. Hampton, J.S. Pearson, C.J. Jones, T. Irwin, I.M. Welch, B.M. Pryor, *Experience and Progress with UHF Diagnostics in GIS*, CIGRE session 1992, paper 15/23-03.
 - [9] S.A. Boggs, *Partial Discharge: Overview and Signal Generation*, IEEE Electrical Insulation Magazine, July/August 1990, Vol. 6, No. 4, pp. 33-39
-

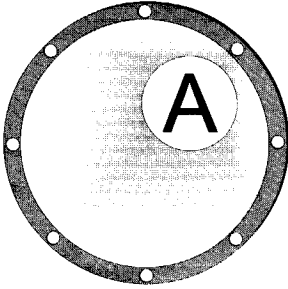
- [10] IEC Publication 517, *Gas-insulated metal-enclosed switchgear for rated voltages of 73.5 kV and above*, 3rd Edition, 1990
 - [11] B.F. Hampton, R.J. Meats, *Diagnostic measurements at UHF in gas insulated substations*, IEE Proceedings, Vol. 135, Pt. C, No. 2, pp. 137-144, 1988.
 - [12] IEC Publication 60270, *Partial Discharge Measurements*, 2nd Edition, 1981.
 - [13] L.E. Lundgaard, M. Runde, B. Skyberg, *Acoustic diagnosis of SF₆ gas insulated substations: a theoretical and experimental basis*, IEEE Transactions on Power Delivery, Vol. 5, No. 4, pp. 1751-1759, Oktober 1990.
 - [14] H.D. Schlemper, R. Kurrer and K. Feser, *Sensitivity of on-site partial discharge detection in GIS*, Proc. 8th Int. Symp. On HV Engineering, Yokohama, Vol. 3, 157-160, 1993
 - [15] J.S. Pearson, B.F. Hampton, A.G. Sellars, *A continuous UHF monitor for gas- insulated substations*, IEEE Transactions on Electrical Insulation, Vol. 26, No.3, pp. 469-478, 1991.
 - [16] E. Gulski, *Computer-aided Recognition of PD Using Statistical Tools*, Delft University Press, 1991.
 - [17] M.D. Judd, O. Farish, *High Bandwidth Measurement of Partial Discharge Current Pulses*, ISEI Paper of IEEE, Vol.2, pp.436-439, June 1998.
 - [18] B.F. Hampton, T. Irwin, D. Lightle, *Diagnostic measurements at ultra high frequency in GIS*, CIGRE session 1990, paper 15/33-01
 - [19] S. Meijer, E. Gulski, J.J. Smit, A.J.L.M. Kanters, *Determination of PD Sensitivity of GIS using Signal Reduction Measurements*, IEEE Int. Symp. on Electrical Insulation, Arlington, Vol. 1, pp. 65-68, 1998.
 - [20] R. Kurrer, K. Feser, *Attenuation Measurements of Ultra-High-Frequency Partial Discharge Signals in Gas-Insulated Substations*, 10th Int. Symp. on HV Engineering, Montreal, Vol. 2, pp. 161-164, 1997.
 - [21] G. Wanninger, *Ultrahochfrequente Teilentladungssignale in gasisolierten Schaltanlagen (GIS)*, Dissertation, University of München, Nr. 21-257, 1998 (in German).
 - [22] E. Gulski, *Digital analysis of partial discharges*, IEEE Trans. on Dielectrics and Elec. Insulation, Vol. 2 No. 5, pp. 822-837, 1995.
 - [23] R. Patsch, M. Hoof, *Pulse-sequence-analysis, a way to get a better insight into the physics of discharges*, International Conference on Partial Discharge, pp. 49-51, 1993.
-

- [24] F.H. Kreuger, *Industrial High Voltage*, Vol. I, Delft University Press, 1991.
 - [25] F.H. Kreuger, *Industrial High Voltage*, Vol. 2, Delft University Press, 1991.
 - [26] L.G. Christophorou, *Electron-molecule interactions and their applications, Volume 2*, Academic Press inc., Orlando, 1984, ISBN 0-12-174402-7.
 - [27] L.G. Christophorou and R.J. Van Brunt, *SF₆-N₂ mixtures Basic and HV insulation properties*, IEEE Transactions on Dielectrics and Electrical Insulation, Vol. 2 No. 5, October 1995.
 - [28] L. Niemeyer, L. Ullrich and N. Wiegart, *The Mechanism of Leader Breakdown in Electronegative Gases*, Transactions on Electrical Insulation, Vol. 24, No. 2, April 1989.
 - [29] T.B. Diarra, A. Béréal, F. Buret, E. Thuries, M. Guillen, Ph. Roussel, *N₂-SF₆ mixtures for High Voltage Gas Insulated Lines*, 10th Int. Symp. on HV Engineering, Montreal, 1997.
 - [30] M. Guillen, F. Buret, A. Beroual, *Lightning Impulse Withstand Voltage of a Gas-Insulated Line filled with N₂/SF₆*, ISH 1999, Volume 3, pp. 71-74.
 - [31] C.M. Cooke, R.E. Wootton, A.H. Cookson, *Influence of Particles on AC and DC Electrical Performance of Gas Insulated Systems at Extra-High-Voltage*, IEEE Transactions on Power Apparatus and Systems, Vol. PAS-96, no. 3, pp. 768-777, May/June 1977.
 - [32] M. Holmberg, *Motion of Metallic Particles in Gas Insulated Systems*, Chalmers Bibliotek, Reproservice, Göteborg, 1997, ISBN 91-7197-533-0.
 - [33] R. Baumgartner, B. Fruth, W. Lanz, K. Pettersson, *Partial Discharge - Part IX: PD in GIS - Fundamental considerations*, IEEE Electrical Insulation Magazine, Vol. 7, No. 6, November/December 1991.
 - [34] H. Blok, P.M. van den Berg, *Electromagnetic Waves*, Lecture notes.
 - [35] C.T.A. Johnk, *Engineering Electromagnetic fields and waves*, John Wily & Sons, Inc., 1975.
 - [36] S. Ramo, J.R. Whinnery, T. Van Duzer, *Fields and Waves in Communication Electronics*, John Wiley & Sons, Inc., 1965.
 - [37] C.R. Paul, S.A. Nasar, *Introduction to Electromagnetic Fields*, McGraw-Hill, Inc., 1982, ISBN 0-07-045908-8.
 - [38] J.D. Kraus, K.R. Carver, *Electromagnetics*, McGraw-Hill, Inc., 1953, ISBN 0-07-035396-4.
-

- [39] R. Kurrer, *Teilentladungsmessung im Gigahertz-Frequenzbereich an SF₆-isolierten Schaltanlagen*, Shaker Verlag GmbH, 1997, ISBN 3-8265-2211-7 (in German).
 - [40] S. Meijer, R.G.A. Zoetmulder, J.J. Smit, E.R.S. Groot, M.D. Judd, *Development and Application of a Portable Multipurpose On-Site/On-Line PD Measuring System*, 8th DMMA 2000, Edinburgh, 17-21 September 2000, pp. 133-138
 - [41] Leon W. Couch II, *Digital and Analog communication systems*, Macmillan Publishing Company, New York, 1993.
 - [42] T. Tsurimoto, H. Moto, M. Doi, K. Ito, H. Fujii, *Correlation between two frequency components of various PD pulses in GIS*, ISEIM 1998, P2-15
 - [43] A. Krivda, *Automated Recognition of Partial Discharges*, IEEE Trans. on Dielectrics and Elec. Insulation, Vol. 2 No. 5, pp. 796-821, 1995.
 - [44] E. Gulski, P. Seitz, *Computer-aided Registration and Analysis of Partial Discharges in High Voltage Equipments*, 8th ISH Yokohama, 1993
 - [45] A. Krivda, *Recognition of Discharges, Discrimination and Classification*, Delft University Press, 1995
 - [46] E. Gulski, *Computer-aided Measurement of Partial Discharges in HV Equipment*, IEEE Trans. on Elec. Insulation, Vol 28, No.6, pp. 969-983, 1993.
 - [47] W. Ziomek, H.-D. Schlemper, K. Feser, *Computer Aided Recognition of Defects in GIS*, IEEE International Symp. On Electr. Insulation, pp. 91-94, Montreal, 1996.
 - [48] S. Meijer, E. Gulski, J.J. Smit, *Pattern Analysis of Partial Discharges in SF₆*, IEEE Trans. on Dielectrics and Electrical Insulation, Vol. 5, No. 6, pp. 830-842, December 1998.
 - [49] S. Meijer, E. Gulski, P. Wester, A.J.L.M. Kanters, A. Girodet, T.S. Ramu, *Advanced Partial Discharge Diagnostics as Early Warning System to Recognize defects in gas-insulated Switchgear (GIS)*, CIGRÉ-report 15-308, Paris.
 - [50] R.E. Collin, *Field theory of guided waves*, McGraw-Hill book company, inc., 1960.
 - [51] Electra Paper of CIGRE TF 15/33.03.05, *PD Detection System for GIS: Sensitivity Verification for the UHF Method and the Acoustic Method*, Electra No. 183, April 1999.
-

- [52] H. Lautenschläger, *Investigations to pre-discharges and breakdown in gaseous insulation of SF₆ and SF₆-mixtures in inhomogeneous field*, Ph.D. Thesis University of Darmstadt, 1985 (in German).
 - [53] Y. Hoshina, M. Sato, H. Murase, M. Toyoda, A. Kobayashi, *Dielectric Properties of SF₆/N₂ Gas Mixtures on a Full Scale Model of the Gas-insulated Busbar*, Power Engineering Society Winter Meeting, Volume 3, pp 2129-2134, 2000.
 - [54] *Cutting the cost of piped power*, Trans-Power Europe Magazine, Vol. 1, No. 1, March 2001, pp.14-16.
 - [55] A.G. Sellars, O. Farish and M.M. Peterson, *UHF detection of Leader Discharges in SF₆*, IEEE Tr. On Dielectrics and Electrical Insulation, Vol. 2, No. 1, February 1995, pp. 143-154.
 - [56] M. Wohlmuth, *Criticality of moving particles in GIS*, 9th ISH Graz, Austria, 1995, paper 2292.
 - [57] H.-D. Schlemper, K. Feser, *Estimation of Mass and Length of Moving Particles in GIS by Combined Acoustical and Electrical PD Detection*, Conference on Electrical Insulation and Dielectric Phenomena, pp. 90-93, 1996.
 - [58] A. Kutil, *Qualification of Fiber-reinforced Insulating Materials Based on PD Analysis*, IEEE Trans. on Dielectrics and Electrical Insulation, Vol. 5, No. 4, pp. 603-611, August 1998.
 - [59] F. Gutfleisch, L. Niemeyer, *Measurement and Simulation of PD in Epoxy Voids*, IEEE Trans. on Dielectrics and Electrical Insulation, Vol. 2, No. 5, pp. 729-743, October 1995.
 - [60] Society for Risk Analysis, *Glossary of Risk Analysis Terms*, www.sra.org, September 26, 2000
 - [61] L.E. Lundgaard, B. Skyberg, A. Diessner, A. Schei, *Method and Instrumentation for Acoustic Diagnoses of GIS*, CIGRE-report 15-309, Paris, 2000
 - [62] K. Feser, R. Kurrer, *Insulation Monitoring of Gas-Insulated Substations with Respect to Life Cycle*, Tutorial In-Service Diagnostics of High Voltage Power Apparatus, ISH 1997.
 - [63] H.-D. Schlemper, *Akustische und elektrische Teilentladungsmessung zur Vor-Ort-Prüfung von SF₆-solorieten schaltanlagen*, Ph.D. Thesis University of Stuttgart, 1997 (in German).
-

- [64] Y. Qiu, Y.P. Feng, *Calculation of Dielectric Strength of the SF_6/N_2 Gas Mixture in Macroscopically and Microscopically Non-Uniform Fields*, Proc. Of the 4th Int. Conference on Properties and Applications of Dielectric Materials, paper 4225, pp 87-90, July 3-8, 1994, Brisbane Australia.
 - [65] S. Meijer, E. Golski, J.J. Smit, F.J. Wester, T. Grun, M. Turner, *Interpretation of PD in GIS using Spectral Analysis*, paper 5.124.S16, 11th ISH, London, 1999.
 - [66] S. Meijer, W.R. Rutgers and J.J. Smit, *Acquisition of partial discharges in SF_6 insulation*, Conference on Electrical Insulation and Dielectric Phenomena, pp. 581-584, 1996.
 - [67] L. Niemeyer, *A Generalized Approach to Partial Discharge Modeling*, IEEE Trans. on Dielectrics and Electrical Insulation, Vol. 2, No. 5, pp. 729-743, October 1995.
-



APPENDIX A ELECTROMAGNETIC FIELD CALCULATION

In this appendix, a more detailed description of the calculation of electromagnetic waves in gas-insulated systems is given. The electromagnetic waves can be described by the wave equations for the electric and magnetic field, derived from the Maxwell equations, (A.1): Faraday's Law, Ampere's Law, Gauss' Law and Magnetic Flux Continuity [34-38].

$$\left\{ \begin{array}{l} \nabla \times \vec{E} + \frac{\partial \mu \vec{H}}{\partial t} = -\vec{K}^e \\ -\nabla \times \vec{H} + \sigma \vec{E} + \frac{\partial \epsilon \vec{E}}{\partial t} = -\vec{J}^e \\ \nabla \cdot \epsilon \vec{E} = \rho \\ \nabla \cdot \mu \vec{H} = 0 \end{array} \right. \quad (A.1)$$

where μ is the permeability of the gas, ϵ is the permittivity of the gas, σ is the conductivity of the gas, ρ is the charge density in the gas, \vec{E} the electric field intensity, \vec{H} the magnetic field intensity, the J^{ext} current density from an external source, K^{ext} the surface current density from an external source and $\vec{B} = \mu \vec{H}$.

Assuming that the fields vary harmonically in time with a frequency ω and that no external sources are present, these equations can be written as

$$\begin{cases} \nabla \times \hat{E} = -j\omega\mu\hat{H} \\ -\nabla \times \hat{H} = (\sigma + j\omega\epsilon\hat{E}) \\ \nabla \cdot \hat{D} = \rho \\ \nabla \cdot \hat{B} = 0 \end{cases} \quad (\text{A.2})$$

We started from these well-known equations to study the propagation of electromagnetic waves in GIS.

TEM MODE

A typical GIS configuration is shown in figure A.1. Because of its cylindrical configuration cylindrical coordinates have been used:

$$\begin{cases} x = r \cdot \cos \varphi \\ y = r \cdot \sin \varphi \\ r = \sqrt{x^2 + y^2} \\ \varphi = \arctan\left(\frac{y}{x}\right) \end{cases} \quad (\text{A.3})$$

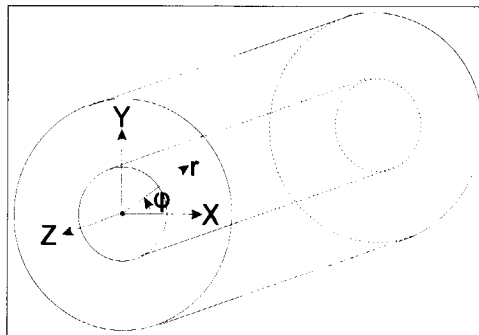


Figure A.1: GIS construction with cylindrical coordinates.

Then the first two equations of (A.2) result in the following sets of equations (A.4 and A.5):

$$\begin{cases} \frac{\partial \hat{E}_z}{r \partial \varphi} - \frac{\partial \hat{E}_\varphi}{\partial z} = -j\omega\mu \hat{H}_r \\ \frac{\partial \hat{E}_r}{\partial z} - \frac{\partial \hat{E}_z}{\partial r} = -j\omega\mu \hat{H}_\varphi \\ \frac{\partial(r \hat{E}_\varphi)}{r \partial r} - \frac{\partial \hat{E}_r}{r \partial \varphi} = -j\omega\mu \hat{H}_z \end{cases} \quad (\text{A.4})$$

$$\begin{cases} \frac{\partial \hat{H}_z}{r \partial \varphi} - \frac{\partial \hat{H}_\varphi}{\partial z} = (\sigma + j\omega\epsilon) \hat{E}_r \\ \frac{\partial \hat{H}_r}{\partial z} - \frac{\partial \hat{H}_z}{\partial r} = (\sigma + j\omega\epsilon) \hat{E}_\varphi \\ \frac{\partial(r \hat{H}_\varphi)}{r \partial r} - \frac{\partial \hat{H}_r}{r \partial \varphi} = (\sigma + j\omega\epsilon) \hat{E}_z \end{cases} \quad (\text{A.5})$$

For TEM propagation of signals in the z-direction the field components $E_z=0$ and $H_z=0$. Furthermore, the fields are invariant in the φ -direction, which means that

$$\begin{cases} \frac{\partial \hat{E}_i}{\partial \varphi} = 0 \\ \frac{\partial \hat{H}_i}{\partial \varphi} = 0 \end{cases} \quad i = r, \varphi, z \quad (\text{A.6})$$

As a result the following set of equations are obtained from (A.4 and A.5):

$$\left\{ \begin{array}{l} -\frac{\partial \hat{E}_\varphi}{\partial z} = -j\omega\mu \hat{H}_r \\ \frac{\partial \hat{E}_r}{\partial z} = -j\omega\mu \hat{H}_\varphi \\ \frac{\partial(r \hat{E}_\varphi)}{r\partial r} = 0 \end{array} \right. \quad (\text{A.7})$$

$$\left\{ \begin{array}{l} -\frac{\partial \hat{H}_\varphi}{\partial z} = (\sigma + j\omega\epsilon) \hat{E}_r \\ \frac{\partial \hat{H}_r}{\partial z} = (\sigma + j\omega\epsilon) \hat{E}_\varphi \\ \frac{\partial(r \hat{H}_\varphi)}{r\partial r} = 0 \end{array} \right. \quad (\text{A.8})$$

Moreover, because the electric field is tangential, $\hat{E}_\varphi=0$, and because the magnetic field is radial, $\hat{H}_r = 0$. So the following equations remain:

$$\left\{ \begin{array}{l} -\frac{\partial \hat{H}_\varphi}{\partial z} = (\sigma + j\omega\epsilon) \hat{E}_r \\ \frac{\partial(r \hat{H}_\varphi)}{r\partial r} = 0 \\ \frac{\partial \hat{E}_r}{\partial z} = -j\omega\mu \hat{H}_\varphi \end{array} \right. \quad (\text{A.9})$$

\hat{E}_r and \hat{H}_ϕ can be expressed by

$$\begin{cases} \hat{E}_r = e_r(r) \hat{V}(z, j\omega) \\ \hat{H}_\phi = h_\phi(r) \hat{I}(z, j\omega) \end{cases} \quad (\text{A.10})$$

in which $e_r(r)$ and $h_\phi(r)$ are the transverse components of the field and $V(z, j\omega)$ and $I(z, j\omega)$ are the voltage and current.

Substituting (A.10) in (A.9) the following set of equations can be used to calculate $h_\phi(r)$:

$$\begin{cases} h_\phi(r) \frac{\partial \hat{I}(z, j\omega)}{\partial z} + (\sigma + j\omega\epsilon) e_r(r) \hat{V}(z, j\omega) = 0 \\ \hat{I}(z, j\omega) \frac{\partial (r h_\phi(r))}{r \partial r} = 0 \\ e_r(r) \frac{\partial \hat{V}(z, j\omega)}{\partial z} + j\omega\mu h_\phi(r) \hat{I}(z, j\omega) = 0 \end{cases} \quad (\text{A.11})$$

To solve these equations to find $h_\phi(r)$, a scalar potential function in the transverse plane between both conductors can be introduced as

$$\left. \begin{array}{l} \varphi(r) = A + B \ln r \\ \text{enclosure } r = r_0: \varphi(b) = 0 = A + B \ln r_0 \\ \text{conductor } r = r_i: \varphi(a) = 1 = A + B \ln r_i \end{array} \right\} \varphi(r) = \frac{\ln\left(\frac{r_0}{r}\right)}{\ln\left(\frac{r_0}{r_i}\right)} \quad (\text{A.12})$$

which results in the following equation for the $e_r(r)$:

$$e_r(r) = -\nabla\varphi = -\frac{1}{r \ln\left(\frac{r_0}{r_i}\right)} \quad (\text{A.13})$$

As a result, $h_\phi(r)$ can be calculated from (A.11):

$$h_\phi(r) = \frac{\gamma}{j\omega\mu} Z_0 e_r(r) = \frac{\gamma}{j\omega\mu} Z_0 \frac{1}{r \ln\left(\frac{r_o}{r_i}\right)} \quad (\text{A.14})$$

and we know how the electric and magnetic field components vary with the radial position. To solve the dependence on the z -direction, the method of separation of variables has been applied to equation (A.11) to obtain:

$$\left\{ \begin{array}{l} \frac{\partial \hat{l}(z, j\omega)}{\hat{V}(z, j\omega) \partial z} = -\frac{(\sigma + j\omega\epsilon) e_r(r)}{h_\phi(r)} = -\gamma Y_0 \\ \frac{\partial \hat{V}(z, j\omega)}{\hat{l}(z, j\omega) \partial z} = -\frac{j\omega\mu h_\phi(r)}{e_r(r)} = -\gamma Z_0 \end{array} \right. \quad Z_0 = \frac{1}{Y_0} \quad (\text{A.15})$$

where γ is the propagation constant and Z_0 is the characteristic impedance of the coaxial structure defined by

$$Z_0 = \frac{\hat{V}^+(z, j\omega)}{\hat{l}^+(z, j\omega)} \quad (\text{A.16})$$

For the propagation in the z -direction equation (A.15) can be rewritten as:

$$\left\{ \begin{array}{l} \frac{\partial \hat{l}(z, j\omega)}{\hat{V}(z, j\omega) \partial z} = -\gamma Y_0 \Rightarrow \hat{V}(z, j\omega) = \frac{-1}{\gamma Y_0} \frac{\partial \hat{l}(z, j\omega)}{\partial z} \\ \frac{\partial \hat{V}(z, j\omega)}{\hat{l}(z, j\omega) \partial z} = -\gamma Z_0 \Rightarrow \hat{l}(z, j\omega) = \frac{-1}{\gamma Z_0} \frac{\partial \hat{V}(z, j\omega)}{\partial z} \end{array} \right. \quad (\text{A.17})$$

Substituting the second equation of (A.17) in the first equation of (A.17) and vice versa gives:

$$\begin{cases} \frac{\partial^2 \hat{I}(z, j\omega)}{\partial z^2} = \gamma^2 \hat{I}(z, j\omega) \\ \frac{\partial^2 \hat{V}(z, j\omega)}{\partial z^2} = \gamma^2 \hat{V}(z, j\omega) \end{cases} \quad (\text{A.18})$$

These wave equations [38] have the following solutions consisting of a combination of forward and backward travelling waves

$$\begin{cases} \hat{V}(z, j\omega) = \overbrace{\hat{V}^+(j\omega)e^{-\gamma z}}^{\text{forward}} + \overbrace{\hat{V}^-(j\omega)e^{\gamma z}}^{\text{backward}} \\ \hat{I}(z, j\omega) = \hat{I}^+(j\omega)e^{-\gamma z} + \hat{I}^-(j\omega)e^{\gamma z} \end{cases} \quad (\text{A.19})$$

With

$$\begin{cases} \hat{V}^+ = Z_0 \hat{I}^+ \\ \hat{V}^- = -Z_0 \hat{I}^- \\ \gamma = \sqrt{j\omega\mu(\sigma + j\omega\epsilon)} \end{cases} \quad (\text{A.20})$$

Now the characteristic impedance Z_0 can be calculated using

$$\iint_{\{r, \phi\} \in D} \mathbf{e}_r h_\phi i_3 dA = 1 \quad (\text{A.21})$$

resulting in

$$Z_0 = \sqrt{\frac{j\omega\mu}{\sigma + j\omega\epsilon}} \frac{\ln\left(\frac{r_o}{r_i}\right)}{2\pi} \quad (\text{A.22})$$

As a result the propagating TEM-modes are fully described.

HIGHER ORDER MODES

The electromagnetic waves not only propagate in the TEM-mode, but also in higher-order modes. These modes can be calculated from the wave equations [36]

$$\begin{cases} \nabla^2 \hat{E} = -\omega^2 \mu \epsilon \hat{E} \\ \nabla^2 \hat{H} = -\omega^2 \mu \epsilon \hat{H} \end{cases} \quad (\text{A.23})$$

Because only propagation in the z-direction has been assumed as $e^{\pm\gamma z}$, the wave equation reduces to a dependency on only the transverse variables r and ϕ . Based on these assumptions it is possible to express the transverse field components E_ϕ , E_r , H_ϕ and H_r in terms of the longitudinal components E_z and H_z . The field solutions can be characterized either by transverse-electric (TE) modes or by transverse-magnetic (TM) modes: $E_z=0$ or $H_z=0$. Now only the field in the z-direction have to be solved. Because the calculation of the electric and magnetic field is similar, only the electric-field calculation is shown:

$$\frac{1}{r} \frac{\partial}{\partial r} \left(r \frac{\partial E_z}{\partial r} \right) + \frac{1}{r^2} \frac{\partial^2 E_z}{\partial \phi^2} + \gamma^2 E_z = -\omega^2 \mu \epsilon E_z \quad (\text{A.24})$$

which can be rewritten as

$$\frac{1}{r} \frac{\partial E_z}{\partial r} + \frac{1}{r^2} \frac{\partial^2 E_z}{\partial \phi^2} + \frac{\partial^2 E_z}{\partial r^2} = -k^2 E_z \quad (\text{A.25})$$

where k is

$$k^2 = \gamma^2 + \omega^2 \mu \epsilon \quad (\text{A.26})$$

To solve this equation we define:

$$E_z(r, \phi) = F(\phi)R(r) \quad (\text{A.27})$$

Now (A.24) can be rewritten as

$$F(\varphi)R''(r) + \frac{1}{r}F(\varphi)R'(r) + \frac{1}{r^2}F''(\varphi)R(r) = -k^2F(\varphi)R(r) \quad (\text{A.28})$$

Separating the variables gives us

$$r^2 \frac{R''(r)}{R(r)} + r \frac{R'(r)}{R(r)} + k^2 r^2 = -\frac{F''(\varphi)}{F(\varphi)} \quad (\text{A.29})$$

Because each side of the equation is a function of only one variable, each side has to be constant. Assume this constant to be m^2 then we can rewrite (A.29) to

$$\begin{cases} -\frac{F''(\varphi)}{F(\varphi)} = m^2 \\ R''(r) + \frac{1}{r}R'(r) + \left(k^2 - \frac{m^2}{r^2}\right)R(r) = 0 \end{cases} \quad (\text{A.30})$$

The solution of the first of these equations is in sinusoids:

$$F(\varphi) = C_X \cos(m\varphi) + D_X \sin(m\varphi) \quad X = E, H \quad (\text{A.31})$$

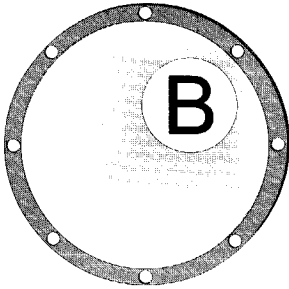
A solution of the second of these equations can be written in terms of Bessel functions of order m :

$$R(r) = A_X J_m(k \cdot r) + B_X N_m(k \cdot r) \quad X = E, H \quad (\text{A.32})$$

in which J_m is the Bessel function of order m and N_m is the Neumann function of order m [38], A_E , B_E , A_H and B_H are constants. In the same way, a similar equation can be determined for the magnetic field. Finally, the electric and magnetic field-component in the axial direction is described by:

$$\begin{cases} E_z = R_E(r) \cdot F_E(\varphi) \cdot e^{-\gamma z} \\ H_z = R_H(r) \cdot F_H(\varphi) \cdot e^{-\gamma z} \end{cases} \quad (\text{A.33})$$

These equations can be used to calculate the cut-off frequencies of the possible higher-order propagation modes.



APPENDIX B OPTIMISATION SPECTRUM ANALYSER SETTINGS

In this Appendix experiments are described which have been used to find the most sensitive setting of the spectrum analyser.

1) PD measurement in the frequency domain

The first step in finding an appropriate frequency range for a VHF/UHF PD measurement is the measurement of a broad frequency span up to several GHz, see figure B.2. Using a HP 8590L the spectrum is analysed up to 1.8 GHz. It takes time to sweep from zero to 1.8 GHz: the sweep time.

It is known that for proper use of a SA the input signal has to be stable in magnitude, pulse shape etc. A PD pulse however, can not be considered as a stable input signal. To be able to apply the VHF/UHF method, we optimised the following important spectrum analyser settings: sweep time, total time of a measurement and acquisition mode [66].

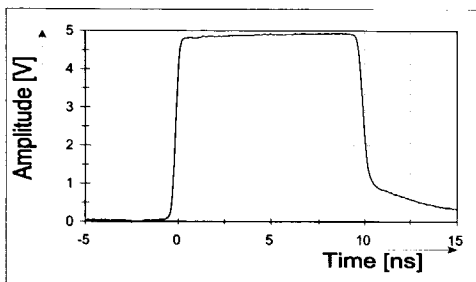


Figure B.1: Pulse shape generated by the Picosecond Pulse Labs 2000D pulse generator: rise time = 400 ps, pulse width = 10 ns.

Increasing the sweep time increases the time available for the measurement. As a result, the SA can use a smaller frequency step size to step through the frequency spectrum. Hence more accuracy is

obtained. We investigated the influence of the sweep time on the number of detected pulses.

The tests have been carried out using a fast pulse generator, Picosecond Pulse Labs model 2000D, which generates pulses with a rise time of 400 ps and a pulse width of 10 ns, figure B.1. Typically, the repetition rate between successive pulses in a PD process can vary between a few Hz (free particles) and several hundreds of Hz (fixed protrusions) [32, 67]. Obviously detection of PD pulses with a low repetition rate is more difficult than those with a high repetition rate. Therefore, we simulated a PD process with a low repetition rate by injecting pulses with a repetition rate of only 1 Hz.

Table B.1 shows the influence of the sweep time on the number of detected pulses from a series of randomly injected pulses. From the table we can conclude that to detect 90% of all injected pulses the sweep time has to be at least 5 s.

Table B.1: *Percentage of processed pulses out of 50 randomly injected pulses as function of the sweep time.*

Sweep time:	Percentage of processed pulses:
36 ms	40 %
100 ms	70 %
500 ms	80 %
1 s	80 %
5 s	90 %
10 s	90 %

2) Spectral analysis of the measured PD frequency spectrum

The second step is analysis of the measured PD frequency spectrum. The PD pulse shape (i.e. the rise and fall time, pulse duration and pulse height) and the repetition rate of the PD pulses vary for each pulse. As a result the frequency spectrum can change during each sweep. However, for further analysis of a frequency spectrum a stable spectrum is necessary. To obtain a stable frequency spectrum, the results of several sweeps can be processed in two ways:

- a) Hold max: process a stable frequency spectrum from the maximum amplitudes at each frequency as measured during the series of sweeps.
- b) Averaging: process a stable frequency spectrum by averaging the measured amplitudes at each frequency over the series of sweeps.

The experiments show that a measurement consisting of 20 sweeps of 5s results in a frequency spectrum containing sufficient information, irrespective of the PD source type and the processing of the frequency spectrum, see table B.2.

Table B.2: *Measurement time required to build up a stable frequency spectrum as function of the repetition rate of the pulse generator.*

Repetition rate:	Stable spectrum using max hold after:	Stable spectrum using averaging after:
1 Hz	20 sweeps	12 sweeps
10 Hz	10 sweeps	10 sweeps
100 Hz	10 sweeps	10 sweeps
1 kHz	8 sweeps	8 sweeps

3) PD measurement in time domain

From the measured spectrum a frequency range well above the noise level can be selected for phase-resolved VHF/UHF PD analysis. For further analysis of the signals at this selected measuring frequency, we used the SA to demodulate the signals into the range of a few MHz in the following way:

- The centre frequency f_c of the SA is set to the selected measuring frequency,
- The measured span is set to zero: the zero span mode of the SA,
- The sweep time is set to 20 ms and the triggering is synchronised with the test voltage to obtain phase-resolved patterns correlated to the 50 Hz sine wave.

In the zero span mode the passed frequency band is determined by the resolution bandwidth (RBW). In fact, the frequencies between $f_c - \frac{1}{2}RBW$ and $f_c + \frac{1}{2}RBW$ are further processed. Therefore, the SA can be seen as a bandpass filter with a tunable centre frequency f_c , see figure B.2.

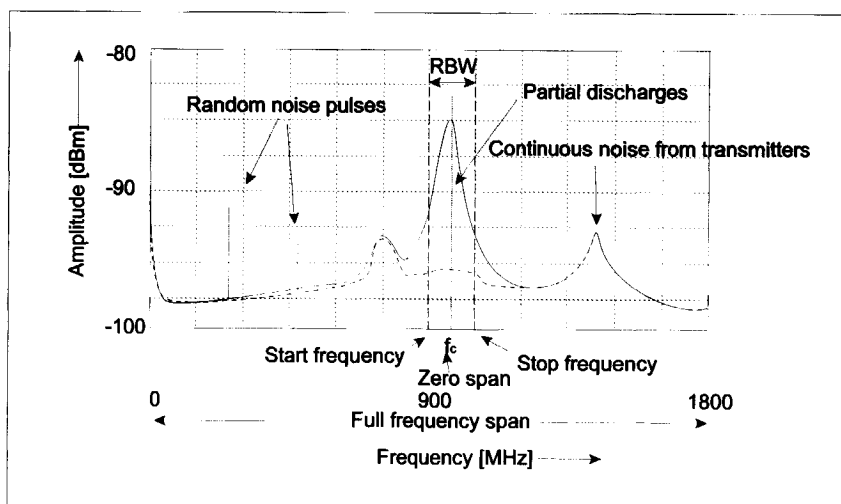
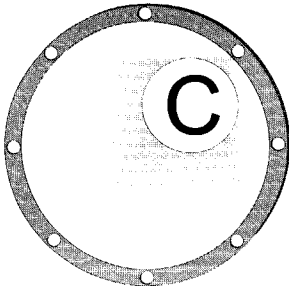


Figure B.2: Example of a frequency spectrum measured at a UHF coupler of a GIS installation.

Dashed line: background spectrum

Solid line: background plus PD spectrum



APPENDIX C

PROCEDURE TO CALCULATE REFLECTION COEFFICIENTS

In this Appendix a procedure is described which has been followed to calculate the reflection coefficients of GIS components, based on experimental results.

C.1 ANALYSIS OF SPACER TRANSMISSION LINE MODEL

In chapter 4, we modelled the influence of one or two spacers on the propagation of high-frequency PD signals. As a result, we compared the measured and estimated frequency spectra shown in figures 4.4 and 4.6. We could conclude that the spectra look rather similar, however, due to the many resonance peaks it is difficult to compare the magnitude of the frequency spectra. Therefore, we calculated the UHF signal using the key value AR as has been described in chapter 3. The results are shown in figure C.1.

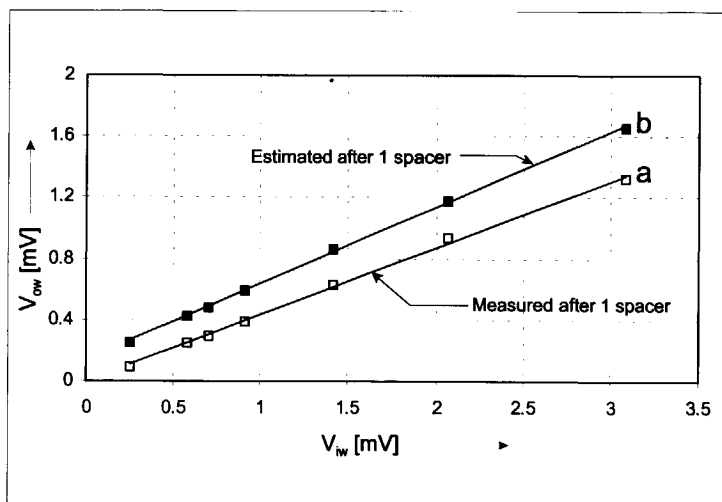


Figure C.1: UHF signal extracted from the measured (hollow squares) and estimated (filled squares) spectra before and after one spacer. V_{iw} is the voltage at the coupler close before the spacer due to the incoming waves; V_{ow} is the voltage measured at the coupler close after the spacer due to the outgoing waves.

To obtain figure C.1 artificial pulses with different amplitudes have been injected somewhere in the GIS setup, using the pulse generator described in Appendix B. The artificial pulses excite electromagnetic waves which propagate into the direction of a spacer. The voltage level V_{iw} due to the incoming waves is measured at a UHF coupler just before they encounter the spacer. A voltage level V_{ow} is measured at the UHF coupler just after the spacer, due to the em-waves transmitted through the spacer. The differences in the measured voltage levels before and after the spacer is a measure for two occurring effects:

- 1) the attenuation of the em-waves by the spacer and
- 2) the influence of the resonance cavity in which the UHF couplers are located.

In figure C.1 two different relations between the voltage levels before and after the spacer are shown:

- a) the actual measured voltage level after the spacer;
- b) the estimated voltage level after the spacer.

It can be seen that the estimated voltage level after the spacer is higher than the actual measured voltage level. This can be explained by the fact the estimated reduction in the frequency range around 1 GHz is negligible as described in section 4.2. However, from the actual measurements can be concluded that there is a change in this frequency range. Consequently, the voltage level measured at the UHF coupler after the spacer is higher for the estimated spectrum than for the measured frequency spectrum.

Another way of plotting the data is shown in figure C.2. Here we plotted the ratio of the voltage levels before and after propagating through one or two spacers against the voltage before the spacer(s).

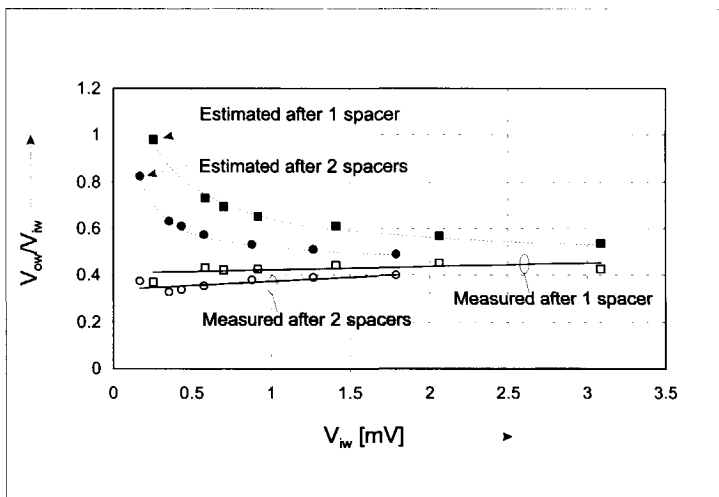


Figure C.2: Ratio between the UHF signal extracted from the measured and estimated spectra before and after one spacer (squares) or two spacers (circles).

As expected, the ratio for one spacer is higher compared to two spacers. Moreover, the ratio of the actual measured values is approximately constant. In contrast, the estimated values show a scatter especially for smaller incoming waves. For higher signals, the estimated and measured values tend to the same ratio. Again, this can be explained by the fact that the estimation has no signal change in the frequency range around 1000 MHz. This results in a certain off-set, which of course has a larger influence on smaller signals.

From figure C.1 and C.2 we can draw several conclusions:

- 1) As expected, the magnitude of the frequency spectrum measured after a component (spacer) depends on the magnitude of the incoming em-waves incident to the component.
- 2) The ratio between the voltage measured before the GIS component due to incoming em-waves and the voltage measured after the same component is approximately constant for the measured frequency spectra.

From the results shown in figure C.2 we can calculate the overall transmission coefficient (overall transmission coefficient means the transmission coefficient of the spacer(s) and the influence of the resonance cavities in which the UHF couplers are mounted) which is the mean value of all ratios. From table C.1 can be concluded that the spread in the transmission coefficient from the measured frequency spectra is rather small (<10%); the spread in the estimated transmission coefficient is larger (approximately 22%).

Table C.1: *Measured and estimated overall transmission coefficient for 1 and 2 spacers.*

Nr. of spacers	Overall transmission coefficient	
	Measured	Estimated
1	0.43±0.03	0.68±0.15
2	0.37±0.03	0.60±0.11

C.2 TRANSMISSION LINE COEFFICIENTS OF A SPACER

The first approach physical modelling confirms the physics of the propagation effects in GIS. However, more accurate modelling is not practical since we use empirical values, assuming the linear correlation as stated above. Besides the measurements shown in figure C.1 to investigate the influence of a spacer on the measured PD signals, we carried out measurements in five other configurations. The ratios of the voltage measured at the UHF coupler before the spacer and after the spacer are

plotted against the voltage measured at the UHF coupler before the spacer due to the incoming em-waves, see figure C.3.

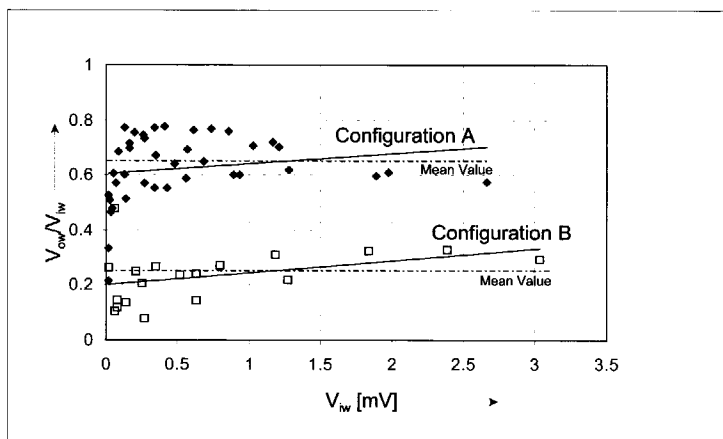


Figure C.3: Ratio between the UHF signal extracted from the measured and estimated spectra before and after spacers at different locations in the test setup.

Two different clusters of measurements can be observed. These clusters of measurements can be explained by the fact that two different types of configurations have been used to investigate the spacer:

Configuration A: The detecting UHF coupler is located between two spacers;

Configuration B: The detecting UHF coupler is located between a spacer and a bushing.

As stated before, the signal reduction not only depends on the investigated GIS component, but on the complete GIS configuration under investigation.

In the following a procedure is described which has been used to calculate the reflection coefficients of each GIS component. Therefore, we used a transmission line model to describe each GIS component.

The reflection coefficient of a spacer located in a configuration of type A as shown in figure 4.2 can be calculated using equations (4.4) and (4.5) with the following set of data:

$$\begin{cases} r_1 = 0 \\ r_2 = r \\ r_3 = -r \\ r_4 = 0 \\ r_5 = r \\ r_6 = -r \\ t_i = 1 + r_i \end{cases} \quad (C.1)$$

the transmission line model can be written as:

$$\begin{bmatrix} S_a^+ \\ S_a^- \end{bmatrix} = A_1 A_2 A_3 A_4 A_5 A_6 \begin{bmatrix} S_b^+ \\ S_b^- \end{bmatrix} = M \begin{bmatrix} S_b^+ \\ S_b^- \end{bmatrix} \quad (C.2)$$

With this formula it is possible to estimate the UHF signal measured at UHF coupler \mathcal{C}_1 (figure C.3) by $S_{C1} = S_a^+ + S_a^-$. Suppose that there is an infinitely long GIS after the second spacer. Then the backward propagating wave $S_b^- = 0$ and the measured UHF signal at coupler \mathcal{C}_1 solely depends on the forward propagating wave S_b^+ :

$$S_{C1} = S_a^+ + S_a^- = (M_{11} + M_{21})S_b^+ \quad (C.3)$$

The measurements have been obtained at UHF coupler \mathcal{C}_2 . The UHF signal S_{C2} at this point can be calculated using:

$$\begin{bmatrix} S_c^+ \\ S_c^- \end{bmatrix} = A_4 A_5 A_6 \begin{bmatrix} S_b^+ \\ S_b^- \end{bmatrix} = N \begin{bmatrix} S_b^+ \\ S_b^- \end{bmatrix} \quad (C.4)$$

Again the backward propagating wave $S_b^- = 0$ so the UHF signal at coupler \mathcal{C}_2 can be determined by:

$$S_{C2} = S_c^+ + S_c^- = (N_{11} + N_{21})S_b^+ \quad (C.5)$$

From the results obtained in configuration A as shown in figure C.3 we know the ratio of the UHF signal measured at coupler C_1 and coupler C_2 : 0.63. Then, using (C.3) and (C.5) ratio S_{C2} / S_{C1} can be determined by:

$$\frac{N_{11} + N_{21}}{M_{11} + M_{21}} = 0.63 \quad (C.6)$$

In this equation (C.6), the only unknown variable is the reflection coefficient r of the spacer and thus r can be solved: $r = -0.35$.

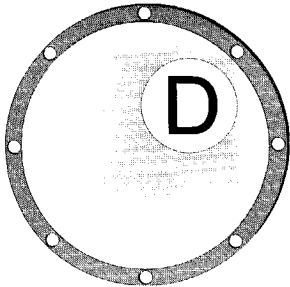
To validate this value, we modelled the spacer as a disk. Then we can calculate the characteristic impedance of the GIS and the spacer by (4.2). This results in the following relation between the impedance of the GIS and the spacer:

$$Z_{spacer} = \frac{1}{\sqrt{\epsilon_r}} Z_{GIS} \quad (C.7)$$

Then the reflection coefficient of the spacer ($\epsilon_r=5.3$) is estimated as

$$r = \frac{Z_{spacer} - Z_{GIS}}{Z_{spacer} + Z_{GIS}} = \frac{\frac{1}{\sqrt{\epsilon_r}} - 1}{\frac{1}{\sqrt{\epsilon_r}} + 1} = -0.39 \quad (C.8)$$

We can conclude that the reflection coefficient calculated from the measurements and from a model deviate only 10%. Therefore, we applied this empirical procedure to calculate the reflection coefficients of each of the GIS components.



APPENDIX D

PROCEDURE FOR ON-SITE UHF PD MEASUREMENTS

In this appendix we describe a procedure for on-site PD measurements using the UHF measuring technique according to the flow chart shown in figure D.1. This figure shows the necessary steps for a proper UHF PD measurement on-site.

Step 1: Connect the sensor and set the spectrum analyser.

The first step is proper setting of the spectrum analyser. Initially the same settings as during the last measurement will be applied. In this way the new measured frequency spectrum and the frequency spectrum measured last time can be easily compared.

Step 2: Measure the frequency spectrum

After setting the spectrum analyser, we can start the measurement. In this case, 20 sweeps are obtained and stored, and can be post-processed by averaging or hold max when necessary.

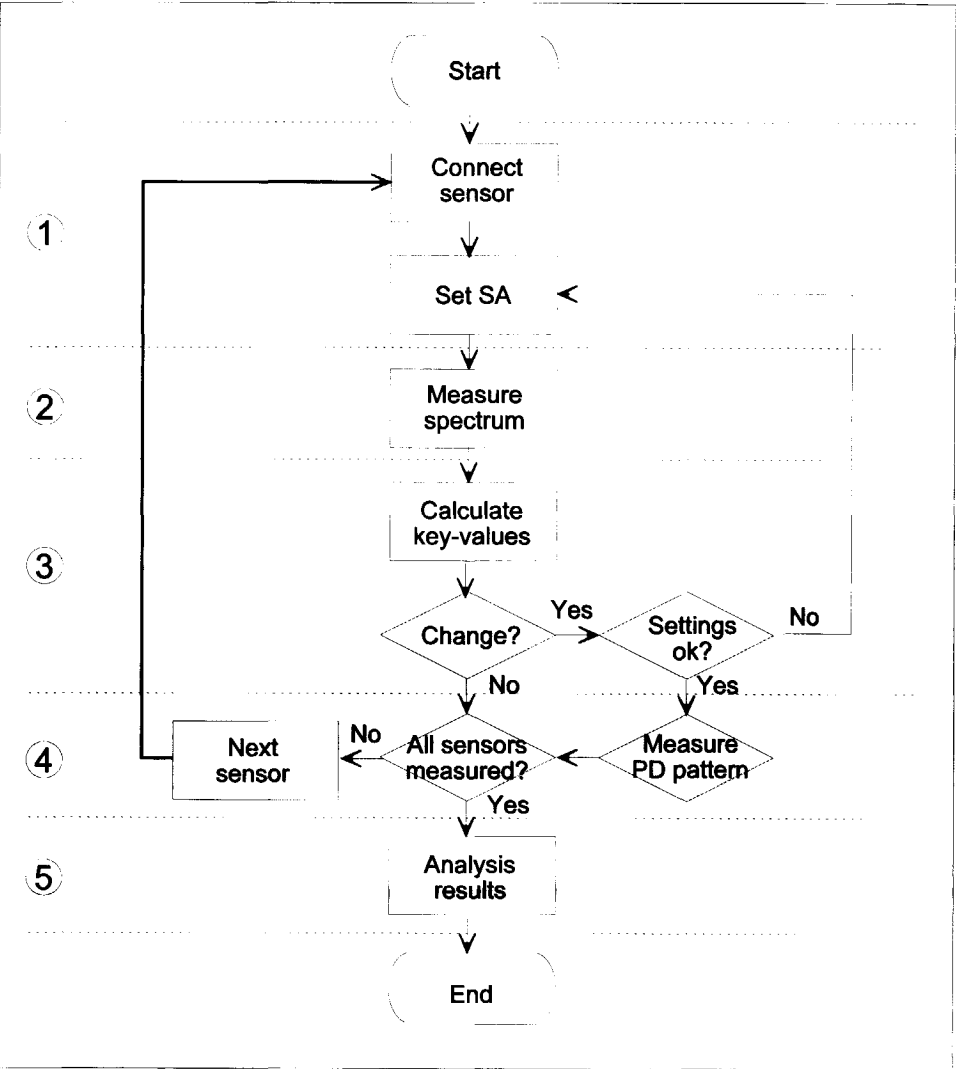


Figure D.1: Flow chart to be followed for on-site PD measurements using the UHF measuring technique for maintenance purposes.

Step 3: Calculation of the key values

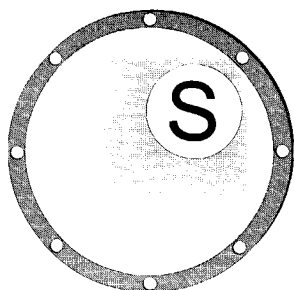
The measured results are analysed by processing the key values as defined in chapter 3. Moreover, if we analyse the trend in the key values over time, changes in the frequency spectra can quickly be seen. Any change can indicate a change in the PD process. In case of a change, we also measure the phase-resolved PD pattern for further analysis.

Step 4: Proceed until last sensor

These steps are repeated until we have measured the frequency spectra of all UHF couplers.

Step 5: Analysis of the obtained results

After the series of measurements, it is possible that the trend in the key values is changed at some of the UHF couplers. In this case also a phase-resolved PD pattern was measured. We compare both the frequency spectrum and the phase-resolved PD pattern with the reference database to find similar patterns in the reference database, indicating the likelihood of the presence of a defect. Based on this dielectric condition assessment, further maintenance steps have to be defined.

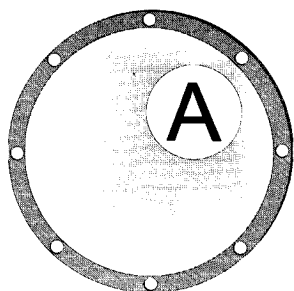


LIST OF SYMBOLS

Δa	Amplitude window size
c	Velocity of light
d	Transmission coefficient
f_c	Cut off frequency higher-order mode
f_c	Centre frequency of a spectrum analyser
Δf	Frequency window size
g	Acceleration of gravity
k_{mn}	Eigenvalues TM-modes
k_{mn}	Eigenvalues TE-modes
m	Mode number
m_{particle}	Mass of free moving particle
n	Mode number
p	Gas pressure
q_{particle}	Apparent charge of particle
q_{max}	The maximum discharge magnitude
q_n	The average discharge magnitude
r	Reflection coefficient
r_i	Radius inner conductor
r_o	Radius outer conductor
t	Transmission coefficient
v	Propagation velocity
z	Propagation direction of electromagnetic waves

A_i	The i^{th} amplitude window for amplitude window analysis
AP	Average power of the frequency spectrum
AR	Area under the measured frequency spectrum
E	Electric field intensity
F_i	The i^{th} frequency window for frequency window analysis
H	Magnetic field intensity
$H_{q_{\text{max}}}(\varphi)$	The maximum pulse height distribution
$H_{q_n}(\varphi)$	The mean pulse height distribution
$H_n(\varphi)$	The pulse count distribution
$H(q)$	The distribution function of the discharge magnitude
$H(p)$	The distribution function of the discharge energy magnitude
I	Current
J	Current density
J_m	Bessel function of order m
K	Surface current density
K_{A_i}	Kurtosis of distribution in amplitude slot analysis, for $i=_$: full spectrum, for $i=1$: low-frequency span and for $i=2$: high-frequency span
K_{F_i}	Kurtosis of distribution in frequency slot analysis, for $i=_$: full spectrum, for $i=1$: low-frequency span and for $i=2$: high-frequency span
MA	Maximum amplitude of the frequency spectrum
MP	Measured power in the frequency spectrum
N	Number of slots in amplitude distribution
N_m	Neumann function of order m
K	Peak in the frequency spectrum
S_{A_i}	Skewness of distribution in amplitude slot analysis, for $i=_$: full spectrum, for $i=1$: low-frequency span and for $i=2$: high-frequency span
S_{F_i}	Skewness of distribution in frequency slot analysis, for $i=_$: full spectrum, for $i=1$: low-frequency span and for $i=2$: high-frequency span
U_{inc}	Inception voltage of partial discharge activity
V	Voltage
V_b	Breakdown voltage
V_i	Inception voltage of partial discharge activity
X	Distance between two points
Z_0	Characteristic impedance for TEM waves
Z_{TEM}	Characteristic impedance for TEM waves

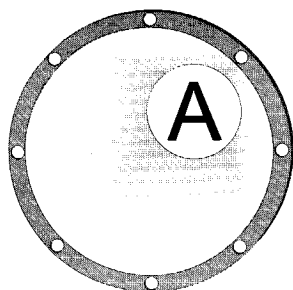
Z_{TE}	Characteristic impedance for TE waves
Z_{TM}	Characteristic impedance for TM waves
$V_{\text{artificial}}$	Voltage level of artificial pulses to simulate partial discharges of 5 pC magnitude
α	Ionization coefficient
γ	Probability to release an electron from the cathode when an ion collides with the cathode
γ	Propagation constant
ϵ_0	Permittivity of air
ϵ_r	Relative permittivity
η	SF ₆ attachment coefficient
μ_0	Permeability of air
μ_r	Relative permeability
ρ	Charge density
ϕ	Phase-angle (0-360°)
ω	Radial frequency



LIST OF ABBREVIATIONS

AC	Alternating Current
AP	Average measured Power
AR	Averaged aRea per data point
CIGRÉ	Conseil International des Grands Réseaux Électriques International Council on Large Electric Systems
dB	DeciBel
EM	ElectroMagnetic
GIL	Gas-Insulated Line
GIS	Gas-Insulated Substation
HP	Hewlett Packard
HV	High Voltage
IEC	International Electrotechnical Commission
LV	Low Voltage
MA	Maximum Amplitude
MP	Measured Power
N ₂	Nitrogen
pC	PicoCoulomb

PD	Partial Discharge
POW	Point-On-Wave
RBW	Resolution Bandwidth
SA	Spectrum Analyser
SF ₆	Sulphur Hexafluoride
TE	Transverse Electric
TEM	Transverse ElectroMagnetic
TF	Task Force
TM	Transverse Magnetic
UHF	Ultra High Frequency
VHF	Very High Frequency
WG	Working Group
BIL	Basic Insulation Level



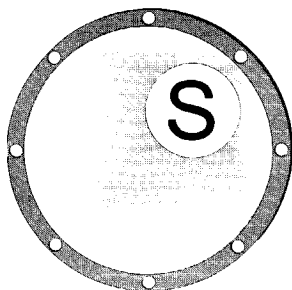
ACKNOWLEDGMENTS

For their support during my Ph.D. work, I want to thank:

- My promotor prof. dr. J.J. Smit and my supervisor dr. E. Gulski.
- Tennet BV, the Dutch grid company, for their financial support and for giving us access to the 380 kV substation in Meeden to perform measurements. Also their support in starting up this Ph.D. work has been of critical importance. In particular I want to thank J. Kanters for the many fruitful discussions.
- Alstom T&D in France who provided us with a large 380 kV GIS test setup of similar equipment as used in Meeden, which have been used for all laboratory investigations described in this thesis. Especially I want to thank A. Girodet for the interesting technical and scientific discussions.
- The students, who worked together with me in this project: F.J. Wester, A. Bovis and R.G.A. Zoetmulder.
- The people from the high-voltage laboratory for their technical support: W.A. Sonneveld, P.V.M van Nes, A. van der Graaf, W. Dronkers and B. Naagen
- My other colleague's dr. P.H.F. Morshuis, J.P. Zondervan, J. Beyer, J.P. van Bolhuis, H.J. van Breen and dr. H.F.M. van de Bosch.

Special thanks to my wife Rosita for her encouragement and support during the last years. I am also indebted to my children who were always able to lift my spirit. I also want to express my gratitude to God, Who gave me the strength and knowledge to carry out this work.

Sander Meijer



SAMENVATTING

Diagnose van Gas-geïsoleerde Hoogspanningsschakelsystemen op Basis van Deelontladingen

Gedurende de afgelopen dertig jaar hebben gasomsloten onderstations een hoge betrouwbaarheid getoond. Daarom worden dit type onderstations geplaatst op belangrijke knooppunten in het electriciteitsnet geplaatst. Toch hebben zich in het verleden problemen voorgedaan met als resultaat hoge kosten. Daarom zijn middelen om uitval te voorkomen gewenst.

Losse deeltjes, deeltjes op de steunisolatoren en scherpe uitsteeksels op de geleiders kunnen erg gevaarlijk zijn voor de isolatietoestand van het systeem. Dus voor toestandsafhankelijk onderhoud van gasomsloten onderstations is het detecteren en herkennen van dit soort defecten voor een doorslag belangrijk. Het meten van deelontladingen heeft zichzelf bewezen als een zeer gevoelige techniek om een mogelijke fout te voorspellen.

In dit proefschrift is de toepasbaarheid van een ontladingsmeettechniek gebaseerd op ultra-hoge frequenties onderzocht op de toegevoegde waarde voor toestandsafhankelijk onderhoud van gasomsloten onderstations.

Hoofdstuk 2 geeft een korte inleiding over gasomsloten systemen, over de isolatiegassen SF₆ en SF₆-N₂-mengsels, over typische isolatie defecten die in gasomsloten systemen kunnen optreden en elektromagnetische golfpropagatie van hoogfrequente signalen.

In hoofdstuk 3 worden the gebruikte ontladingsmeettechnieken en analysetechnieken beschreven. Om de inhoud van ontladingsspectra met elkaar te kunnen vergelijken zijn key-values gedefinieerd. Amplitude verdelingen gebaseerd op frequentie spectra zijn verder geanalyseerd met behulp van statistische methoden.

In hoofdstuk 4 zijn propagatie-effecten van de hoogfrequente ontladingssignalen in gasomsloten onderstations beschreven. Met deze kennis over signaalpropagatie kan de locatie van UHF opnemers worden bepaald om een bepaalde gevoeligheid van het UHF meetcircuit te garanderen.

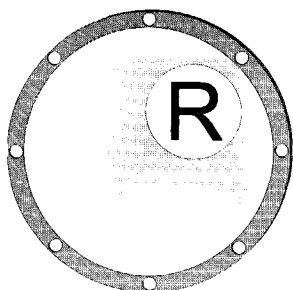
In hoofdstuk 5 worden meetresultaten beschreven van verschillende typen isolatie defecten in puur SF₆ en SF₆-N₂ gas mengsels met 5% en 10% SF₆. Hierdoor kon de invloed van deze defecten op de isolatie conditie van het gas worden bepaald en zijn typische resultaten opgeslagen in een databank.

Hoofdstuk 6 beschrijft een procedure voor het toepassen van de UHF meettechniek in het veld. Deze procedure is toegevoegd aan het onderhoudsconcept van het 380 kV gasomsloten onderstation in Meeden in Nederland.

Risico analyse van defecten op de isolatieconditie van GIS is beschreven in hoofdstuk 7. Om het gevaar van uitsteeksels en losse deeltjes te bepalen zijn zowel de fase-verdeelde ontladingspatronen als de ontladingsspectra nodig.

De uitkomst van dit onderzoek is dat de UHF ontladingsmeettechniek een gevoelige meettechniek is om de isolatietoestand van gasomsloten onderstations te bepalen.

Sander Meijer



RÉSUMÉ

Interprétation de Décharges Partielle du Matériel Haute Tension Blindé

La fiabilité des postes sous enveloppe métallique n'a cessé de s'améliorer au cours de ces 30 dernières années et de nombreux postes ont été installés sur les différents réseaux électriques. Pour éviter les défauts, dont les conséquences financières sont importantes, il est nécessaire de mettre en place des moyens pour les prévenir.

Les particules libres ou fixées sur les isolants ainsi que les pointes sur les conducteurs peuvent réduire la tenue diélectrique des PSEM. La détection et l'identification de ces défauts dès leur apparition sont importants lorsqu'une maintenance préventive du PSME est envisagée. La mesure des décharges partielles est l'une des méthodes les plus sensibles pour prévenir les amorçages causés par ce genre de défauts d'isolation.

Cette thèse présente l'utilisation de la méthode de mesure des décharges partielles par UHF dans le but d'une maintenance préventive des PSEM.

Le chapitre 2 est une introduction sur les systèmes à isolation gazeuse SF_6 ou mélange N_2/SF_6 et les types de défauts qu'ils génèrent. Le mode de propagation des ondes électromagnétiques est également abordé.

Le chapitre 3 aborde les différentes techniques de mesure et d'analyse des décharges partielles. La comparaison des spectres de fréquence est effectuée à partir du calcul de valeurs clés et par application des méthodes statistiques sur les courbes de distribution des amplitudes.

Le chapitre 4 décrit le mode de propagation des ondes UHF à l'intérieur du PSEM. Leur connaissance permet d'optimiser la position des capteurs pour assurer une sensibilité suffisante au système de mesure par la méthode UHF.

Le chapitre 5 étudie le comportement des défauts d'isolation dans le SF₆ pur et le mélange N₂/SF₆ contenant 5% et 10% de SF₆. Des résultats caractéristiques ont été établis et mis dans une base de données.

Le chapitre 6 décrit la procédure utilisée pour la mesure des décharges partielles par UHF lors de la maintenance du poste blindé 380kV de Meeden en Hollande.

L'étude du risque associé aux défauts d'isolation dans les PSEM est développée dans le chapitre 7. Il est démontré que par l'analyse des spectres et des images temporelles il est possible d'obtenir les informations suffisantes pour évaluer la criticité des défauts de type pointe et des particules libres.

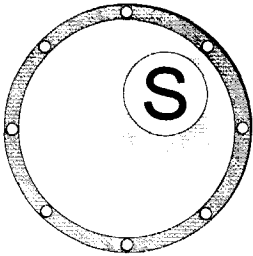
En conclusion il est démontré que la méthode de mesure des décharges partielles par UHF est une technique suffisamment sensible pour surveiller la tenue diélectrique des systèmes à isolation gazeuse.

Sander Meijer



Visual inspection and quality control of GIS during assembling

Sander Meijer studied electrical engineering at the "Hoge School Rotterdam" in Rotterdam from 1988 to 1992. He finished his study at Delft University of Technology in 1995. In the same year he started with his Ph.D. research project at the department of high voltage technology.



STELLINGEN / PROPOSITIONS

behorende bij het proefschrift

**Partial Discharge
Diagnosis
of
High-Voltage Gas-
Insulated Systems**

Sander Meijer
5 november 2001

1. Continue on-line monitoring van metaal-omsloten gas-geïsoleerde schakelinstallaties (GIS) kan alleen een serieuze toekomst hebben als de betrouwbaarheid van het toekomstige diagnostische systeem beter zal zijn dan die van de GIS-installatie zelve.

The perspective of continuous on-line monitoring of metal-enclosed gas-insulated switchgear (GIS) can only be successful if the reliability of this future diagnostic system surpasses the reliability of the GIS-system itself.

2. Het enthousiasme over de toepasbaarheid van ontladingsdiagnostiek op toestandsafhankelijk onderhoud van grote elektrische installaties, dat diverse onderzoekers aan de dag leggen, is meestal het gevolg van een onjuiste inschatting van de invloed van de bedrijfsomstandigheden.

The enthusiasm about the applicability of partial discharge diagnostic for condition-based maintenance of large electrical equipment, which is elucidated by several investigators, often results from erroneous estimations on the influence of the operating conditions.

3. De elektromagnetische straling van deelontladingen kan in principe worden toegepast voor diagnostische metingen aan alle hoogspannings-componenten.

The electromagnetic radiation produced by partial discharges can in principle be used for diagnostic measurements on all high-voltage components.

4. In geval van zwavelhexafluoride-stikstof mengsels zijn de hoge eisen, die worden gesteld aan de detectiegevoeligheid voor ontladingen in puur zwavelhexafluoride, niet meer nodig.

The high requirements imposed on the detection-sensitivity for partial-discharges in pure sulphur hexafluoride are not necessary into its full extent in case of sulphur hexafluoride-nitrogen mixtures.

5. Het efficiënt toepassen van hoge temperatuur supergeleidende materialen in de elektrische energietechniek is primair een systeemkwestie.

Effective application of high-temperature superconducting materials in the electrical power technology is primarily a system issue.

6. De behandeling van vloeistoffen door middel van gepulste elektrische velden voor het onschadelijk maken van bacteriën en sporen wordt begrensd door de temperatuur van de vloeistof aan de wand.

Treatment of liquids, using pulsed electric fields to inactivate bacteria's and spores, is limited by the temperature of the liquid at the wall of treatment chamber.

7. Als de privatisering van elektrische distributienetten een zelfde effect heeft als de privatisering van de Nederlandse Spoorwegen, dan zijn, naast algemene ontevredenheid, uitval van energieleveringen te verwachten.

If the privatisation of the electrical distribution results in similar effects as with the privatisation of the Dutch Railway, then besides general dissatisfaction, loss of power delivery has to be expected.

8. Bij het beheersen van een technisch risico spelen economische aspecten een dominante rol.

Control of technical risks is influenced in a dominant way by economical aspects.

9. Duurzame energie in een geliberaliseerde marktomgeving moet zich nog bewijzen.

Renewable energy has still to prove itself in a liberalised market environment.

10. De externe opinie maakt een topuniversiteit.

The external judgment makes a top university.

